NORTHWESTERN UNIVERSITY

Phenomenology of Light Sterile Neutrinos and Neutrino Dipole Moments

A DISSERTATION

SUBMITTED TO THE GRADUATE SCHOOL

IN PARTIAL FULFILLMENT OF THE REQUIREMENTS

for the degree

DOCTOR OF PHILOSOPHY

Field of Physics

By

Giancarlo Jusino Sánchez

EVANSTON, ILLINOIS

June 2023

ABSTRACT

Phenomenology of Light Sterile Neutrinos and Neutrino Dipole Moments

Giancarlo Jusino Sánchez

This thesis focuses on exploring the explanatory and discovery potential of the four-neutrino and enhanced neutrino magnetic and electric dipole moments hypotheses when applied to the NOvA/T2K discrepancy and the XENON1T anomaly, respectively. Firstly, we study the effect of a very light (sub eV) sterile neutrino on the NOvA/T2K anomaly. We find that for some regions of the parameter space the four-neutrino hypothesis is preferred with moderate significance. Secondly, we study the parameter space of the neutrino dipole moment matrix given Majorana or Dirac neutrinos. We discuss the XENON1T anomaly given the recent XENOXnT measurement. We also study how the potential physics reach of future experiments depends on the nature of neutrinos. We find that a next-generation experiment two orders of magnitude more sensitive to the neutrino dipole moments via muon-neutrino elastic scattering could discover that neutrino electromagnetic moments are nonzero if neutrinos are Dirac fermions. Instead, if neutrinos are Majorana fermions, such a discovery is excluded by existing solar neutrino data, unless there are more than three light neutrinos.

Acknowledgements

This thesis would not have been possible without the support of my family, friends, and community at Northwestern. Primarily, I want to thank my mother Iris for encouraging and supporting me throughout this entire journey. I could not have accomplished this without you being there in the best and worst of times. I also want to thank Tio Juancho and Abuelita Yoly for their love now and always.

I want to thank my advisor André de Gouvêa for his immense patience, promptness, and wisdom; my committee members John Joseph Carrasco, Ian Low, and Timothy Kovachy for amazing classes and service in my committee. A special thanks to Kevin Kelly and Zahra Tabrizi for all of the work and mentoring during our collaborations. I also want to thank Mayda Velasco and Michael Schmitt for seeing potential in me so long ago during the SROP and making this experience possible.

I want to thank the Department of Physics & Astronomy and TGS for supporting me. I also want to thank CAPS and the Research Computing Services at Northwestern IT, especially Colby Witherop and Julie Anh Nguyen, for their amazing support and guidance. Finally, I would like to thank Gayle Ratliff and my classmates past and present Joseph and Suna for their help and making this experience as enjoyable as it was.

Dedication

In memory of my grandparents: Juan Ramón Sánchez who stoked my interest in science; and Linberg and Miriam for their unconditional love

Table of Contents

List of Tables

List of Figures

CHAPTER 1

Introduction

Our observations of the behavior of neutrinos have shown us that the Standard Model of Particle Physics (SM) is not complete. While the SM assumes neutrinos are massless, all evidence points to neutrinos having mass. This evidence is that we have observed neutrinos to change flavor from that at the point of production to where they are detected. We call this phenomenon flavor oscillation and it is best described by mixing the neutrino flavor states with mass states via a unitary matrix. We can describe this oscillation by time-evolving the Hamiltonian of the system. Neutrino masses and flavor oscillations open the field to many questions, including Beyond the Standard Model (BSM) queries, such as:

- How do neutrinos get their mass?
- Are neutrinos their own antiparticle?
- Are there sterile neutrinos?
- What is the mass ordering of the neutrino mass eigenstates?

But we can ask an even more immediate question: What are the entries of the aforementioned mixing matrix? In the last decades a monumental amount of effort has been expended towards the goal of measuring these entries and trying to answer some of these questions. We have gone from positing and observing the phenomena [**5, 6, 7, 8, 9,**

10, 11, 12, 13], to making groundbreaking measurements and an era of precision measurements [**14, 15, 16, 17, 18**], and continuing our efforts with the next generation of experiments [**19, 20, 21**]. Nevertheless, along the way we have made measurements that have left us with lingering and uncomfortable discrepancies and anomalies. This thesis aims to, at this particular point in time, explore some of these anomalies by considering some of the aforementioned questions as hypotheses. Furthermore, we will comment on the role that these future high precision experiments can play with regards to these anomalies and questions.

1.1. Flavor Oscillations & Interactions

1.1.1. Vacuum

Neutrinos are created via the weak interactions as distinct flavor eigenstates $|\nu_\alpha\rangle$ with α denoting the flavor corresponding to the charged leptons: electrons e, muons μ, and tauons τ. Neutrinos then propagate as mass eigenstates $|\nu_i\rangle$ with $i = 1, 2, 3...$ corresponding to the number of neutrino states. Neutrinos are detected via weak interactions though W boson (Charged Current) or Z boson (Neutral Current) exchange. We can measure the probability of neutrinos being detected as the initial flavor eigenstate $P_{\alpha\alpha}$ or of it changing to a different final state $P_{\alpha\beta}$. We also expect to conserve probability, so $\sum_\beta P_{\alpha\beta} = 1$. We will briefly discuss the standard derivation of neutrino oscillations probabilities in vacuum to have a working base for Chapter 2 and Chapter 3.

Neutrino flavor eigenstates can be written as a weighted sum of the mass eigenstates.

$$|\nu_\alpha\rangle = \sum_i U^*_{\alpha i} |\nu_i\rangle \,, \tag{1.1.1}$$

where U is a complex unitary matrix, to conserve probability, that maps the flavor eigenstates to the mass eigenstates. In the three neutrino picture, the matrix can be parametrized by three mixing angles θ_{12}, θ_{13}, and θ_{23} usually referred to as the solar, reactor, and atmospheric mixing angles, respectively. These monikers come from the phenomena that dominated the oscillation when first trying to measure these parameters. In the case of Dirac neutrinos, there is also one physical complex Charge Parity (CP) violating phase $\delta_{13} = \delta_{\rm CP}$ called the Dirac phase.

$$U_{3\times3} = \begin{pmatrix} 1 & 0 & 0 \\ 0 & \cos\theta_{23} & \sin\theta_{23} \\ 0 & -\sin\theta_{23} & \cos\theta_{23} \end{pmatrix} \begin{pmatrix} \cos\theta_{13} & 0 & \sin\theta_{13}e^{-i\delta_{\rm CP}} \\ 0 & 1 & 0 \\ -\sin\theta_{13}e^{i\delta_{\rm CP}} & 0 & \cos\theta_{13} \end{pmatrix} \begin{pmatrix} \cos\theta_{12} & \sin\theta_{12} & 0 \\ -\sin\theta_{12} & \cos\theta_{12} & 0 \\ 0 & 0 & 1 \end{pmatrix}. \tag{1.1.2}$$

In the three-neutrino picture, U in Eq. (1.1.2) is usually called the Pontecorvoo-Maki-Nakagawa-Sakata (PMNS) matrix. For Majorana neutrinos U becomes UU^M where U^M is a diagonal unitary matrix with two physical phases.* We are interested in the probability $P_{\alpha\beta}$ for an initial neutrino flavor eigenstate ν_α to a final flavor eigenstate ν_β. To calculate this we time-evolve $|\nu_\alpha\rangle$ so we can project $\langle\nu_\beta|$ unto it to get the transition amplitude. The time evolution is best described in the mass basis because the mass states $|\nu_k\rangle$ are the eigenstates of the free-particle (propagation) Hamiltonian H,

$$H\,|\nu_k\rangle = E_k\,|\nu_k\rangle\,. \tag{1.1.3}$$

*We omit these additional Majorana phases because they do not contribute to the oscillation probability Eq. (1.1.8). Furthermore, in Chapter 3, they can be absorbed into the off-diagonal magnetic moment matrix phases for Majorana neutrinos.

Where the E_k are the energy eigenvalues. With these we can write the plane wave solutions to the time-dependent Schrödinger equation $H\left|\nu_k(t)\right\rangle = i\frac{d}{dt}\left|\nu_k(t)\right\rangle$,

$$\left|\nu_k(t)\right\rangle = e^{-iE_k t}\left|\nu_k(0)\right\rangle, \quad \text{where} \quad \left|\nu_k(t=0)\right\rangle = \left|\nu_k\right\rangle. \tag{1.1.4}$$

Using this solution, Eq. (1.1.1), and its inversion, we can write out the time-evolution of the initial state $\left|\nu_\alpha(0)\right\rangle$ in the flavor basis,

$$\left|\nu_\alpha(t)\right\rangle = \sum_\beta \sum_k U^*_{\alpha k} U_{\beta k} e^{-iE_k t}\left|\nu_\beta\right\rangle. \tag{1.1.5}$$

Given that neutrinos have small masses and they travel close to the speed of light, it is beneficial to take the ultrarelativistic approximation. The energy eigenvalues become

$$E_K = \sqrt{\vec{p}^2 + m_k^2} \simeq E_\nu + \frac{m_k^2}{2E_\nu}, \tag{1.1.6}$$

where we neglect the neutrino mass from the neutrino energy $E_\nu = |\vec{p}|$. The transition amplitude is given by,

$$A_{\alpha\beta}(t) = \left\langle \nu_\beta | \nu_\alpha(t) \right\rangle. \tag{1.1.7}$$

Usually, the distance L between the source and detector is known rather the oscillation time t so we approximate $t = L$. We can evaluate the transition probability of a neutrino with initial flavor state α to be detected some time later as a flavor state β to be,

$$P_{\alpha\beta}(L, E_\nu) = \left|\left\langle \nu_\beta | \nu_\alpha(L) \right\rangle\right|^2 = \sum_k \sum_j U^*_{\alpha k} U_{\beta k} U_{\alpha j} U^*_{\beta j} e^{-i(E_k - E_j)L}. \tag{1.1.8}$$

We can see that the oscillation depends on the difference of the eigenvalues. From Eq. (1.1.6) this difference is approximately $E_k - E_j \simeq \frac{\Delta m^2_{kj}}{2E_\nu}$ with $\Delta m^2_{kj} = m^2_k - m^2_j$. From this relation it is clear that neutrino flavor oscillation probabilities are only sensitive to neutrino mass squared differences. In the three-neutrino picture this implies two mass squared differences for three massive states. These splitting can be arranged in two ways,

$$\begin{aligned} &m_1 < m_2 < m_3 \quad \text{Normal Ordering (NO)} \\ &m_3 < m_1 < m_2 \quad \text{Inverted Ordering (IO)}, \end{aligned} \tag{1.1.9}$$

giving rise to the mass ordering question, hinted at before.

We can also write these transition probabilities in matrix form,

$$\Psi_\alpha = (A_{\alpha e}, A_{\alpha\mu}, A_{\alpha\tau}), \quad i\frac{\mathrm{d}}{\mathrm{dt}}\Psi_\alpha = H_F\Psi_\alpha, \tag{1.1.10}$$

where H_F is the Hamiltonian in the flavor basis. In the mass basis, the Hamiltonian becomes diagonal with entries proportional to each mass-squared value. Addition or subtraction of terms proportional to the identity matrix leave the transition probability unchanged, allowing us to write:

$$H_F = U\mathbf{M}U^\dagger = U \begin{pmatrix} 0 & 0 & 0 \\ 0 & \frac{\Delta m^2_{21}}{2E_\nu} & 0 \\ 0 & 0 & \frac{\Delta m^2_{31}}{2E_\nu} \end{pmatrix} U^\dagger. \tag{1.1.11}$$

It is instructive to consider the two-neutrino vacuum oscillation case that can be characterized by a 2×2 unitary matrix U parametrized by θ and a single mass-squared splitting

Δm^2.

$$U_{2\times 2} = \begin{pmatrix} \cos\theta & -\sin\theta \\ \sin\theta & \cos\theta \end{pmatrix}. \tag{1.1.12}$$

Eq. (1.1.8) would take the form,

$$P_{\nu_\alpha \to \nu_\beta}(L, E_\nu) = \sin^2 2\theta \sin^2\left(\frac{\Delta m^2 L}{4E_\nu}\right) \tag{1.1.13}$$

where E_ν is the neutrino energy and L is the distance of propagation. We see that the amplitude of the oscillation depends on the mixing parameters while the frequency is driven by the mass-squared splitting and neutrino energy. In our analysis, we will work with neutrinos with energies in the GeV range and baselines of the order of hundreds of km, so it is useful to rewrite the oscillation argument in Eq. (1.1.13) as

$$1.27\frac{\Delta m^2[\mathrm{eV}^2]L[\mathrm{km}]}{E_\nu[\mathrm{GeV}]}. \tag{1.1.14}$$

The oscillations of interest in Chapter 2 feature the three-neutrino and four-neutrino pictures. The analytical functions of the transition and survival probabilities are cumbersome, so instead we elect to show plots of the oscillations where pertinent.

1.1.2. Matter

The interactions via the weak force of neutrinos with the matter they propagate through are critical in our description of solar and accelerator neutrinos. The intervening matter is composed of electrons e^-, protons p, and neutrons n. As neutrinos propagate in matter they predominantly interact with electrons via the Charged Current (CC) through W

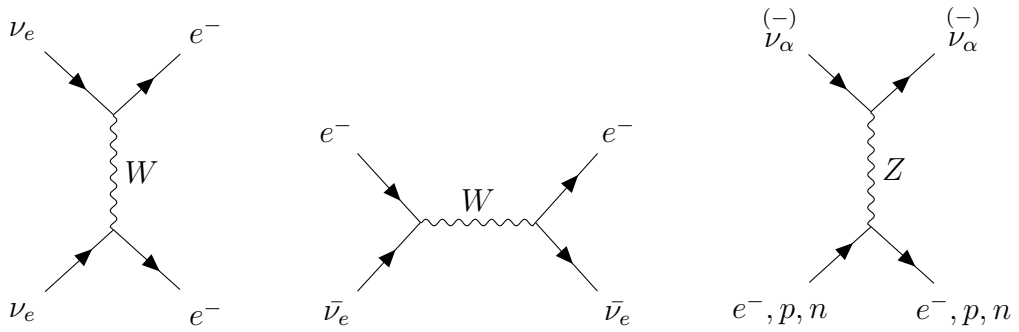

Figure 1.1. Feynman diagrams that contribute to coherent forward elastic scattering as neutrinos or anti-neutrinos propagate through matter. The two leftmost diagrams contribute to the Charged Current potential $V_{\rm CC}$ for scattering with electrons in the media. The rightmost diagram contributes to the Neutral Current potential $V_{\rm NC}$ as the (anti)-neutrinos scatter with all of the components of the media.

exchange. The neutrinos also interact with the intervening e^-, p, n via the Neutral Current (NC) through Z exchange. The diagrams contributing to these interactions are shown in Fig. 1.1. Of concern to us are interactions where neutrinos reach the detector and leave the intervening matter unchanged – this is coherent forward elastic scattering. In the CC case, we can take neutrinos to be traveling in a homogeneous static gas of electrons characterized by electron density N_e. We can modify H_F in the flavor-basis from Eq. (1.1.11) to include these contributions as effective potential terms,

$$H_F = U\mathbf{M}U^\dagger + H^{\rm CC} + H^{\rm NC}. \tag{1.1.15}$$

The CC effective potential contribution is given by,

$$H^{\rm CC}_{\alpha\beta} = V_{\rm CC}\delta_{\alpha e} = \sqrt{2}G_{\rm F}N_e\delta_{\alpha e}, \tag{1.1.16}$$

where $G_{\rm F}$ is the Fermi constant. The NC interactions include contributions from electrons, protons, and neutrons. For ordinary matter we assume electrical neutrality, meaning an equal number of electrons and protons. The electron and proton NC effective potential contributions are equal in magnitude but differ by a sign, so the only net contribution to $H^{\rm NC}$ is that of neutrons.

$$H^{\rm NC}_{\alpha\beta} = V_{\rm NC}\delta_{\alpha\beta} = \sqrt{2}/2 G_{\rm F} N_n \delta_{\alpha\beta}, \tag{1.1.17}$$

where N_n is the density of neutrons in matter. For anti-neutrinos, the matter potentials $V_{\rm CC}$ and $V_{\rm NC}$ gain a negative sign. A useful fact is that the NC contribution to the Hamiltonian is proportional to the identity matrix; since we can add or subtract terms proportional to the identity matrix at the level of the Hamiltonian we can ignore the NC contribution in the three-neutrino picture. Nevertheless, this will not be the case in Chapter 2 where we consider sterile neutrinos that, by definition, do not interact via Z exchange. The simplest case, which for our purposes applies to the intervening matter in accelerator experiments, has the effective matter potentials depend only on constant N_e or N_n. With this in mind we can diagonalize $H_{\rm F}$ and re-parameterize in terms of an effective matter mixing matrix $U_{\rm M}$ as the eigenvector matrix and $H_{\rm M}$ as the diagonalized eigenvalue matrix, such that

$$U^{\rm T}_{\rm M} H_{\rm F} U_{\rm M} = H_{\rm M}. \tag{1.1.18}$$

We can then substitute these effective matter objects into Eq. (1.1.8) to calculate the probability of neutrino oscillations given a constant matter profile. In the two-neutrino framework, the survival probability of an electron-neutrino ν_e in matter of constant density

is given by

$$P_{\nu_e \to \nu_e}(L, E_\nu) = \sin^2 2\theta_{\rm M} \sin^2 \left(\frac{\Delta m^2_M L}{4E_\nu} \right), \tag{1.1.19}$$

where θ_M and Δm^2_M follow from U_M and $H_{\rm M}$. In Chapter 3 we also consider neutrinos that are created in the Sun and are detected at Earth. The propagation of these neutrinos follow three regions of interest: from their point of creation in the Sun until they reach space, from the edge of the Sun to Earth, and any intervening matter between the point of terrestrial ingress and where the detector is located. The solar region does not feature a constant matter profile, but at the low energies of interest we can apply the adiabatic approximation. As calculated in [**22**], for solar neutrinos with low energy we can approximate their behavior by taking

$$\theta_{12} \to \theta^{(i)}_M. \tag{1.1.20}$$

$\theta^{(i)}_M$ is the effective solar mixing angle of the solar neutrinos at their point of production in the Sun. The survival probability will be of use in Chapter 3 when we discuss the solar effective neutrino magnetic moment.

1.1.3. Electromagnetic Interactions

Massive neutrinos gain a coupling to the photon when we include loop level effects. We are concerned with the effective vertex in Fig. 1.2 between initial and final neutrino mass states ν_i and ν_f. As discussed in [**22**], the effective vertex $\Lambda_{if}(q)$ depends only on the

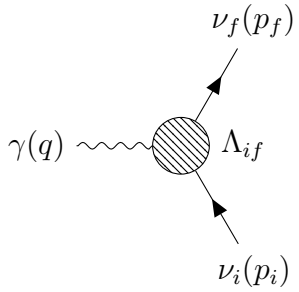

Figure 1.2. Effective coupling of neutrinos to the electromagnetic field given one photon. Transitions between different initial ν_i and final ν_f state neutrinos are mediated by the effective vertex Λ_{if}.

four-momentum transferred to the photon. It can be expressed as a linear combination of six Lorentz invariant form factors. In the real photon case where $q^2 = 0$, these form factors reduce to $\boldsymbol{q}_{if}, \boldsymbol{\mu}_{if}, \boldsymbol{\epsilon}_{if}$, and $\boldsymbol{a}_{if}$. These are the neutrino charge, magnetic dipole moment, electric dipole moment, and anapole moment, respectively. We focus our attention to the well studied magnetic and electric dipole moments. Within the framework of the minimally extended Standard Model, the one-loop contributions to the neutrino one photon coupling are shown in Fig. 1.3.

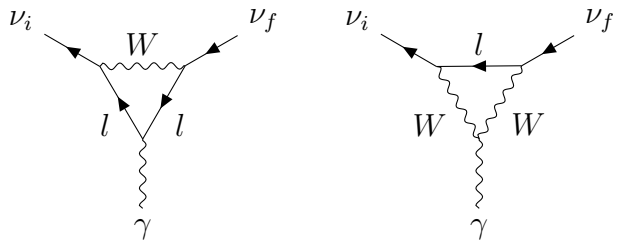

Figure 1.3. Feynman diagrams contributing to the one-loop coupling between neutrinos and one photon in the minimally extended Standard Model. There is an implied sum over all leptons $l = e, \mu, \tau$.

For Majorana neutrinos, only transition moments are allowed. As discussed in [**22**] the SM expectation has been calculated to be

$$\begin{aligned} \boldsymbol{\mu}_{kj}^{\mathrm{Maj}} &\simeq -\frac{3ieG_{\mathrm{F}}}{16\sqrt{2}\pi^2}(m_k + m_j)\sum_l \mathrm{Im}[U_{lk}^* U_{lj}]\frac{m_l^2}{m_W^2}, \\ i\boldsymbol{\epsilon}_{kj}^{\mathrm{Maj}} &\simeq -\frac{3eG_{\mathrm{F}}}{16\sqrt{2}\pi^2}(m_k - m_j)\sum_l \mathrm{Re}[U_{lk}^* U_{lj}]\frac{m_l^2}{m_W^2}, \end{aligned} \tag{1.1.21}$$

for $kj = 1, 2, 3$ and $l = e, \mu, \tau$. It follows that only the transition elements $f \neq i$ are non-vanishing. Furthermore, we can see that the moments are proportional to the neutrino masses and the ratio of the charged lepton masses with the W mass. These two factors lead to very small magnetic and electric dipole moments – outside the reach of any currently conceivable experimental endeavour.

The picture does not change if we instead consider a minimally extended SM with massive Dirac neutrinos. As discussed in [**22**] the SM expectation is

$$\begin{aligned} \boldsymbol{\mu}_{kj}^{\mathrm{Dir}} &\simeq \frac{3eG_{\mathrm{F}}}{16\sqrt{2}\pi^2}(m_k + m_j)\left(\delta_{kj} - \frac{1}{2}\sum_l U_{lk}^* U_{lj}\frac{m_l^2}{m_W^2}\right), \\ i\boldsymbol{\epsilon}_{kj}^{\mathrm{Dir}} &\simeq \frac{3eG_{\mathrm{F}}}{16\sqrt{2}\pi^2}(m_k - m_j)\left(\delta_{kj} - \frac{1}{2}\sum_l U_{lk}^* U_{lj}\frac{m_l^2}{m_W^2}\right). \end{aligned} \tag{1.1.22}$$

The Dirac case allows for diagonal magnetic and electric moments, but we see a similar issue with the transition moments depending on the neutrino masses and being further suppressed by the W mass. Of particular interest is the diagonal case, where the magnetic and electric moments are no longer suppressed by m_l^2/m_W^2,

$$\boldsymbol{\mu}_{kk} \simeq \frac{3eG_{\mathrm{F}}}{8\sqrt{2}\pi^2} m_k \simeq 3.2 \times 10^{-19}\ \mu_B, \tag{1.1.23}$$

where $\mu_B = 1/(2m_e)$ is the Bohr magneton. In the SM, this renders the diagonal elements of the Dirac neutrino magnetic and electric dipole moments to be much larger than the transition elements. Nevertheless, these are also too small and inaccessible to current or proposed future experiments. Therefore, any enterprise that aims to measure neutrino magnetic moments with current sensitivities will be looking for larger enhanced moments where the effective vertex in Fig 1.2 includes Beyond the Standard Model (BSM) contributions. These BSM enhanced magnetic moments will have to be much larger, within the reach of current experiments.

Of particular interest to us is elastic scattering between any incoming neutrino state and an electron. The electromagnetic contribution has the convenient feature that it can be added incoherently to the SM neutrino-electron scattering cross-section. This is due to the fact that weak interactions seek to preserve helicity while electromagnetic interactions seek to change it. This allows us to write

$$\frac{d\sigma_{\nu_l e^-}}{dT_e} = \left(\frac{d\sigma_{\nu_l e^-}}{dT_e}\right)_{\mathrm{SM}} + \left(\frac{d\sigma_{\nu_l e^-}}{dT_e}\right)_{\mathrm{mag}}, \tag{1.1.24}$$

where T_e is the kinetic energy of the recoil electron – what the detector is able to measure. The electromagnetic contribution is given by

$$\left(\frac{d\sigma_{\nu_l e^-}}{dT_e}\right)_{\text{mag}} = \frac{\mu_{\nu_l}^2}{\mu_{\text{B}}^2}\frac{\pi\alpha^2}{m_e^2}\left(\frac{1}{T_e}-\frac{1}{E_\nu}\right). \tag{1.1.25}$$

Where m_e is the mass of the electron, α is the fine structure constant, and μ_{ν_l} is the effective neutrino magnetic moment relevant to the experiment in consideration. This effective magnetic moment is characteristic of the flavor composition of the incoming neutrino flux.

If we consider an effective magnetic moment $\mu_{\nu_l}^2$, we are concerned with the neutrinos detected some space-time distance away from from the scattering interaction. This will be a sum of the final states of the form,

$$\mu_{\nu_l}^2 = \sum_j \left| \sum_k U_{lk}^* e^{-i\Delta m_{kj}^2 \frac{L}{2E_\nu}} (\boldsymbol{\mu}_{jk} - i\boldsymbol{\epsilon}_{jk}) \right|^2 . \tag{1.1.26}$$

We will explore the fundamental neutrino magnetic moments in the mass basis with greater detail in Chapter 3, but we can make some additional simplifications. For all the cases considered in this thesis, the oscillation term $\Delta m_{kj}^2 \frac{L}{2E_\nu}$ in Eq. (1.1.26) is too small, allowing us to neglect the oscillation term. Furthermore, $\boldsymbol{\mu}_{jk}$ and $\boldsymbol{\epsilon}_{jk}$ are general complex (anti-symmetric in the case of Majorana neutrinos) matrices. We cannot distinguish between the electric and magnetic moments in the general BSM scenario, so henceforth we refer to the magnetic moment μ_{jk} as

$$\mu_{jk} = \boldsymbol{\mu}_{jk} - i\boldsymbol{\epsilon}_{jk}. \tag{1.1.27}$$

With these tools we are now primed to tackle the anomalies.

1.2. Anomalies

Since the discovery of neutrino flavor oscillations we have come across several anomalies, some of the more interesting ones being [**23, 24, 25, 26, 27**]. We want to address two such anomalies: One is the discrepancy between the measurements of oscillation parameters by the NOvA and T2K experiments. The other is an excess of events, potentially from solar neutrinos, in the XENON1T experiment [**2**]. For the former we explore the possibility of a very light sterile neutrino assuaging the discrepancy. For the latter we explore BSM magnetic moments as a possible solution – with an eye towards the Majorana and Dirac nature of neutrinos.

1.2.1. NOvA & T2K Discrepancy

The NOvA and T2K experiments are both long-baseline accelerator experiments intended to measure muon-neutrino to electron-neutrino conversion. They have improved our measurements of θ_{23} and ideally have something to say about the CP violating phase δ_{CP}. The discrepancy has two manifestations: Firstly, as shown in Fig. 1.4, the preferred regions of the experiments are in mild tension (1.7σ [**28**]) under the NO. Secondly, individually, both experiments prefer the NO. Nevertheless, the combination of both experiments prefers the IO. If this discrepancy persists, it can become a window to BSM Physics such as neutrino NSIs and sterile neutrinos.

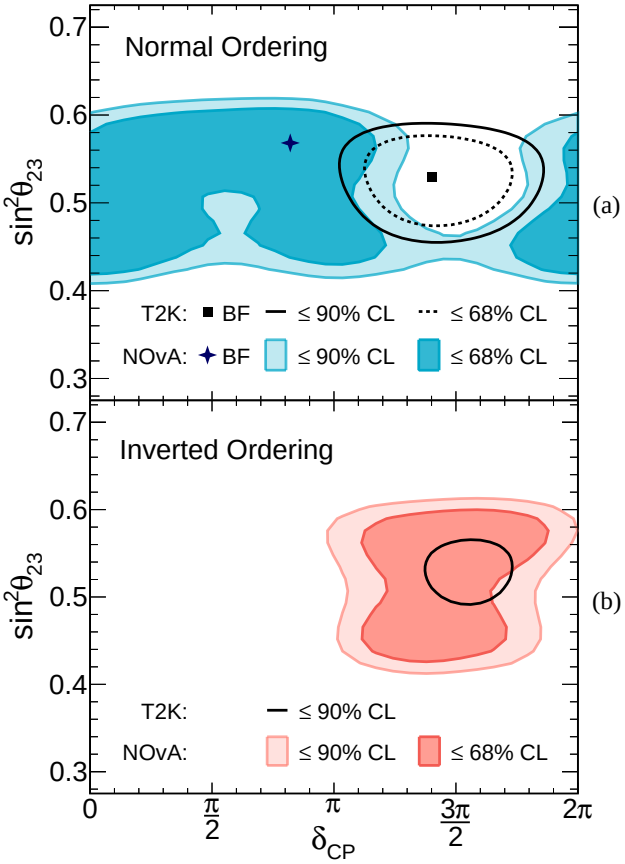

Figure 1.4. The 68% and 90% confidence level contours in $\sin\theta_{23}{}^2$ vs. δ_{CP} in the (a) normal mass ordering and (b) inverted mass ordering.The cross denotes the NOvA best fit point and colored areas depict the 90% and 68% allowed regions. Overlaid black solid-line and dashed-line contours depict allowed regions reported by T2K. [**1**]

The key difference between these experiments is the importance of matter effects. We are sensitive to BSM hypotheses that are affected by the matter interactions as the neutrinos propagate from the source to the detectors. In this thesis, we want to leverage these facts and this discrepancy to explore whether a very light sterile neutrino meaningfully softens this tension.

1.2.2. XENON1(n)T Excess (Measurement)

The XENON1T experiment was one of the premier dark matter search enterprises. In their search, came upon an excess of electron recoil events at low energies. This anomalous excess could be explained by an as-of-yet unmeasured amount of Tritium in the detector. Nevertheless, we can also suppose that this excess is due to new Physics. Two other exciting hypotheses that can explain the excess are Solar axions and new neutrino properties leading to a large neutrino magnetic moment. The data and interpretations of the XENON1T collaboration are shown in Fig. 1.5. In this thesis, we will focus on the BSM neutrino magnetic moment solution in the presence of both Majorana and Dirac neutrinos.

We stand to learn regardless of whether this excess can be explained by an unknown Tritium background or BSM neutrino magnetic moments. For the former, we would have stronger bounds on the Solar effective neutrino magnetic moments, and for the latter we would open a window into new Physics to explain this larger-than-expected neutrino magnetic moment. Of particular interest to us is how this measurement fits in the grander scheme of direct measurements of neutrino magnetic moments. In particular, we are interested in the neutrino magnetic moment bounds of reactor, accelerator, and Solar neutrino sources when considering Majorana or Dirac neutrinos. We also take an interest in discussing the role future experiments can have in differentiating whether neutrinos are Majorana or Dirac particles.

Recently, the XENON collaboration released results for the XENONnT measurement. These results show no hint of the aforementioned excess [**29**]. In Chapter 3 we will discuss how the XENONnT results all but rule out this anomaly.

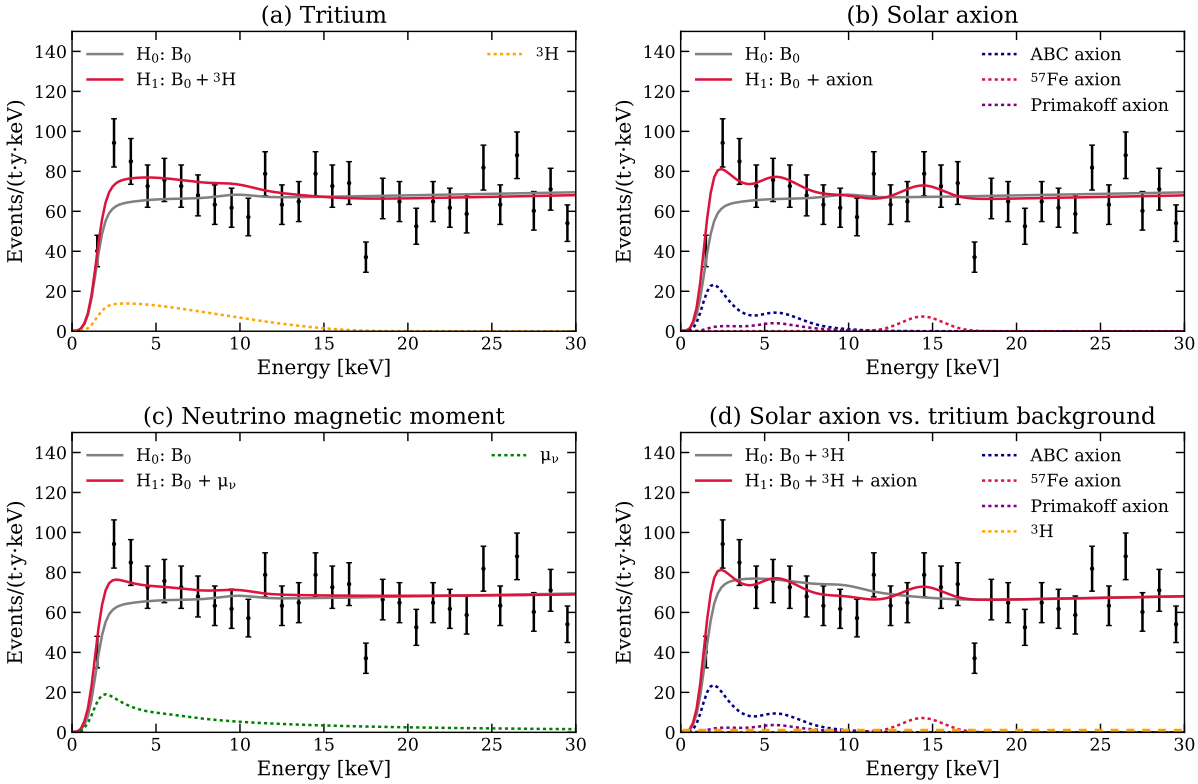

Figure 1.5. Fits to the data under various hypotheses. The null and alternative hypotheses in each scenario are denoted by gray (solid) and red (solid) lines, respectively. For the tritium (a), solar axion (b), and neutrino magnetic moment (c) searches, the null hypothesis is the background model B_0 and the alternative hypothesis is B_0 plus the respective signal. Contributions from selected components in each alternative hypothesis are illustrated by dashed lines. Panel (d) shows the best fits for an additional statistical test on the solar axion hypothesis, where an unconstrained tritium component is included in both null and alternative hypotheses. This tritium component contributes significantly to the null hypothesis, but its best-fit rate is negligible in the alternative hypothesis, which is illustrated by the orange dashed line in the same panel. [**2**]

1.3. In This Dissertation

As noted before, the aim of this thesis is to explore these anomalies and study the role future experiments can play. The first anomaly of interest discussed in Chapter 2

is the tension between the results of the NOvA and T2K experiments when interpreted through the three-neutrino framework. We test whether the addition of a very light sterile neutrino meaningfully softens this discrepancy. Particular care is taken to address statistical pathologies arising from fitting an alternate hypothesis with more degrees of freedom than the null. The second anomaly we consider in Chapter 3 is the XENON1T low energy event excess. We briefly discuss the interpretation of this excess as due to a measurement of non-standard neutrino magnetic moments. We show how the recent XENONnT measurement all but eliminates this possibility. This discussion is done for both cases where neutrinos are either Majorana and Dirac particles. We examine the bounds placed by other experiments such as BOREXINO, LSND, and GEMMA and find that the discovery potential of future experiments depend on the Majorana or Dirac nature of neutrinos. Chapter 4 offers concluding remarks.

This thesis is based on the following works:

- **"Very light sterile neutrinos at NOvA and T2K,"** André de Gouvêa, Giancarlo Jusino Sánchez, and Kevin J. Kelly, Phys. Rev. D **106** 055025 (2022). arXiv:2204.09130
- **"Majorana versus Dirac Constraints on the Neutrino Dipole Moments,"** André de Gouvêa, Giancarlo Jusino Sánchez, Pedro A.N. Machado, and Zahra Tabrizi, arXiv:2209.03373. Submitted for publication in Physical Review D.

CHAPTER 2

Very Light Sterile Neutrinos at NOvA and T2K

2.1. Introduction

Long-baseline neutrino oscillation experiments aim at studying the phenomenon of neutrino oscillations by taking advantage of the known neutrino oscillation lengths, proportional to (the inverse of) the mass-squared differences $\Delta m^2_{21} \equiv m^2_2 - m^2_1$ or $\Delta m^2_{31} \equiv m^3_2 - m^2_1$, where $m_{1,2,3}$ are the masses of the neutrino mass eigenstates $\nu_{1,2,3}$, respectively. The neutrino masses are labelled such that $m^2_2 > m^2_1$ and $|\Delta m^2_{31}| > \Delta m^2_{21}$. With this definition, the sign of Δm^2_{31} is an observable and captures the neutrino-mass ordering: normal ordering (NO) when Δm^2_{31} is positive, inverted ordering (IO) when Δm^2_{31} is negative.

Among the objectives of long-baseline experiments is testing the standard-three-massive-neutrinos paradigm, which states that there are three neutrino mass eigenstates and that these interact via neutral-current and charged-current weak interactions. As far as the charged-current weak interactions are concerned, three orthogonal linear combinations of $\nu_{1,2,3}$ couple to the W-boson and the charged leptons ℓ_α ($\alpha = e, \mu, \tau$). In more detail, $\nu_\alpha = U_{\alpha i}\nu_i$ ($i = 1, 2, 3$) couples to ℓ_α and the W-boson, and $U_{\alpha i}$ are the elements of the unitary leptonic mixing matrix. On the other hand, assuming the standard-three-massive-neutrinos paradigm is correct, long-baseline experiments are capable of measuring, sometimes with great precision, the neutrino oscillation parameters – the parameters which

define $U_{\alpha i}$ and the mass-squared differences. One way to test the standard-three-massive-neutrinos paradigm is to assume it is correct; measure the oscillation parameters using different oscillation processes or different experimental setups; and compare the results. If different measurements of the same quantity disagree at a high confidence level, we would claim the underlying formalism – in this case the standard three-massive-neutrinos paradigm – is deficient.

Among the current generation of long-baseline experiments are the Tokai to Kamioka experiment (T2K) [**17, 3**], in Japan, and the NuMI Off-axis ν_e Appearance (NOvA) experiment [**18, 1**], in the United States. They are sensitive to several of the neutrino oscillation parameters, including some that are, at present, virtually unknown: the neutrino mass-ordering and the CP-odd parameter δ_{CP} that governs whether and how much CP-invariance is violated in the lepton sector. Data from T2K and NOvA have been analyzed assuming the standard-three-massive-neutrinos paradigm and have led to interesting measurements of the oscillation parameters. Just as interesting, perhaps, is the fact that there is some tension between T2K and NOvA data.

The tension, which was first demonstrated by Refs. [**30, 31**], has been quantified and examined critically in the three-neutrino framework by various authors [**32, 28, 33, 34**]. In a little more detail, both T2K and NOvA measure electron-like and muon-like events associated to a pion decay-in-flight neutrino source ($\pi \to \mu\nu_\mu$). Measurements are performed at both near and far detectors and the detectors are exposed to both "neutrino" and "antineutrino" beams. With all this information, they can infer the ν_μ and $\overline{\nu}_\mu$ survival probabilities $P(\nu_\mu \to \nu_\mu)$ and $P(\overline{\nu}_\mu \to \overline{\nu}_\mu)$, respectively, and the ν_e and $\overline{\nu}_e$ appearance probabilities $P(\nu_\mu \to \nu_e)$ and $P(\overline{\nu}_\mu \to \overline{\nu}_e)$, respectively. At T2K, typical neutrino energies

are around 600 MeV and the baseline is 295 km. Typical NOvA energies are around 2 GeV and the baseline is 810 km.

Assuming the standard-three-massive-neutrinos paradigm, the T2K and NOvA disappearance data are consistent but the appearance data, for both neutrinos and antineutrinos, are in disagreement when analyzed within the NO. If the mass ordering is NO, T2K prefers $\delta_{\rm CP}$ values close to $3\pi/2$.* In contrast, when analyzed under the NO, NOvA data have no strong preference for any particular value of $\delta_{\rm CP}$, however, they disfavor the combination of $\delta_{\rm CP}$ and the mixing angle $\sin^2\theta_{23}$ preferred by T2K at roughly 2σ confidence. This tension may be addressed by instead considering the IO, where both experiments prefer $\delta_{\rm CP} \approx 3\pi/2$ [**32, 3, 1**]. However, global fits to all neutrino oscillation data [**28, 33, 34**] (particularly including those from reactor antineutrino experiments [**35, 36, 37**]), as well as comparisons with cosmological observations [**38, 39**], prefer NO at $\sim 2-3\sigma$, leaving the T2K-NOvA tension unaddressed.

Whether the tension can be alleviated by the presence of physics beyond the standard-three-massive-neutrinos paradigm has also been the subject of intense exploration (see, for example, Refs. [**40, 41, 42, 43, 44, 45, 46**]). Here, we would like to explore, in some detail, whether the tension between T2K and NOvA can be interpreted as evidence for new light neutrino states. This issue has been discussed before [**42**], assuming the new neutrino state ν_4 with mass m_4 is relatively heavy: $|\Delta m^2_{41}| \gg |\Delta m^2_{31}|$. Instead, here we concentrate on $|\Delta m^2_{41}|$ values that are $\mathcal{O}(|\Delta m^2_{31}|)$ or smaller, down to $\mathcal{O}(\Delta m^2_{21})$, and explore the full parameter space associated with the fourth neutrino. In Sec. 2.2, we describe the four-neutrino oscillation formalism of interest. We also discuss how the existence of a light

*We will use the convention that CP-violating phases are defined over $[0, 2\pi]$.

fourth neutrino may help alleviate the T2K–NOvA tension. In Sec. 2.3 we present our simulations of NOvA and T2K data and discuss how these are used, in Sec. 2.4, to compare the standard-three-massive-neutrinos paradigm and the fourth-neutrino hypothesis. We present some concluding remarks in Sec. 2.7. Some results are included in appendices: Appendix A.1 includes detailed numerical results from our analyses, Chapter 2.5 presents an alternate, extremely-light sterile neutrino analysis, and Chapter 2.6 discusses some Monte Carlo studies of T2K, NOvA, and their combination in light of the sterile neutrino analyses.

2.2. Four-Flavor Neutrino Oscillations

We assume there are four neutrino mass eigenstates $\nu_{1,2,3,4}$, and that these are related to the four interaction eigenstates $\nu_{e,\mu,\tau}$ and ν_s (where we assume the ν_s state does not participate in the weak interactions) via a 4×4 unitary mixing matrix:

$$U = R(\theta_{34})R(\theta_{24},\delta_{24})R(\theta_{14},\delta_{14})R(\theta_{23})R(\theta_{13},\delta_{13})R(\theta_{12}), \tag{2.2.1}$$

where R are 4×4 rotation matrices in the ij-plane associated with a rotation angle θ_{ij}. The nontrivial entries of the different R in Eq. (2.2.1) are given by

$$R(\theta_{ij}) = \begin{pmatrix} c_{ij} & s_{ij} \\ -s_{ij} & c_{ij} \end{pmatrix} \qquad R(\theta_{ij},\delta_{ij}) = \begin{pmatrix} c_{ij} & s_{ij}e^{-\delta_{ij}} \\ -s_{ij}e^{\delta_{ij}} & c_{ij} \end{pmatrix},$$

where $c_{ij} = \cos\theta_{ij}$ and $s_{ij} = \sin\theta_{ij}$. This extension to the standard-three-massive-neutrinos paradigm includes one more independent mass-squared difference and five new mixing parameters: three mixing angles $(\theta_{14},\theta_{24},\theta_{34})$ and two complex phases $(\delta_{14},\delta_{24})$.

The 4×4 mixing matrix is defined in such a way that, in the limit $\theta_{14}, \theta_{24}, \theta_{34} \to 0$, $\nu_4 = \nu_s$ and $\nu_{1,2,3}$ are linear superpositions of only the active states $\nu_{e,\mu,\tau}$. In this limit, we recover the standard-three-massive-neutrinos paradigm. We will be interested in the case where $\theta_{14}, \theta_{24}, \theta_{34}$ are relatively small and will refer to $\nu_{1,2,3}$ as the mostly active states. The mostly active states will be defined in the usual way, including the ordering of their masses, which is either "normal" (NO) or "inverted" (IO), as discussed in Sec. 2.1. With this in mind, we define

$$\Delta m^2_{4l} \equiv \begin{cases} m^2_4 - m^2_1, & \text{if } m_1 < m_3 \text{ (NO)} \\ m^2_4 - m^2_3, & \text{if } m_3 < m_1 \text{ (IO)} \end{cases} . \tag{2.2.2}$$

In order to allow for all different relevant orderings of the four masses, we allow for both the NO and IO of the mostly active states and for both positive and negative values of Δm^2_{4l}. The four qualitatively different mass orderings are depicted in Fig. 2.1. As far

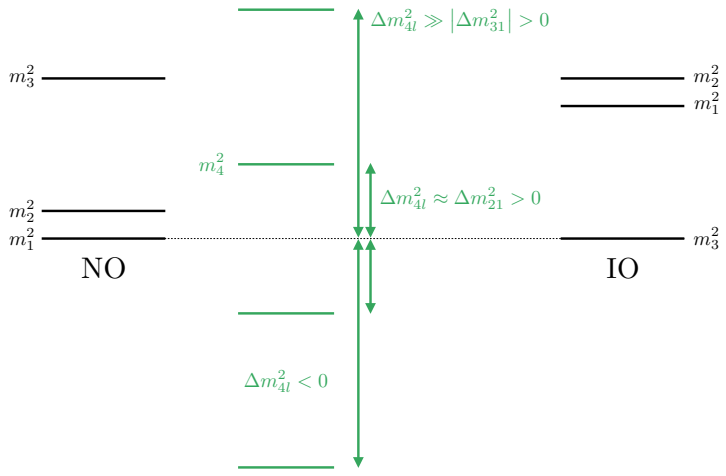

Figure 2.1. Definition, including the sign convention, of Δm^2_{4l} given the NO or IO for the mostly active states.

as the magnitude of Δm^2_{4l}, we will restrict our analyses to $(10^{-5} < |\Delta m^2_{4l}| < 10^{-1})$ eV^2. Inside this range, we expect nontrivial oscillation effects to manifest themselves in the far detectors of T2K and NOvA but not in the corresponding near detectors. When $|\Delta m^2_{4l}|$ is smaller than 10^{-5} eV^2, the new oscillation length associated to Δm^2_{4l} is too long and outside the reach of T2K and NOvA. Instead, when $|\Delta m^2_{4l}|$ is larger than 10^{-1} eV^2, we expect very fast oscillations in the far detectors of T2K and NOvA and nontrivial effects in the corresponding near detectors. This region of parameter space was explored in Ref. [**42**].

The active neutrinos interact with the medium as they propagate from the source to the far detector. These interactions modify the equations that govern the flavor evolution of the neutrino states via effective potentials for forward charged-current (CC) and neutral-current (NC) scattering. The neutrino flavor evolution equation can be written as a Schrödinger-like equation with an effective Hamiltonian given by, in the flavor basis, $H_F = 1/(2E_\nu)(U\mathbf{M}^2U^\dagger + \mathbf{A})$, where

$$\text{(2.2.3)} \qquad \mathbf{M}^2 = \begin{pmatrix} 0 & 0 & 0 & 0 \\ 0 & \Delta m^2_{21} & 0 & 0 \\ 0 & 0 & \Delta m^2_{31} & 0 \\ 0 & 0 & 0 & \Delta m^2_{41} \end{pmatrix}, \qquad \mathbf{A} = \begin{pmatrix} 2E_\nu V_{\rm CC} & 0 & 0 & 0 \\ 0 & 0 & 0 & 0 \\ 0 & 0 & 0 & 0 \\ 0 & 0 & 0 & -2E_\nu V_{\rm NC} \end{pmatrix}.$$

For neutrinos, $V_{\rm CC} = -2V_{\rm NC} = 3.8 \times 10^{-5}$ (eV^2/ GeV)$\rho[\frac{\rm g}{\rm cm^3}]$ are the CC and NC matter potentials, respectively. The CC and NC matter potentials arise from active-neutrino interactions with electrons and all matter particles, respectively – because the NC interaction is identical for all active neutrinos but absent for the sterile neutrino, it appears

with a negative sign in the "sterile-sterile" element of Eq. (2.2.3), $\mathbf{A}_{ss} = -2E_\nu V_{\rm NC}$. For antineutrinos, the matter potentials have the opposite sign. ρ is the density – assumed to be constant – of the medium, assumed to be neutral. When neutrality is assumed, $V_{\rm NC}$ is half as large as $V_{\rm CC}$ and negative. For the NOvA and T2K experiments, we fix the baselines to be $L_{\rm NOvA} = 810$ km and $L_{\rm T2K} = 295$ km, respectively, while the near-far detector average matter densities are taken to be, respectively, $\rho_{\rm NOvA} = 2.8$ g/cm^3 [**1**] and $\rho_{\rm T2K} = 2.6$ g/cm^3 [**3**].

We are interested in improving the quality of fits to the combined T2K and NOvA data, particularly in the ν_e and $\overline{\nu}_e$ appearance channels. If allowing for a fourth neutrino, with $|\Delta m^2_{4l}| \approx 10^{-2}$ eV^2, then the oscillation probability $P(\nu_\mu \to \nu_e)$ will change significantly for the baseline lengths and energies of interest for the two experiments. To try to understand this potential fit improvement, we show in Fig. 2.2 the oscillation probabilities for (anti)neutrinos at T2K and NOvA under the best-fit three-neutrino hypothesis, with parameters given in the 3ν IO column of Table 2.1 and obtained with the analyses described below. Similarly, we also present the best-fit oscillation probabilities at these energies under the four-neutrino hypothesis for the best fit we obtain, with oscillation parameters also given in the 4ν IO column of Table 2.1. We also allow $\sin^2\theta_{34}$ to vary beyond the nominal value of 0.56 in Table 2.1, in order to demonstrate that it has a noticeable impact (despite not appearing in the vacuum-calculated oscillation probabilities), especially at NOvA. Upon inspection of Fig. 2.2, we highlight two main reasons that the effects at T2K and NOvA may be different. One is that the dominant values of L/E, keeping in mind that both beams have a narrow energy profile, are not identical for the

two experiments. This means that for relatively "fast" Δm^2_{4l} the value of the new oscillation phase will not be the same for the two experiments. The other is that the matter effects are more pronounced at NOvA relative to T2K. These allow the effective oscillation frequencies and mixing parameters to be distinct at the two experimental setups.

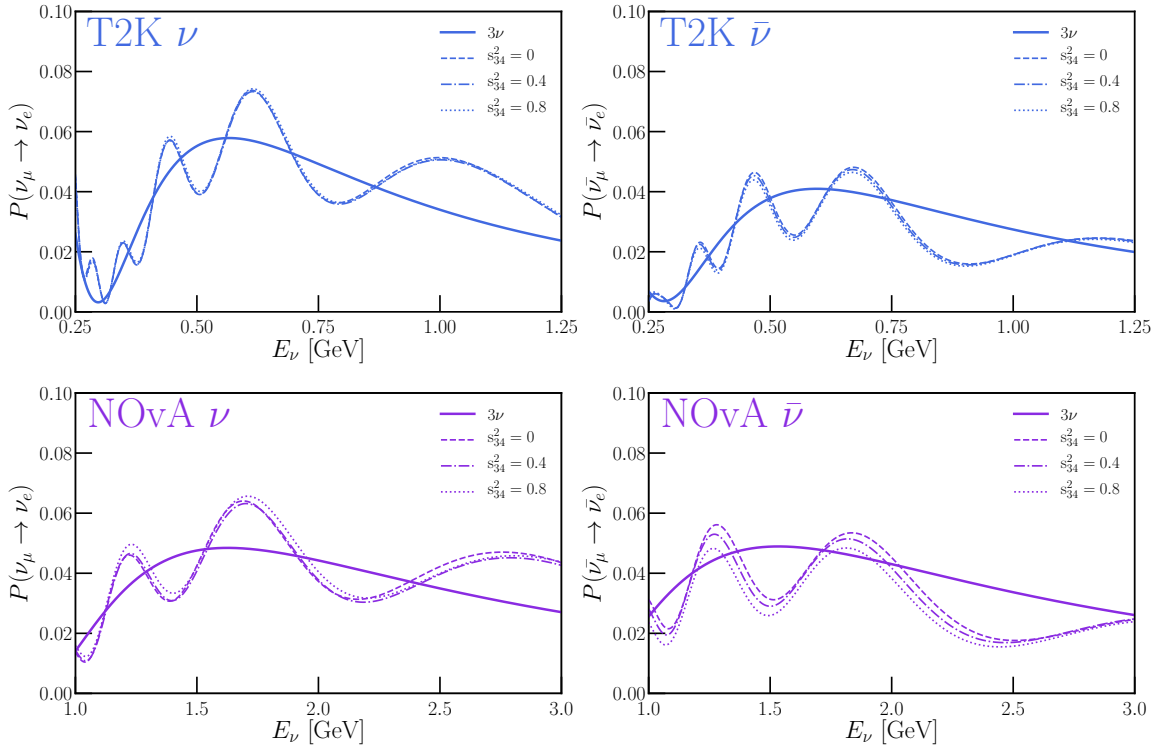

Figure 2.2. Appearance oscillation probabilities at T2K (top, blue) and NOvA (bottom, purple) comparing three-neutrino oscillation probabilities (solid lines, parameters from Table 2.1, column 2 "3ν IO") against four-neutrino ones (non-solid lines, parameters from Table 2.1, column 4 "4ν IO"). Left panels show probabilities for neutrino oscillation, whereas right ones show antineutrino oscillation. For the four-neutrino probabilities, three choices of $\sin^2\theta_{34}$ are used for illustrative purposes: dashed/dot-dashed/dotted lines correspond to $\sin^2\theta_{34} = 0/0.4/0.8$.

In vacuum, $P(\nu_\mu \to \nu_e)$ does not depend on θ_{34}; this is not the case in matter. An easy way to see this is to express the propagation Hamiltonian in the mass basis. In the absence of matter effects, the dependency on the mixing parameters is encoded in the initial and final interaction eigenstates and since neither ν_e nor ν_μ, when expressed as linear superpositions of the mass eigenstates, depend on θ_{34}, then neither can $P(\nu_\mu \to \nu_e)$. Instead, when the matter effects are present, the matter potential in the mass basis depends on θ_{34}. Hence we expect $P(\nu_\mu \to \nu_e)$ to also depend on θ_{34} as long as matter effects are relevant. The dependency on θ_{34} can be seen in Fig. 2.2. As expected, it is rather small at T2K and larger at NOvA, where matter effects are relatively more pronounced.

Another nontrivial aspect of four-neutrino oscillations for T2K and NOvA is the sterile-sterile component of the matter potential, $\mathbf{A}_{ss}$. As discussed above, for a sterile neutrino, $\mathbf{A}_{ss} = -2E_\nu V_{\mathrm{NC}}$, but a fourth active neutrino would have $\mathbf{A}_{ss} = 0$, or equivalently, $V_{\mathrm{NC}} = 0$. Fig. 2.3 depicts the ratio of the appearance probabilities in matter relative to what those would be in vacuum. We show this comparison for the three-neutrino hypothesis (solid lines) as well as the four-neutrino one, where we compare the two hypotheses, $V_{\mathrm{NC}} = -1/2V_{\mathrm{CC}}$ (a sterile neutrino) and 0 (an active one). Here, we see that the "sterileness" of the fourth neutrino has an observable impact on the oscillation probabilities at both T2K and especially NOvA. We emphasize however that all of the analyses below make the more theoretically-robust assumption that the fourth neutrino is sterile and $V_{\mathrm{NC}} = -1/2V_{\mathrm{CC}}$.

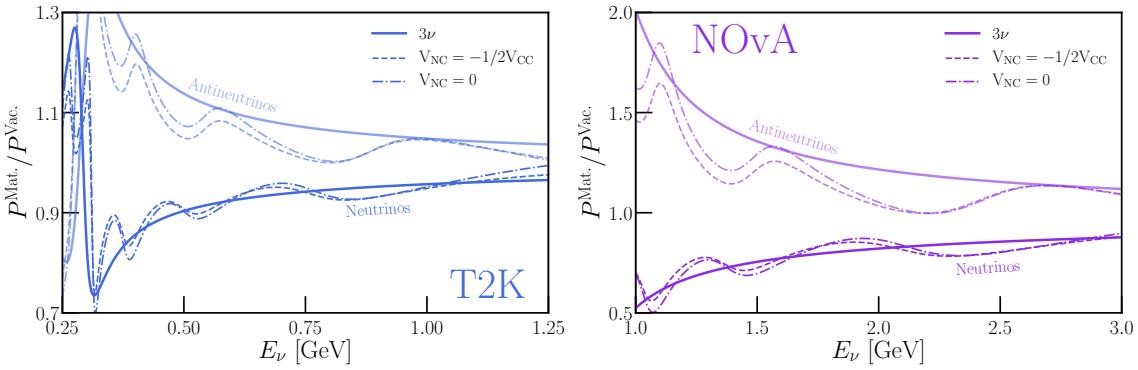

Figure 2.3. Ratio of appearance oscillation probabilities in matter to those in vacuum at T2K (left) and NOvA (right). Solid lines correspond to the three-neutrino oscillation probabilities. Dashed and dot-dashed lines correspond to a fourth neutrino that is sterile or active, respectively. Parameters are taken from columns 2 and 4 from Table 2.1 corresponding to the three-neutrino and four-neutrino cases, respectively.

2.3. Simulating Data from NOvA and T2K

As discussed earlier, both NOvA and T2K operate with beams with a flux of predominantly ν_μ ($\overline{\nu}_\mu$) when operating in (anti)neutrino mode. Both experiments' far detectors are designed to study the disappearance of ν_μ and $\overline{\nu}_\mu$, as well as the appearance of ν_e and $\overline{\nu}_e$. Using the most recent publications from NOvA [**1**] and T2K [**3**], and building off the simulations of Refs. [**47, 48, 32**], we perform simulations to determine the expected event rates in the disappearance and appearance channels of both experiments given a set of three- or four-neutrino oscillation parameters. We then compare these expected event rates against the experiments' published event rates and construct a test statistic using Poissonian bin expectations.

In the remainder of this section, we briefly explain the process by which we simulate the expected event rates, as well as the number of data points for each experiment that

Table 2.1. Oscillation parameters assumed when depicting oscillation probabilities and expected event rates. The four columns correspond to the three-neutrino (3ν) and four-neutrino (4ν) hypotheses, as well as whether the three mostly-active neutrinos follow the normal (NO) or inverted (IO) mass ordering.

Parameter	3ν NO	3ν IO	4ν NO	4ν IO
$\sin^2\theta_{12}$	0.307	0.307	0.321	0.314
$\sin^2\theta_{13}$	0.022	0.022	0.023	0.023
$\sin^2\theta_{23}$	0.57	0.57	0.43	0.45
$\Delta m^2_{21}/10^{-5}$ eV^2	7.53	7.53	7.53	7.53
$\Delta m^2_{31}/10^{-3}$ eV^2	2.51	-2.41	2.49	-2.39
$\delta_{\rm CP}$	3.66	4.71	4.09	4.46
$\sin^2\theta_{14}$	—	—	0.043	0.021
$\sin^2\theta_{24}$	—	—	0.060	0.053
$\sin^2\theta_{34}$	—	—	0.37	0.56
$\Delta m^2_{41}/$eV^2	—	—	1.1×10^{-2}	-1.1×10^{-2}
δ_{14}	—	—	0.01	4.88
δ_{24}	—	—	1.82	5.89

enter our test statistic. To center our discussion, we will rely on several benchmark sets of oscillation parameters with which we calculate the expected observables at NOvA and T2K. We adopt two benchmark sets each for the 3ν and 4ν assumptions, listed in Table 2.1, allowing for the mostly-active neutrinos to follow either the normal (NO) or inverted (IO) orderings. As we will discuss in Section 2.4, these parameters are the best-fit points obtained by our fit to the *combination* of T2K and NOvA under the different hypotheses.

NOvA — Our simulation of NOvA, designed to match the results of Ref. [**1**], includes the disappearance channels of neutrino and antineutrino mode (19 bins each, with neutrino energies ranging from 0 to 5 GeV) as well as event rate measurements of the appearance

channels[†], totaling 40 data points. This simulation corresponds to a total exposure of 13.6×10^{20} (12.5×10^{20}) protons on target (POT) in (anti)neutrino mode.

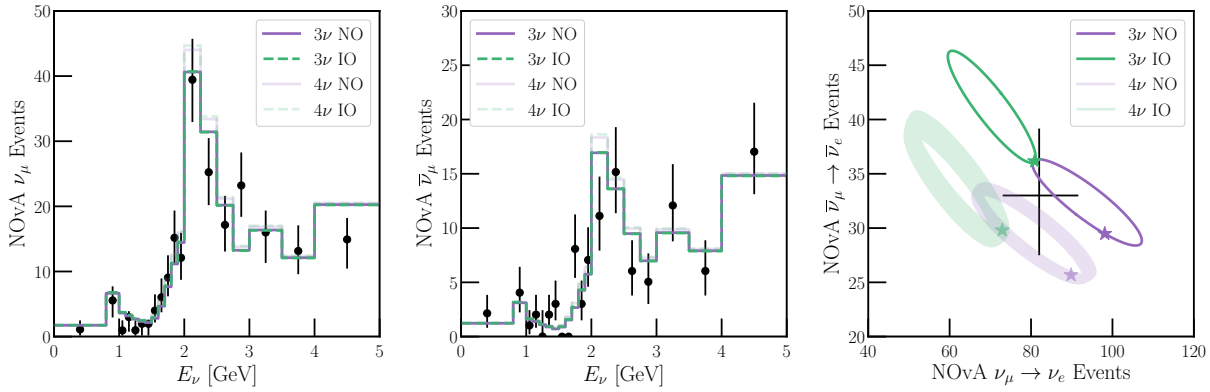

Figure 2.4. Expected and observed event rates in NOvA's ν_μ disappearance (left), $\overline{\nu}_\mu$ disappearance (center), and $\nu_e/\overline{\nu}_e$ appearance (right) channels. We compare the prediction under the 3ν (solid/dashed lines) and 4ν (faint lines/regions) hypotheses, with parameters from Table 2.1, with the observed data (black). Purple curves correspond to the mostly-active neutrinos following the normal mass ordering (NO), where green ones correspond to the inverted mass ordering (IO). In the right panel, the CP-violating phases are allowed to vary in the predicted rates. Data points from Ref. [**1**].

Fig. 2.4 shows the expected event rates in NOvA for neutrino mode ν_μ disappearance (left), antineutrino mode $\overline{\nu}_\mu$ disappearance[‡] (center), and a joint comparison of neutrino (x-axis) and antineutrino (y-axis) mode $\nu_\mu \to \nu_e$ (or $\overline{\nu}_\mu \to \overline{\nu}_e$) appearance (right panel). We compare the NOvA benchmark oscillation predictions, using the parameters in Table 2.1 (purple histograms/curves[§] for NO, green for IO, and dark curves for 3ν, faint ones

[†]For simplicity, we sum the expected event rate for the entire neutrino energy range and compare it against the observed 82 (33) appearance events of operation in (anti)neutrino mode. We have compared this approach to one that includes the spectral information of the appearance channels and find no qualitative impact on our results.

[‡]In contrast to Ref. [**1**], our disappearance channel panels depict the event rate per bin as opposed to event rate per unit energy, causing our higher-energy bins (with larger bin width) to appear exaggerated.

[§]Where the faint curves are not visible in the left/center panels, the four-neutrino hypothesis predicts the same rate as the three-neutrino one(s).

for 4ν), to the observed event rates from the experiment (black). Error bars here are only statistical. In the left and center panels, all oscillation parameters are fixed according to Table 2.1. In contrast, the right panel allows $\delta_{\rm CP}$ to vary for the 3ν curves, and all three CP-violating phases to vary in the 4ν case. This allows for a set of ellipses in this bi-event parameter space instead of a single one. In the right panel, stars indicate the predicted event rates when the CP-violating phases are fixed to their values in Table 2.1.

T2K — We simulate T2K in much the same spirit as NOvA, with the goal of matching the results presented in Ref. [**3**]. In the case of T2K, the disappearance channels each consist of 30 bins – 100 MeV in width from 0 to 2.9 GeV, and one bin corresponding to neutrino energies above 2.9 GeV. For the appearance channel, we take advantage of the expected neutrino-energy spectrum with bins of 125 MeV width from 0 to 1.25 GeV in each channel.[¶] This yields 80 data points in our T2K analysis. Our T2K simulation corresponds to an exposure of 14.94×10^{20} (16.35×10^{20}) POT in (anti)neutrino mode operation.

Similar to Fig. 2.4, we show in Fig. 2.5 our expected event rates in the different T2K channels – the left panel is for ν_μ disappearance, center for $\overline{\nu}_\mu$ disappearance, and the right panel is the combined ν_e and $\overline{\nu}_e$ appearance. For clarity of display, we sum the total expected event rates in the ν_e and $\overline{\nu}_e$ channels in the right panel. Here, the oscillation parameters correspond to those given in Table 2.1 and, in the right panel, the CP-violating phases are allowed to vary.

Test Statistic — We take the expected and observed event rates in NOvA (40 data points), T2K (80), or a combination of them (120) and construct a test statistic using

[¶]Refs. [**47, 48**], however, have demonstrated that total-rate measurements of T2K's appearance channel result in similar parameter estimation to the collaboration's results.

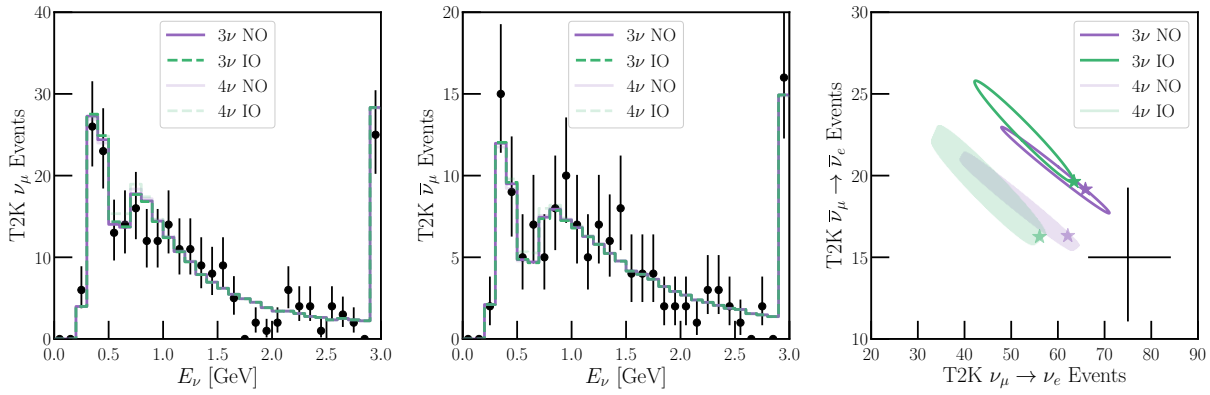

Figure 2.5. Expected and observed event rates in T2K's ν_μ disappearance (left), $\overline{\nu}_\mu$ disappearance (center), and $\nu_e/\overline{\nu}_e$ appearance (right) channels. We compare the prediction under the 3ν (solid/dashed lines) and 4ν (faint lines/regions) hypotheses, with parameters from Table 2.1, with the observed data (black). Purple curves correspond to the mostly-active neutrinos following the normal mass ordering (NO), where green ones correspond to the inverted mass ordering (IO). In the right panel, the CP-violating phases are allowed to vary in the predicted rates. Data points from Ref. [**3**].

Poisson statistics for the log-likelihood (matching a χ^2 function in the limit of large event rates):

$$\chi^2 = \sum_{i \,\in\, \text{bins}} -2\left(-\lambda_i + x_i + x_i \log\left(\frac{\lambda_i}{x_i}\right)\right), \tag{2.3.1}$$

where λ_i (x_i) represents the expected (observed) event rate in bin i for a given experiment/channel.

We will be interested in several pieces of information from the test statistic in Eq. (2.3.1). When performing parameter estimations, we will use contours of $\Delta\chi^2$ about its minimum to represent preferred regions/intervals of parameter space. When comparing best-fit points under different hypotheses, i.e., comparing preference for the 4ν scenario over the

3ν one, we will compare the minimum χ^2 when varying over oscillation parameters, taking into account the number of degrees of freedom in such a fit.

Analysis & Priors — The main focus of this work is on the long-baseline experiments NOvA and T2K, which are sensitive to oscillation effects associated with mass-squared differences of order of 10^{-3} eV^2. On the other hand, the solar mass-squared difference has been well-measured by solar neutrino [**49, 50**] and reactor antineutrino [**51**] experiments to be $\Delta m^2_{21} = 7.53 \times 10^{-5}$ eV^2 while the associated mixing angle is measured to be $\sin^2\theta_{12} = 0.307$, both at the few percent level. Due to the lack of sensitivity to these quantities at NOvA/T2K, we fix them[‖] in our analyses. While NOvA and T2K are sensitive to $\sin^2\theta_{13}$ through their appearance channels, their measurement capability is significantly weaker than that of Daya Bay [**35**], RENO [**36**], and Double Chooz [**37**] reactor antineutrino experiments. In our fits, we include Daya Bay's measurement as a Gaussian prior on the quantity $4|U_{e3}|^2(1-|U_{e3}|^2) = 0.0856 \pm 0.0029$, which is $\sin^2(2\theta_{13})$ when considering the three-neutrino hypothesis [**35**].

2.4. Results

This section details the results of our analyses. First, in Section 2.4.1, we summarize the results of fits of our NOvA and T2K simulations and their combination under the three-neutrino hypothesis. Then, Section 2.4.2 discusses the results of these fits under the four-neutrino hypothesis, including a comparison of the three-neutrino and four-neutrino hypotheses.

[‖]Specifically, we fix the matrix-element-squared $|U_{e2}|^2$, which is equal to $\sin^2\theta_{12}\cos^2\theta_{13}\cos^2\theta_{14}$ in the four-neutrino framework, to its best-fit value of 0.300. This causes $\sin^2\theta_{12}$ to vary for large θ_{14}.

2.4.1. Three-Neutrino Results

Our first three-neutrino analysis is focused on finding the best-fit points of each experimental analysis (T2K, NOvA, and a combined fit). For this, we perform two fits for each experiment/combination, one assuming that neutrinos follow the normal mass ordering (NO, $\Delta m^2_{31} > 0$) and one assuming that they follow the inverted one (IO, $\Delta m^2_{31} < 0$). Recent results have demonstrated that, under the three-neutrino hypothesis, T2K and NOvA each exhibit mild preference for the NO over the IO, but their combination has a mild preference for the IO [**32, 28, 33, 34**]. When combined with all reactor antineutrino data and other experimental results, the global preference is for the NO at relatively low significance.

We find a result consistent with these previous results, summarized in Table 2.2. As in all of our analyses, Δm^2_{21} and $\sin^2\theta_{12}$ are fixed, and a prior is included from the results of Daya Bay on $\sin^2(2\theta_{13})$. We present both the overall test statistic at this best-fit point for each analysis as well as the preference for the NO over the IO in the right-most column (positive values indicate preference for NO, negative for IO). We note here that all of the best-fit χ^2 obtained are comparable to (and in the case of T2K and the joint fit, less than) the number of degrees of freedom, implying that these are all good fits to their respective data sets. Finally, we see that the joint-fit χ^2 under the NO hypothesis is around five units of χ^2 larger than the sum of the two individual fits whereas, under the IO hypothesis, it is roughly the same – this highlights the so-called NOvA/T2K tension, where the results disagree under the NO hypothesis but not under the IO one. The values from the "Joint" fit in Table 2.2 correspond to the benchmark values we adopted in the three-neutrino case in Table 2.1.

Table 2.2. Best-fit parameters of our analyses of T2K, NOvA, and a combined analysis of the two under the three-neutrino hypothesis. We determine the best-fit point under the normal (NO) and inverted (IO) mass-ordering hypotheses, as well as the overall preference for the NO over IO, $\Delta\chi^2_{\mathrm{NO,IO}}$, for each analysis. In each, a prior on $\sin^2(2\theta_{13})$ from Daya Bay is included, and $\sin^2\theta_{12} = 0.307$ and $\Delta m^2_{21} = 7.53 \times 10^{-5}$ eV^2 are fixed to their best-fit points from other experimental results.

3ν		$\sin^2\theta_{13}$	$\sin^2\theta_{23}$	$\Delta m^2_{31}/10^{-3}$ eV^2	δ_{CP}	χ^2	$\Delta\chi^2_{\mathrm{NO,IO}}$
T2K	NO	0.022	0.56	2.52	4.58	66.82	1.48
	IO	0.022	0.56	−2.41	4.71	68.19	
NOvA	NO	0.022	0.58	2.52	2.34	43.40	0.14
	IO	0.022	0.57	−2.41	4.78	43.55	
Joint	NO	0.022	0.57	2.51	3.67	115.58	−3.76
	IO	0.022	0.57	−2.41	4.72	111.82	

We also perform a parameter estimation under the three-neutrino hypothesis, both to prepare our expectations for the four-neutrino analyses and to validate our results compared against the official results of the experimental collaborations. The free/fixed parameters and test statistic are identical to those when determining the best-fit points. For simplicity, we perform an analysis of the parameters $\sin^2\theta_{13}$, $\sin^2\theta_{23}$, Δm^2_{31}, and δ_{CP} and marginalize over $\sin^2\theta_{13}$ and Δm^2_{31} (including both the NO and IO hypotheses), and present the joint measurement of $\sin^2\theta_{23}$ and δ_{CP}.

Fig. 2.6 presents the results of this analysis at 2σ (dashed, filled contours) and 3σ (solid lines) CL for T2K (blue), NOvA (purple), and the joint fit (green). Stars of each color represent the best-fit points obtained in Table 2.2. Once the mass ordering is marginalized, NOvA has no sensitivity to δ_{CP}, and constrains $\sin^2\theta_{23}$ to be between roughly 0.37 and 0.65 at 3σ CL. In the NO, NOvA can take on nearly any value of δ_{CP}, however it disfavors the combination $\delta_{CP} = 3\pi/2$, $\sin^2\theta_{23} > 1/2$ at relatively high significance. Under the IO,

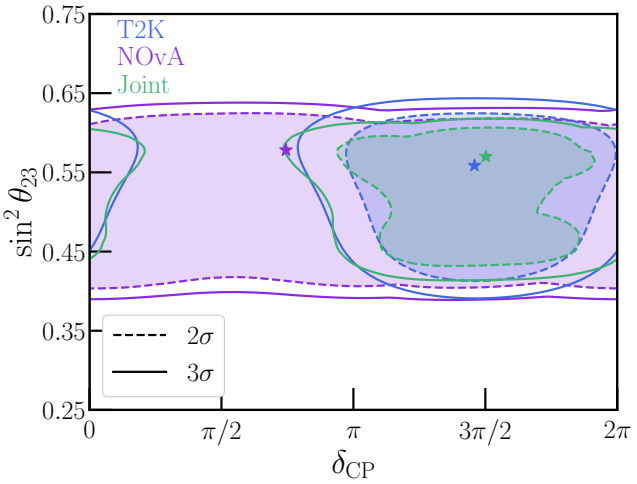

Figure 2.6. Parameter estimation of δ_{CP} and $\sin^2\theta_{23}$ from T2K (blue), NOvA (purple), and their combination (green) at 2σ (dashed lines) and 3σ (solid lines) CL.

NOvA prefers this combination. Regardless of the mass ordering, T2K prefers $\delta_{\mathrm{CP}} = 3\pi/2$ and constrains $\sin^2\theta_{23}$ to be in a similar range as NOvA. When the two are combined, the preferred regions are very similar to those obtained in the fit to T2K data alone.

2.4.2. Four-Neutrino Results

We begin our four-neutrino analyses by repeating the process that led to Table 2.2 – we determine the best-fit points under the four-neutrino hypothesis for T2K, NOvA, and their combination. Now that we are considering four-neutrino oscillations, we allow for all four mass orderings discussed in Sec. 2.2 (see Fig. 2.1). This amounts to dividing the analysis based on the signs of Δm^2_{31} and Δm^2_{4l}, where l represents m_1 in the NO and m_3 in the IO, the lightest of the mostly-active neutrinos.

Table 2.3 summarizes these twelve analyses (four each for NOvA, T2K, and their Joint fit), giving the best-fit parameters as well as the overall χ^2 of each fit in the four-neutrino hypothesis. Near the bottom we give the preferred ordering of masses from each experiment/combination – T2K and the Joint fit both prefer $m_4 < m_3 < m_1 < m_2$, where NOvA prefers $m_1 < m_2 < m_3 < m_4$. The preference for the sign of Δm^2_{4l} is small in all cases – individual fit results for all four mass orderings and all three experimental combinations are provided for completeness in Appendix A.1. When allowing for a fourth neutrino, neither T2K nor NOvA have a strong preference for the sign of Δm^2_{31}. T2K prefers $\Delta m^2_{31} < 0$ at $\Delta\chi^2 = 0.1$, where NOvA prefers $\Delta m^2_{31} > 0$ at $\Delta\chi^2 = 0.02$. However, the combined fit prefers $\Delta m^2_{31} < 0$ at $\Delta\chi^2 = 4.6$ an even stronger preference for negative Δm^2_{31} than when data are analyzed under the three-neutrino hypothesis.

The bottom row of Table 2.3 presents the improvement in each experimental analysis (as well as the combined one) compared to the results of the three-neutrino analysis. We find that the fits to both the T2K* and NOvA data improve by roughly five units in χ^2, and the combined fit improves by nearly nine units. However, we note two very important caveats here:

(1) The results of the three-neutrino fit in Table 2.2 demonstrate that, relative to the number of degrees of freedom, good fits have been achieved. So, when comparing the three-neutrino fit – four parameters – to the four-neutrino one – ten parameters – one must take into account the fact that this minimization is being performed over an additional six parameters.

*This result is consistent with what the T2K collaboration reported in Ref. [**52**], which found an improvement of $\Delta\chi^2 = 4.7$.

Table 2.3. Best-fit parameters of the four-neutrino analyses of T2K, NOvA, and their combination. We allow for all possible orderings of the neutrino mass eigenstates, hence Δm^2_{31} and Δm^2_{4l} can each be negative. In each analysis, a prior on $|U_{e3}|^2(1-|U_{e3}|^2)$ from Daya Bay is included, and $|U_{e2}|^2 = 0.300$ and $\Delta m^2_{21} = 7.53 \times 10^{-5}$ eV^2 are fixed to their best-fit points from other experimental results.

4ν	T2K	NOvA	Joint
$\sin^2\theta_{13}$	0.024	0.022	0.023
$\sin^2\theta_{23}$	0.43	0.44	0.43
$\Delta m^2_{31}/10^{-3}$ eV^2	-2.39	2.43	-2.39
$\delta_{\rm CP}$	4.41	0.00	4.46
$\sin^2\theta_{14}$	7.8×10^{-2}	6.9×10^{-3}	4.3×10^{-2}
$\sin^2\theta_{24}$	4.1×10^{-2}	1.2×10^{-1}	6.0×10^{-2}
$\sin^2\theta_{34}$	0.78	0.29	0.37
$\Delta m^2_{4l}/$eV^2	-8.5×10^{-3}	1.0×10^{-2}	-8.5×10^{-3}
δ_{14}	1.82	3.51	4.88
δ_{24}	2.64	3.15	5.89
$\chi^2_{4\nu}$	61.95	38.10	102.83
Ordering	$m_4 < m_3 < m_1 < m_2$	$m_1 < m_2 < m_3 < m_4$	$m_4 < m_3 < m_1 < m_2$
$\chi^2_{3\nu} - \chi^2_{4\nu}$	4.87	5.30	8.99

(2) When determining the statistical significance, the comparison of $\chi^2_{3\nu}-\chi^2_{4\nu}$ must be scrutinized to see whether these test statistics follow a χ^2 distribution. We have performed some basic Monte Carlo studies of our T2K and NOvA simulations (see Chapter 2.6) and found that, when statistical fluctuations are considered, one will often find best-fit points with $\Delta m^2_{4l} \approx 10^{-2}$ eV^2 that improve each experiment's fit by a couple of units of χ^2. This is likely driven by the sizes of the energy bins (around 100 MeV) used in the T2K and NOvA analyses – at T2K/NOvA baselines/energies, a new oscillation driven by a mass-squared splitting of 10^{-2}

eV^2 will evolve significantly[†] over the span of a single bin. This new fast oscillation can "absorb" individual bins' statistical fluctuations and lead to an artificial improvement in the test statistic. This is validated by the results of Ref. [**52**], which found that an improvement of $\Delta\chi^2 = 4.7$ at T2K (between the three-neutrino and four-neutrino hypotheses) corresponds to only $\sim 1.0\sigma$ preference for a fourth neutrino, in contrast with the preference derived assuming Wilks' theorem [**53**] holds, $\sim 1.7\sigma$.

When considering the results of Table 2.3 (and that the best-fit points are close to $|\Delta m^2_{4l}| \approx 10^{-2}$ eV^2) in light of these two caveats, we find that, while a very light sterile neutrino improves the "tension" between T2K and NOvA, there is not strong evidence in favor of a four-neutrino hypothesis over the three-neutrino one.

In order to determine whether the sterile neutrino solution to the NOvA/T2K tension persists in light of caveat 2 above, we also perform an alternate analysis in Chapter 2.5 where we restrict $\Delta m^2_{21} \lesssim |\Delta m^2_{4l}| < 10^{-3}$ eV^2. This allows us to avoid fast oscillations in the T2K/NOvA far detectors and any statistical pathologies that may arise. We find that there remains a preference for four neutrinos over three neutrinos at a level of $\Delta\chi^2 = 4.1$. While this is smaller than what we observed for $|\Delta m^2_{4l}| \approx 10^{-2}$ eV^2, it is nevertheless comparable to the preference for non-standard interactions as a solution to this tension found in Refs. [**40, 43**] at the level of $\Delta\chi^2 \approx 4.4 - 4.5$.

We generalize this best-fit procedure by, instead of minimizing over all parameters (including Δm^2_{4l}), scanning over Δm^2_{4l} values. We again allow for both positive and negative values of this new mass-squared difference and for both the normal and inverted

[†]For this Δm^2, the argument of the term $\sin^2(\Delta m^2 L/4E_\nu)$ that enters the oscillation probabilities changes by an appreciable fraction of π.

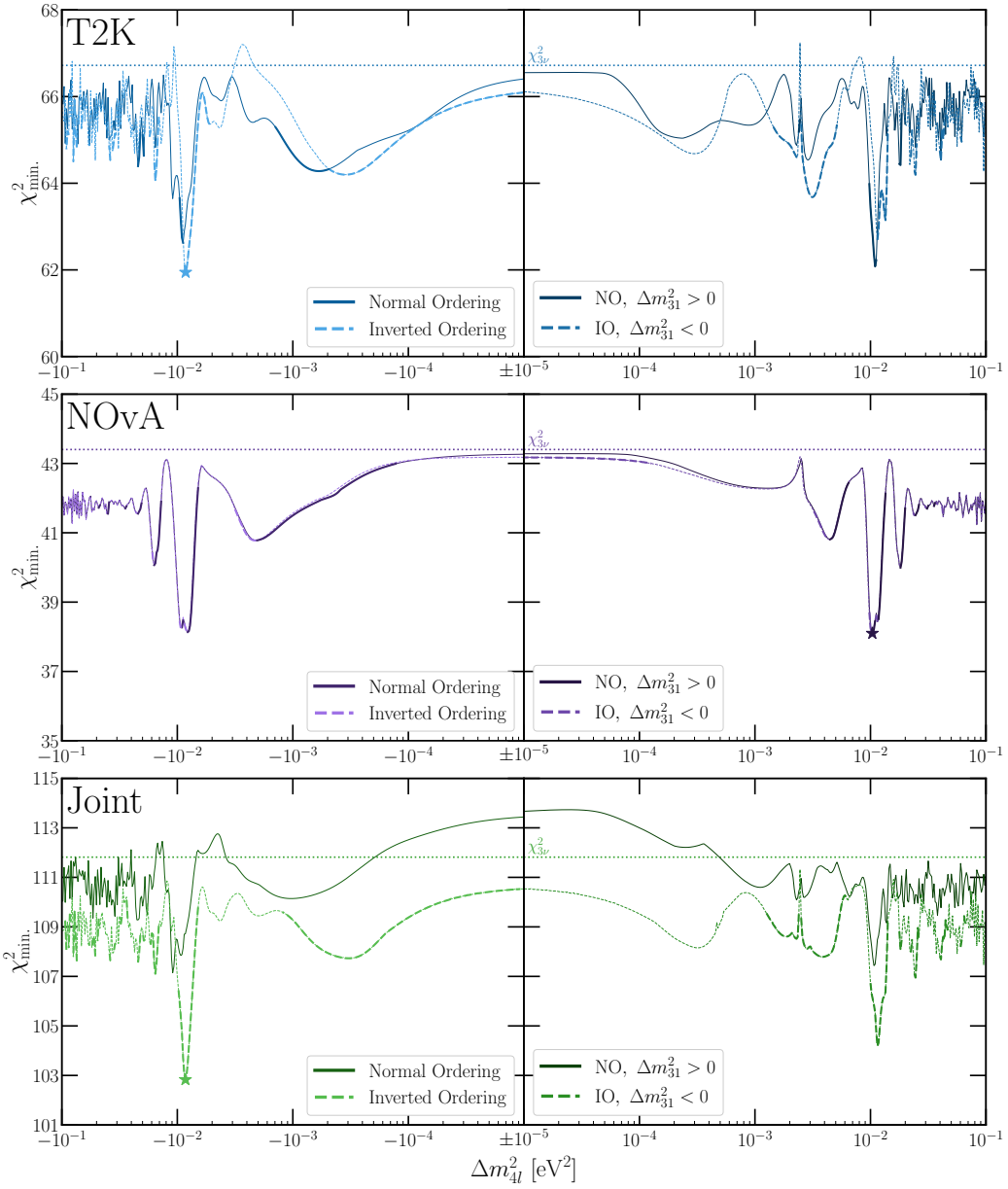

Figure 2.7. Best-fit χ^2 obtained using our analysis of T2K (top, blue), NOvA (middle, purple), and a joint fit of the two (bottom, green) as a function of different values of Δm^2_{4l}. Different tones within each panel indicate different mass orderings (the signs of Δm^2_{31} and Δm^2_{4l}). The minimization has been performed across all other oscillation parameters except for θ_{12} and Δm^2_{21}, which are fixed.

mass orderings for the three mostly active states. Fig. 2.7 presents the results of this approach. The top panels (blue lines) show the results for T2K, middle panels (purple) for NOvA, and bottom panels (green) for the combined analysis. In each row, the left (right) panel corresponds to negative (positive) values of Δm^2_{4l}. Dark (light) lines in each case correspond to the NO (IO) among the mostly-active neutrinos. Dashed lines in each panel indicate the best-fit χ^2 under the three-neutrino hypothesis presented in Table 2.2. Stars indicate the overall best-fit point of each analysis (when considering all different mass orderings), and lines are made bold if they constitute the minimum χ^2 for a given experimental analysis for all of these choices of mass orderings.

The findings of Table 2.3 (and the corresponding tables in Appendix A.1) are borne out in Fig. 2.7, showing that the fits prefer $|\Delta m^2_{4l}| \sim 10^{-2}$ eV^2 in all cases, with moderate improvements relative to the three-neutrino fits. Above, we discussed the possibility that this preference has to do with the energy resolution and binning of the experiments and the statistical significance when interpreting confidence levels from $\Delta\chi^2$ may be overstated. If we restrict ourselves to $|\Delta m^2_{4l}| \lesssim 10^{-3}$ eV^2 to avoid this concern, we still find moderate preference for a fourth neutrino – see Chapter 2.5 for further discussion.

Moving on from best-fit determinations, we now construct constraints on the new parameters, specifically $\sin^2\theta_{24}$ and Δm^2_{4l} (the ones to which these experiments have the greatest sensitivity). In order to present constraints at a particular confidence level and compare against other literature results, we assume for this exercise that Wilks' theorem holds [**53**]. After marginalizing over the remaining oscillation parameters (still fixing $|U_{e2}|^2$ and Δm^2_{21}), we present 2σ CL constraints from T2K (blue) and NOvA (purple) in Fig. 2.8. In generating these constraints, we have marginalized over the signs of both

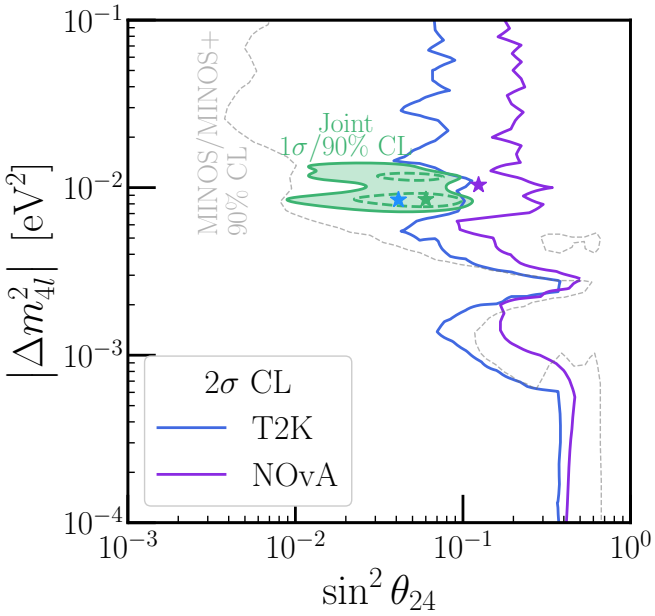

Figure 2.8. Constraints on $\sin^2\theta_{24}$ vs. Δm^2_{4l} at 2σ CL from T2K (blue) and NOvA (purple) after marginalizing over all other parameters (except for $|U_{e2}|^2$ and Δm^2_{21}, which are fixed and a prior from Daya Bay on $|U_{e3}|^2$ – see text), including the signs of Δm^2_{31} and Δm^2_{4l}. The green region indicates the preferred region from a combined analysis at 1σ (dashed) and 90% (solid) CL, and the grey, dashed line shows the 90% CL constraint from MINOS/MINOS+ [**4**]. All confidence levels presented here are derived assuming Wilks' theorem holds.

Δm^2_{31} and Δm^2_{4l}. Colored stars indicate the best-fit point in $(\sin^2\theta_{24}, |\Delta m^2_{4l}|)$ of the given fits. In Fig. 2.8 we also compare against the 90% CL constraint from the MINOS/MINOS+ experiment [**4**] as a faint grey line.[‡] Finally, we also present in green the preferred region at 1σ/90% CL[§] ($\Delta\chi^2 = 2.3,\ 4.61$ assuming Wilks' theorem for two parameters) by our combined T2K and NOvA analysis. This result is in tension with that of the MINOS/MINOS+ result, however, our preferred region has not been Feldman-Cousins

[‡]This result assumed Δm^2_{31} and Δm^2_{41} to both be positive, however, due to the lack of mass-ordering sensitivity at MINOS, the result likely does not depend strongly on this choice.

[§]We choose 90% CL for clarity (the 2σ CL region spans the entire range of $|\Delta m^2_{4l}|$ of the figure and a comparable region of $\sin^2\theta_{24}$) and for a direct comparison against the MINOS/MINOS+ result.

corrected, and the results would likely agree if a higher confidence level were assumed. T2K has reported constraints in the $\sin^2\theta_{24}$ vs. Δm^2_{41} parameter space in Ref. [**52**] – we find comparable results here despite the simplified assumptions we have made in our analysis and the slightly larger data set considered in this work.

While Fig. 2.8 compares constraints and preferred regions in the parameter space $\sin^2\theta_{24}$ vs. $|\Delta m^2_{4l}|$, it is also important to consider the parameters that have been marginalized in this construction. For concreteness, we focus on the preferred region (green) from the combined T2K/NOvA analysis that we have performed. The best-fit point, at $|\Delta m^2_{4l}| = 8.5 \times 10^{-3}$ eV^2, corresponds to mixing angles

$$\left\{\sin^2\theta_{14},\ \sin^2\theta_{24},\ \sin^2\theta_{34}\right\} = \left\{4.3\times10^{-2},\ 6.0\times10^{-2},\ 0.37\right\}, \tag{2.4.1}$$

or mixing-matrix elements

$$\left\{|U_{e4}|^2,\ |U_{\mu4}|^2,\ |U_{\tau4}|^2\right\} = \left\{4.3\times10^{-2},\ 5.7\times10^{-2},\ 0.33\right\}. \tag{2.4.2}$$

For these low values of $|\Delta m^2_{4l}|$, the strongest constraints on $|U_{e4}|^2$ come from reactor antineutrino oscillation experiments such as Daya Bay [**54**] and Bugey-3 [**55**]. A combined analysis [**56**] constrains $\sin^2\theta_{14} \lesssim 4\times10^{-3}$ at 90% CL, in significant tension with the value found in Eq. (2.4.1).

Constraints on $|U_{\tau4}|^2$ are more difficult to extract, as they often arise in tandem with $|U_{\mu4}|^2$ and depend strongly on Δm^2_{41} [**57**]. While specific constraints in this region of $|\Delta m^2_{4l}|$ have not been explicitly derived, $|U_{\tau4}|^2 = 0.33$ is possibly in tension with existing results from neutrino experiments. T2K, which analyzed its neutral-current data in addition to the data sets considered here, has constrained $|U_{\tau4}|^2 \lesssim 0.5$ for both

$\Delta m^2_{41} = 3 \times 10^{-3}$ eV^2 and 0.1 eV^2 at 90% CL [**52**]. Atmospheric neutrino experiments, including Super-Kamiokande [**58**] and IceCube [**59**] have constrained $|U_{\tau 4}|^2 \lesssim 0.2$ at high confidence, however, these analyses are restricted to $\Delta m^2_{41} \gtrsim 0.1$ eV^2 where the fourth-neutrino-driven oscillations are averaged out. A more thorough investigation of this 10^{-2} eV^2 regime would prove useful if this hint persists in future NOvA/T2K data.

Lastly, we also note that for such large $|U_{\alpha 4}|^2$ and small m_4, this fourth neutrino would thermalize with the SM in the early universe and remain relativistic and in thermal equilibrium throughout much of the universe's evolution. Such thermalized light species are in tension with cosmological observations surrounding the Cosmic Microwave Background and Big-Bang Nucleosynthesis – we refer the reader to Ref. [**60**] for further discussion on these effects. Regardless, if such a light sterile neutrino truly is behind any tension between NOvA and T2K, additional work is necessary to resolve tension between this terrestrial solution and cosmological observations.

When discussing Fig. 2.7, we considered the possibility of analyzing only the region $|\Delta m^2_{4l}| \lesssim 10^{-3}$ eV^2, in part to avoid concerns regarding energy resolution and bin widths. We noted that in that region, a solution to the NOvA/T2K tension persists with a preference of $\Delta\chi^2 \approx 4.1$. This regime has the added benefit that constraints from MINOS/MINOS+ (as seen in Fig. 2.8), Daya Bay/Bugey-3/others, and Super-Kamiokande/IceCube are considerably weaker. Such an *extremely-light* sterile neutrino, as we discuss in Chapter 2.5, with $|\Delta m^2_{4l}| \approx 7 \times 10^{-4}$ eV^2 should be paid particular attention as more data from T2K and NOvA are unveiled, especially if any tension between the two persists.

T2K and NOvA will continue collecting data – if a very light sterile neutrino does in fact exist with $|\Delta m^2_{4l}| \approx 10^{-2}$ eV^2, more data will continue to shed light and potentially

lead to a discovery. In the next generation, the Deep Underground Neutrino Experiment (DUNE) [**19**] and Hyper-Kamiokande (HK) [**20**] experiments will have sensitivity to light sterile neutrinos in the same region of $|\Delta m_{4l}|^2$ given that they operate in a similar L/E_ν as NOvA and T2K. The two experiments, and any combined analysis, will have excellent sensitivity to test this solution to the T2K/NOvA tension [**61, 62**].

2.5. Alternative Analyses with Very Small Mass-Squared Difference

We find, in Section 2.4, a solution to the NOvA/T2K tension with a new, light sterile neutrino with a mass-squared difference $|\Delta m^2_{4l}| \approx 10^{-2}$ eV^2. However, there are technical challenges associated with this relatively large mass-squared difference for the NOvA/T2K analyses, also as discussed in Section 2.4. For those reasons, we choose to pursue a different version of the analyses from the main text, this time restricting ourselves to $|\Delta m^2_{4l}| \leq 10^{-3}$ eV^2. As with the analyses in the main text, we fix Δm^2_{21} to its best-fit value (7.53×10^{-5} eV^2).

First, we illustrate how the oscillation probabilities $P(\nu_\mu \to \nu_e)$ and $P(\overline{\nu}_\mu \to \overline{\nu}_e)$ at T2K/NOvA energies and baselines behave for a very light sterile neutrino, similar to the discussion in Section 2.2 (see Fig. 2.2). Instead of a relatively large $|\Delta m^2_{4l}| \approx 10^{-2}$ eV^2, Fig. 2.9 depicts the impact of a new mass-squared difference $\Delta m^2_{4l} = -3.4 \times 10^{-4}$ eV^2 (and an inverted mass ordering for the three mostly-active neutrinos). The remaining oscillation parameters we use are from the "Joint" column in Table 2.4, corresponding to the best-fit parameters of the combined T2K and NOvA analysis when the new mass-squared difference is restricted to be $|\Delta m^2_{4l}| \leq 10^{-3}$ eV^2.

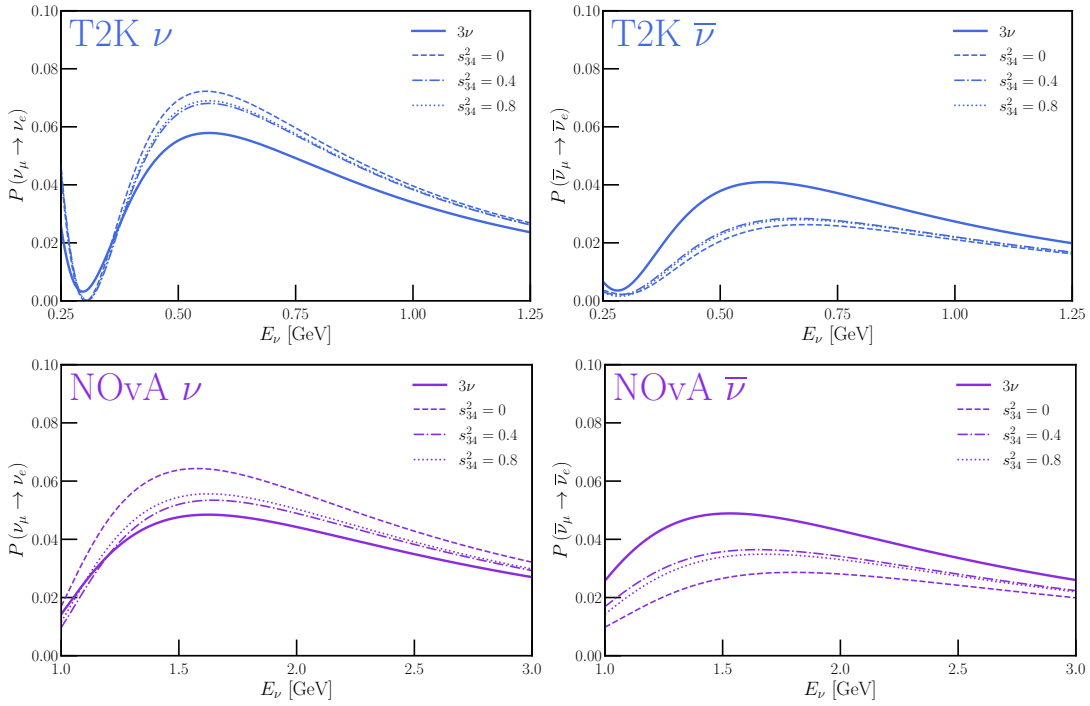

Figure 2.9. Oscillation probabilities at T2K (top) and NOvA (bottom) comparing three-neutrino oscillation probabilities (solid lines, parameters from Table 2.1) against four-neutrino ones (non-solid lines, parameters from the "Joint" column in Table 2.4). Left panels show probabilities for neutrino oscillation, whereas right ones show antineutrino oscillation. For the four-neutrino probabilities, three choices of $\sin^2\theta_{34}$ are used for demonstration: dashed/dot-dashed/dotted lines correspond to $\sin^2\theta_{34} = 0,\ 0.4,\ 0.8$.

The top panels of Fig. 2.9 show oscillation probabilities at T2K, and the bottom panels at NOvA; the left (right) panels correspond to neutrino (antineutrino) oscillations. As with Fig. 2.2, we allow $\sin^2\theta_{34}$ to vary to demonstrate its nontrivial impact on these oscillation probabilities – the dashed/dot-dashed/dotted lines correspond to $\sin^2\theta_{34} = 0,\ 0.4,\ 0.8$, respectively. Compared with Fig. 2.2, here the "new" oscillation length driven by $\Delta m^2_{21} < |\Delta m^2_{4l}| < |\Delta m^2_{31}|$ is relatively long as a function of the neutrino energy, leading at zeroth order to an overall shift in normalization relative to the three-neutrino

oscillation probabilities. Across the energies of interest for T2K and NOvA, this leads to larger values of $P(\nu_\mu \to \nu_e)$ and smaller values of $P(\overline{\nu}_\mu \to \overline{\nu}_e)$. As in Fig. 2.2, the impact of nonzero $\sin^2\theta_{34}$ is more prevalent for NOvA, with its longer baseline, than for T2K. Fig. 2.10 depicts the impact of matter effects for this relatively smaller value of Δm^2_{4l} and is to be compared to Fig. 2.3.

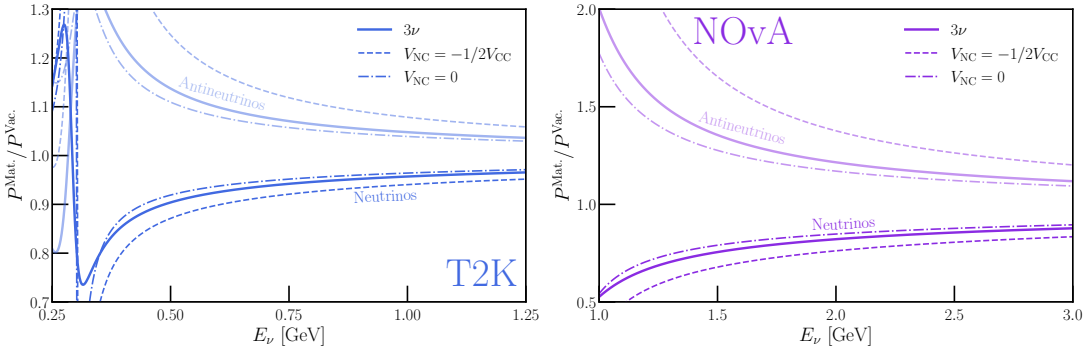

Figure 2.10. Ratio of oscillation probabilities, similar to Fig. 2.3, considering an extremely light sterile neutrino with $\Delta m^2_{4l} = -3.4 \times 10^{-4}$ eV^2 and oscillation parameters as given in Table 2.4.

The best-fit points obtained from this low-Δm^2_{4l} fit to T2K data, NOvA data, and the combined data sets are listed in Table 2.4. As in the result discussed in the main text, NOvA favors NO for the mostly active states while T2K and the Joint fits favor the IO for the mostly active states. All fits point to m_4 as the lightest neutrino mass. The improvement relative to the three-neutrinos scenario is largest for the Joint fit – a little over four units of χ^2 – but rather modest. In summary, the data do not significantly favor the four-neutrino hypothesis over the three-neutrino one.

Fig. 2.11 depicts the region of the $|\Delta m^2_{4l}| \times \sin^2\theta_{24}$ parameter space that is allowed by the combination of T2K and NOvA data at the one-sigma level, including all possible four-neutrino mass orderings (see Fig. 2.1) and assuming $|\Delta m^2_{4l}|$ is less than 10^{-3} eV^2,

along with the 2σ constraints from NOvA (purple) and T2K (blue). The stars indicate the best-fit points and the dashed line existing bounds from MINOS/MINOS+. Unlike the result discussed in the main text, here the best fit point is not in tension with existing neutrino oscillation bounds thanks to the more limited sensitivity of MINOS/MINOS+ and reactor antineutrino experiments to new mass-squared differences less than 10^{-3} eV^2.

Like the results discussed in the main text, here, the best-fit points in Table 2.4 all prefer large values of $\sin^2\theta_{34}$, i.e., they suggest that ν_4 has an $\mathcal{O}(1)$ ν_τ component. As discussed in Section 2.4, while large $\sin^2\theta_{34}$ are excluded by existing data, relevant constraints were obtained only for relatively large $|\Delta m^2_{4l}| \gtrsim 0.1$ eV^2.

Table 2.4. Best-fit parameters of our 4ν analyses when restricted to $|\Delta m^2_{4l}| \leq 10^{-3}$ eV^2. Other details identical to Table 2.3.

4ν	T2K	NOvA	Joint
$\sin^2\theta_{13}$	0.025	0.022	0.026
$\sin^2\theta_{23}$	0.41	0.63	0.53
$\Delta m^2_{31}/10^{-3}$ eV^2	-2.37	2.44	-2.39
$\delta_{\rm CP}$	4.05	2.98	4.21
$\sin^2\theta_{14}$	0.13	6.2×10^{-3}	0.14
$\sin^2\theta_{24}$	8.2×10^{-2}	6.1×10^{-2}	7.6×10^{-2}
$\sin^2\theta_{34}$	0.63	0.79	0.48
$\Delta m^2_{4l}/$eV^2	-3.5×10^{-4}	-1.0×10^{-3}	-3.4×10^{-4}
δ_{14}	4.66	2.77	5.34
δ_{24}	5.04	3.21	5.39
$\chi^2_{4\nu}$	64.20	41.50	5.39
Ordering	$m_4<m_3<m_1<m_2$	$m_4<m_1<m_2<m_3$	$m_4<m_3<m_1<m_2$
$\chi^2_{3\nu}-\chi^2_{\rm 4nu}$	2.62	1.90	4.11

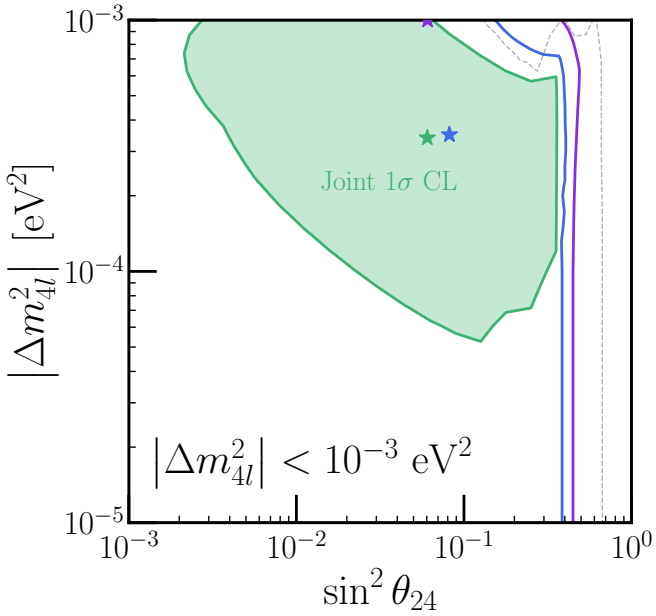

Figure 2.11. Similar to Fig. 2.8 but under the analysis assumption that $|\Delta m^2_{4l}| < 10^{-3}$ eV^2.

2.6. Test Statistic Studies and Pseudoexperiments

Section 2.4 demonstrated that all three fits, those to the T2K and NOvA data individually as well as their combination, prefer the four-neutrino hypothesis over the three-neutrino one to some degree of confidence. This is expected, as the three-neutrino hypothesis is a subset of the four-neutrino one – what is more difficult to predict is the level at which this preference is found. Specifically, we found that the best-fit-point to the data under the four-neutrino hypothesis compared to that of the three-neutrino hypothesis for T2K, NOvA, and the joint fit exhibited a preference at the level of $\Delta\chi^2 = 4.87,\ 5.30$, and 8.99, respectively. Also in Section 2.4, we discussed the fact that these three fits tend to favor $|\Delta m^2_{4l}| \approx 10^{-2}$ eV^2 and opined on whether this is a coincidence due to the binning used by T2K and NOvA or a real, physical effect.

In this chapter, we attempt to quantify some of these observed challenges – how significant these preferences are, and whether the preferred new mass-squared splitting is spurious. To do so, we perform a number of pseudoexperiments corresponding to each analysis. We simulate data for each experiment assuming the three-neutrino hypothesis is true, assuming $\sin^2\theta_{12} = 0.304$, $\sin^2\theta_{13} = 0.0212$, $\sin^2\theta_{23} = 0.532$, $\Delta m^2_{21} = 7.53 \times 10^{-5}$ eV^2, $\Delta m^2_{31} = 2.45 \times 10^{-3}$ eV^2, and $\delta_{\rm CP} = 4.39$ (given as reference values in Ref. [**3**]). For each pseudoexperiment, we include Poissonian fluctuations on the expected data according to this hypothesis. Then, using the same analysis strategies as in the main text, we obtain the best-fit-points and χ^2 values for the three-neutrino and four-neutrino hypotheses.

The normalized distribution of $\Delta\chi^2 \equiv \chi^2_{3\nu} - \chi^2_{4\nu}$ is shown in Fig. 2.12. We show the histograms obtained by performing pseudoexperiments of the three different analyses in solid, colored lines, compared against the $\Delta\chi^2$ obtained when analyzing the data as vertical, dashed lines. We also display the χ^2 distribution assuming six degrees of freedom (corresponding to the difference between the number of parameters in the two analysis hypotheses) as a grey line, which seems to track the distribution of the joint-fit pseudoexperiments well. As a result of this procedure, we can determine the statistical significances of the three preferences – the p-values of the observed data at T2K, NOvA, and their combination are 0.53, 0.21, and 0.22, respectively. These values correspond to preference for the four-neutrino hypothesis at the level of 0.58σ, 1.26σ, and 1.22σ – none of which corresponds to a significant preference.

Finally, we determine whether the best-fit points obtained when analyzing data, all with $|\Delta m^2_{4l}| \approx 10^{-2}$ eV^2 are expected when including Poissonian fluctuations of simulated three-neutrino data. We determine, for each pseudoexperiment, the best-fit values of

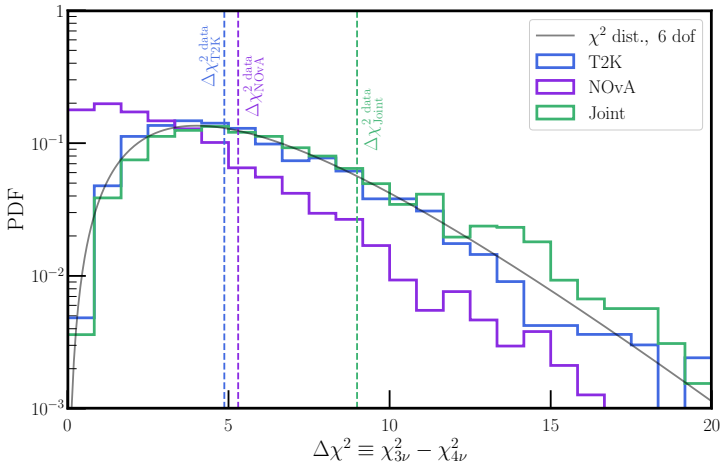

Figure 2.12. Preference for the four-neutrino hypothesis over the three-neutrino one as indicated by pseudoexperiments simulating T2K (blue), NOvA (purple), and their combination (green). We also display the PDF of the chi-squared distribution assuming six degrees of freedom (grey), as well as the preferences indicated when analyzing the actual data sets (dashed lines).

$\sin^2\theta_{24}$ and $|\Delta m^2_{4l}|$ obtained when analyzing the pseudodata under the four-neutrino hypothesis, displaying the distributions of these best-fit values in Fig. 2.13. Here, the dark regions indicate where the fits prefer the combination of parameters most frequently, and the white stars show the best-fit parameters obtained in each analysis from Section 2.4. For all three analyses, the best-fit obtained when analyzing the data is nearly exactly consistent with the most likely points obtained by these procedures. This indicates that such fit values of $|\Delta m^2_{4l}|$ are to be expected due to the construction of the test statistic and the experimental particulars, furthering the evidence that the results obtained in the main text are due to statistical fluctuations instead of the actual presence of a fourth, very light neutrino.

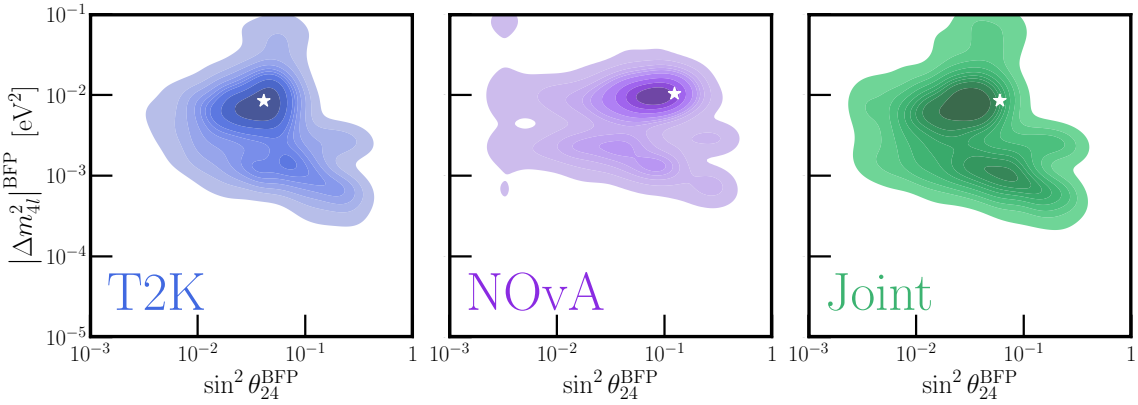

Figure 2.13. Best-fit values of $\sin^2\theta_{24}$ and $|\Delta m^2_{4l}|$ obtained when performing pseudoexperiments of T2K (left), NOvA (center), and their combination (right). White stars in each panel indicate the best-fit values of these parameters when analyzing the corresponding data set. In the colored distributions, darker (lighter) colors indicate regions where the fit prefers the values more (less) frequently.

2.7. Concluding Remarks

As more data from neutrino oscillation experiments are collected, we are able to test the standard-three-massive-neutrinos paradigm with better precision. Concurrently, there is always the possibility that disagreements arise, especially when data from multiple experiments are analyzed. In these instances, exploring different explanations of such tensions is invaluable, whether they are related to statistical fluctuations, deeper systematic issues, or new physics beyond the standard-three-massive-neutrinos paradigm.

Such a tension has been noted when comparing the latest data from the Tokai to Kamioka (T2K) and NuMI Off-axis ν_e Appearance (NOvA) experiments. These measure the (dis)appearance of ν_e (ν_μ) in a ν_μ beam at relatively long baselines. When analyzed under the three-neutrino hypothesis, their results disagree at around the 90% confidence level. Previous studies of combination T2K and NOvA data have highlighted that this

tension is reduced when, for instance, the inverted neutrino mass ordering is considered instead of the normal ordering [**32, 28, 33, 34**], or when additional, beyond-the-Standard-Model neutrino/matter interactions are included in the analyses [**40, 43**].

We have demonstrated here that an alternative approach can remedy this tension – the addition of a fourth, very light, sterile neutrino. This very light new neutrino would be associated to a mass-squared difference, relative to the lightest mostly-active neutrino, of order 10^{-2} eV^2. We have studied the four-neutrino hypothesis when applied to the T2K and NOvA data independently, as well as their combination. For the combined data, we find that the four-neutrino hypothesis is preferred over the three-neutrino one at the level of $\Delta\chi^2 \approx 9$. When interpreting this in terms of statistical significance, two difficulties arise: first, the number of additional parameters in the four-neutrino hypothesis relative to the three-neutrino one (six additional parameters). Second, the oscillations associated with a new mass-squared difference on the order of 10^{-2} eV^2 are significant within individual bins in these long-baseline experiments, which leads to an artificial preference for sterile neutrinos due to statistical fluctuations.

Due to the second challenge, in order to avoid relatively fast oscillations, we also explored an alternative extremely-light sterile neutrino analysis where the fourth neutrino is fixed to be associated to a mass-squared difference smaller (in magnitude) than 10^{-3} eV^2. In this context, we find moderate improvement relative to the three-neutrino hypothesis, at the level of $\Delta\chi^2 \approx 4$. While this is less significant, it is comparable to the improvement offered by non-standard neutrino interactions and merits further investigation.

NOvA and T2K are still collecting and analyzing data. As they progress, the experiments and combined analyses thereof will allow for deeper testing of these different,

interesting regimes of four-neutrino oscillations with a very light or extremely light fourth neutrino. If they confirm the existence of such a new, light fermion state, then future experiments (including the spiritual successors DUNE and Hyper-Kamiokande) will be able to probe the new particle's properties with even greater precision.

CHAPTER 3

Majorana versus Dirac Constraints on the Neutrino Dipole Moments

3.1. Introduction

While the neutrino charge is zero, massive neutrinos are guaranteed to have a nonzero electromagnetic dipole moment. In the absence of new interactions, the neutrino magnetic dipole moment is generated at the one loop level and is of order $10^{-20}(m_\nu/0.1\text{ eV})\mu_\text{B}$ [**63, 64, 65**], where μ_B is the Bohr magneton. This is several orders of magnitude beyond the sensitivity of current and near future experimental probes. The measurement of a nonzero neutrino electromagnetic dipole moment would imply more new physics in the neutrino sector.

The nature of the neutrino dipole moment depends on whether neutrinos are Majorana fermions or Dirac fermions. It is well known that diagonal dipole moments for Majorana fermions are forbidden and hence these only have transition dipole moments. Dirac fermions, instead, are allowed to have both diagonal and transition dipole moments. We review this carefully in Section 3.2, concentrating on the differences between Dirac and Majorana neutrinos. We also discuss how Majorana neutrinos can "mimic" Dirac neutrinos in the presence of new light neutral fermions.

Nonzero neutrino electromagnetic dipole moments contribute to neutrino–matter scattering, as we discuss in more detail in Section 3.3. Precision measurements of neutrino

scattering, therefore, allow one to constrain their magnitudes. Experiments with reactor antineutrinos and solar neutrinos, for example, exclude effective dipole moments larger than a few times $10^{-11}\mu_B$ [**66, 67**]. In Section 3.4 we list the current laboratory constraints. In the near and intermediate future, better laboratory sensitivity is expected (see, for example, [**68, 69, 70, 71, 72**]). There are also indirect constraints on the neutrino electromagnetic dipole moments from astrophysical processes [**73, 74, 75, 76**]. We comment on those briefly in Section 3.4. Here, we concentrate on laboratory constraints, which we view as complementary to the indirect astrophysical bounds.

Since there are at least three different neutrino flavors, a more careful examination of the experimental data is required. Different experiments constrain different combinations of the neutrino dipole moments. This implies that (a) some combinations of dipole moments are less constrained and (b) one can obtain qualitatively different bounds on the neutrino dipole moments by combining information from different experiments. The interplay of the different data sets also depends on whether neutrinos are Dirac or Majorana fermions. Here we estimate the current bounds on all neutrino dipole moments, taking all possible correlations into account, for both Dirac neutrinos and Majorana neutrinos. We also discuss expectations for future experimental searches. We find, in particular, that expectations depend strongly on whether neutrinos are Majorana or Dirac fermions. These results are presented and discussed in Sec 3.6.

The constraints reported by the experiments are in the form of upper limits on the magnitude of some effective magnetic moment $|\mu^{\text{eff}}|$ (see Section 3.3). These constraints can be translated into the fundamental electromagnetic dipole moments. In recent years,

there have been many efforts connecting these constraints to the parameters of the Lagrangian (see, for example, [**77, 78, 79, 80, 81, 68, 69, 82, 83, 84, 85, 86, 87**]). In most of these studies, special attention was dedicated to the Majorana-neutrino hypothesis. In this case, relative to the Dirac-neutrino hypothesis, there are fewer parameters and the analysis is computationally simpler. For the Dirac-neutrino hypothesis, it is often the case that only constraints on the diagonal magnetic moments are considered in the literature. Here, we present the results of a comprehensive analysis, treating all the parameters as independent from one another. We also discuss is some detail what information is, in principle, experimentally accessible. We make use the experimental data of current solar, reactor and accelerator experiments, including the most recent results from XENONnT [**29**] (also discussed, very recently, in [**86, 87**]), and speculate on the impact of a future accelerator experiment capable of constraining the neutrino dipole moment using a ν_μ "beam." We find that such a future experiment has the potential to make a discovery even when its sensitivity is significantly weaker than the current solar constraints. However, this statement is only true, assuming there are no new light particles, if the neutrinos are Dirac fermions.

The fact that electromagnetic dipole moments and masses are correlated – both require chirality violation – also allows one to estimate how large the neutrino dipole moments could be. In a nutshell, generic new physics that induces nonzero neutrino dipole moments will also contribute to the neutrino masses. If one assumes the new-physics contribution to the neutrino masses is not much larger than the known values, one can place mostly model-independent bounds on the neutrino dipole moments [**88, 89**]. In

[**88**], Bell and collaborators argued that, modulo fine-tuning among different contributions to the neutrino masses, neutrino dipole moments are guaranteed to be less than, roughly, $10^{-15}(m_\nu/0.1\text{ eV})\mu_\text{B}$ if the neutrinos are Dirac fermions. The equivalent upper bound on Majorana neutrinos is a lot weaker. For example, if there is new physics at the weak scale, it is possible to identify scenarios that saturate the current experimental constraints (see, e.g., [**89**] and references therein and [**90**] for a more recent discussion). We return to these issues in Section 3.7, where we also summarize our results and offer other concluding remarks.

3.2. The Electronmagnetic Dipole Moment Matrix

Given two left-handed Weyl fermions χ_a and χ_b with zero electric charge, one can write down the following gauge and Lorentz invariant dimension-five operator that couples the fermions to the electromagnetic field strength $F^{\mu\nu}$:

$$\mathcal{O} = \frac{1}{\Lambda}(\chi_a)^\beta \left[(\sigma_\mu)_{\beta\dot\alpha}(\bar\sigma_\nu)^{\dot\alpha\alpha} - (\sigma_\nu)_{\beta\dot\alpha}(\bar\sigma_\mu)^{\dot\alpha\alpha}\right](\chi_b)_\alpha F^{\mu\nu}, \tag{3.2.1}$$

making use of the standard $\alpha, \dot\alpha = 1, 2$ notation for Weyl fermions, along with the $\epsilon^{\alpha\beta} = -\epsilon^{\beta\alpha}$ metric for raising and lowering spinor indices (there is an equivalent metric for dotted indices), the four-vector $\sigma_\mu, \bar\sigma_\mu$ 2×2–matrices, while Λ denotes an arbitrary energy scale. It is easy to show that, now omitting spinor indices, $\chi_a\sigma_\mu\bar\sigma_\nu\chi_b = \chi_b\sigma_\nu\bar\sigma_\mu\chi_a$ so Eq. (3.2.1) is antisymmetric upon the exchange $a \leftrightarrow b$. This means that Eq. (3.2.1) for $a = b$ vanishes exactly.

If neutrinos are Majorana fermions, each neutrino mass eigenstate ν_i (with mass m_i, $i = 1, 2, \ldots, N$, and N is the number of neutrinos) can be represented as a two-component

left-handed Weyl fermion and the following Lagrangian describes the neutrino–photon interactions at dimension five:

$$\mathcal{L}_{\rm M} = \frac{1}{2}\mu_{ij}\nu_i\sigma_{\mu\nu}\nu_j F^{\mu\nu} + H.c., \tag{3.2.2}$$

where $4\sigma_{\mu\nu} \equiv \sigma_\mu\bar{\sigma}_\nu - \sigma_\nu\bar{\sigma}_\mu$. Here, $\mu_{ij} = -\mu_{ji}$ are complex constants that define the neutrino electromagnetic dipole moment matrix. There are $(N^2-N)/2$ complex, independent μ_{ij}. In the case of three neutrinos, the dipole moment matrix is parameterized by 6 real parameters: $\mu_{ij} = |\mu_{ij}|e^{i\xi_{ij}}$, $ij = 12, 13, 23$.

If neutrinos are Dirac fermions, each neutrino mass eigenstate can be represented as a pair of two-component left-handed Weyl fermions, ν_i, and ν_i^c. In our notation, ν_i have lepton number $+1$ and are referred to as the left-handed neutrino fields while ν_i^c have lepton number -1 and are referred to as the left-handed antineutrino fields. Note that while ν_i couples to weak gauge bosons, ν_i^c does not. When it comes to writing down the electromagnetic dipole moments, terms proportional to $\nu_i\sigma_{\mu\nu}\nu_j$ and $\nu_i^c\sigma_{\mu\nu}\nu_j^c$ violate lepton number and are hence forbidden. We are left with

$$\mathcal{L}_{\rm D} = \mu_{ij}^D\nu_i^c\sigma_{\mu\nu}\nu_j F^{\mu\nu} + H.c.. \tag{3.2.3}$$

Note that we do not include interactions of the type $\nu_i\sigma_{\mu\nu}\nu_j^c$. These are accounted for since, as already mentioned earlier, $\nu_i\sigma_{\mu\nu}\nu_j^c = -\nu_j^c\sigma_{\mu\nu}\nu_i$. With this in mind, μ_{ij}^D define a generic, $N \times N$ complex matrix, parameterized by N^2 complex numbers. In the case of three neutrinos, the dipole moment matrix is parameterized by 18 real parameters, $\mu_{ij}^D = |\mu_{ij}^D|e^{i\xi_{ij}}$, $ij = 11, 12, 13, 21, 22, 23, 31, 32, 33$.

There is a useful way to visually compare the Majorana and Dirac dipole moment matrices. In the Majorana case,

(3.2.4)

$$\mathcal{L}_M = \frac{1}{2}\begin{pmatrix} \nu_1 & \nu_2 & \dots & \nu_N \end{pmatrix}\sigma_{\mu\nu}\begin{pmatrix} 0 & \mu_{12} & \dots & \mu_{1N} \\ -\mu_{12} & 0 & \dots & \mu_{2N} \\ \vdots & \vdots & \ddots & \vdots \\ -\mu_{1N} & -\mu_{2N} & \dots & 0 \end{pmatrix}\begin{pmatrix} \nu_1 \\ \nu_2 \\ \vdots \\ \nu_N \end{pmatrix} F^{\mu\nu} + H.c.,$$

while in the Dirac case, making use of $\nu_i\sigma_{\mu\nu}\nu_j^c = -\nu_j^c\sigma_{\mu\nu}\nu_i$, we can rewrite Eq. (3.2.3) in a more "symmetric" way, so that it looks very much like the Majorana case:

(3.2.5)

$$\mathcal{L}_D = \frac{1}{2}\begin{pmatrix} \nu_1^c & \dots & \nu_N^c & \nu_1 & \dots & \nu_N \end{pmatrix}\sigma_{\mu\nu}\begin{pmatrix} 0 & \dots & 0 & \mu_{11}^D & \dots & \mu_{1N}^D \\ \vdots & \ddots & \vdots & \vdots & \ddots & \vdots \\ 0 & \dots & 0 & \mu_{N1}^D & \dots & \mu_{NN}^D \\ -\mu_{11}^D & \dots & -\mu_{N1}^D & 0 & \dots & 0 \\ \vdots & \ddots & \vdots & \vdots & \ddots & \vdots \\ -\mu_{1N}^D & \dots & -\mu_{NN}^D & 0 & \dots & 0 \end{pmatrix}\begin{pmatrix} \nu_1^c \\ \vdots \\ \nu_N^c \\ \nu_1 \\ \vdots \\ \nu_N \end{pmatrix} F^{\mu\nu} + H.c..$$

For the same number of neutrino species N, the Dirac dipole moment matrix is bigger: $(2N \times 2N)$ versus $(N \times N)$. On the other hand, the Dirac dipole moment matrix has a larger fraction of zero entries; in fact, only 1/4 of the entries in the Dirac case are independent and nontrivial.

It is easy to see that if the number of neutrinos, here defined to be very light neutral fermions, is three, the Dirac case has many more independent dipole moments (18 real parameters) than the Majorana case (6 real parameters). Therefore, if the neutrinos are Majorana fermions, the dipole moment matrix can be over-constrained after one obtains

7 independent bits of information. On the other hand, 19 independent bits are required in order to over-constrain the dipole moment matrix in the Dirac case.* In Section 3.6, this will translate into the fact that the neutrino electromagnetic dipole moments are less constrained if the neutrinos are Dirac fermions.

One is tempted to conclude that, by performing enough measurements of the neutrino dipole moments, it is possible to establish the nature of the neutrinos, Majorana fermions versus Dirac fermions. This is not necessarily the case. If the neutrinos are Majorana fermions, one can mimic the Dirac case by adding more neutrino mass eigenstates. For example, by doubling the number of mass eigenstates, the dimensions of the two dipole moment matrices can be made the same. In this case, in fact, there are more independent dipole moments if the neutrinos are Majorana fermions. Concretely, for six Majorana neutrinos, there are 15 complex dipole moments, compared to the 9 complex dipole moments for three Dirac neutrinos. Five Majorana neutrinos, as a matter of fact, are a better "match" to three Dirac neutrinos: 10 versus 9 complex parameters. As an aside, the number of independent dipole moments first coincides for 1 Dirac neutrino and 2 Majorana neutrinos, followed by 6 Dirac neutrinos and 9 Majorana neutrinos. The next combinations are 35 Dirac neutrinos versus 50 Majorana neutrinos, followed by 204 Dirac neutrinos versus 289 Majorana neutrinos. We did not find other pairings with less than 1000 Dirac neutrinos.

*Whether these "bits of information" are accessible in principle or in practice will be further discussed in the next sections.

3.3. Observing Neutrino Electromagnetic Dipole Moments

A non-zero neutrino electromagnetic dipole moment modifies elastic neutrino–electron, neutrino–nucleon, and neutrino–nucleus scattering. For all processes of interest, the chirality-flipping nature of the magnetic moment, combined with the chirality-conserving nature of the weak interactions and the tiny neutrino masses implies that the contribution from photon-exchange between the neutrino and the charged-fermion of interest will add incoherently to the weak cross section. For $\nu_i + e \to \nu_j + e$ elastic scattering, the dipole-moment contribution to the cross section is

$$\frac{d\sigma_{ij}}{dE_R} = \frac{|\mu_{ji}|^2}{\mu_B^2}\frac{\pi\alpha^2}{m_e^2}\left[\frac{1}{E_R} - \frac{1}{E_\nu}\right], \tag{3.3.1}$$

where E_ν is the energy of the incoming neutrino, E_R is the electron recoil kinetic energy, α is the fine-structure constant, m_e is the electron mass, and $\mu_B \equiv e/2m_e$ is the Bohr magneton. The signature of the dipole moment in neutrino–electron scattering experiments is an excess of recoil electrons that peaks at small recoil kinetic energies. For coherent elastic scattering on nuclei, the cross section is given by Eq. (3.3.1) multiplied by $Z^2F^2(q^2)$, where Z is the atomic number of the target, $F(q^2)$ is the nuclear from factor, and q^2 is the four-momentum transfer [**91**].

Since neutrino masses are negligibly small and the daughter neutrinos cannot, for all practical purposes, be observed directly or indirectly, σ_{ij} is not really an observable. Instead, upon detecting the recoil charged particle, one measures $\sigma_i \equiv \sum_j \sigma_{ij}$. For neutrino–electron scattering,

$$\frac{d\sigma_i}{dE_R} = \frac{|\mu_i^{\text{eff}}|^2}{\mu_B^2}\frac{\pi\alpha^2}{m_e^2}\left[\frac{1}{E_R} - \frac{1}{E_\nu}\right], \tag{3.3.2}$$

where

$$|\mu_i^{\text{eff}}|^2 \equiv \sum_j |\mu_{ji}|^2, \tag{3.3.3}$$

is the magnitude squared of the effective magnetic moment associated to an incoming ν_i. The effective magnetic moments μ_i^{eff} are directly constrained by solar neutrino experiments since these are best described as incoherent mixtures of the neutrinos with well defined masses, ν_1, ν_2, ν_3, etc.

Neutrinos that are both produced and detected on Earth are best described as coherent linear superpositions of the neutrino mass eigenstates – the neutrino flavor eigenstates, $\nu_\alpha = U_{\alpha i}\nu_i$, $\alpha = e, \mu, \tau$, where $U_{\alpha i}$ are the elements of the unitary lepton mixing matrix. It is simple to define the neutrino electromagnetic moment matrix in the flavor-eigenstate basis. If the neutrinos are Majorana fermions,

$$\mathcal{L}_{\text{M}} = \frac{1}{2}\mu_{ij}U^*_{\alpha i}\nu_\alpha\sigma_{\mu\nu}U^*_{\beta j}\nu_\beta F^{\mu\nu} + H.c. = \frac{1}{2}\mu_{\alpha\beta}\nu_\alpha\sigma_{\mu\nu}\nu_\beta F^{\mu\nu} + H.c., \tag{3.3.4}$$

where

$$\mu_{\alpha\beta} \equiv U^*_{\alpha i}U^*_{\beta j}\mu_{ij}. \tag{3.3.5}$$

Instead, if the neutrinos are Dirac fermions,

$$\mathcal{L}_{\text{D}} = \mu^D_{ij}V^*_{\alpha i}\nu^c_\alpha\sigma_{\mu\nu}U^*_{\beta j}\nu_\beta F^{\mu\nu} + H.c. = \mu^D_{\alpha\beta}\nu^c_\alpha\sigma_{\mu\nu}\nu_\beta F^{\mu\nu} + H.c. \tag{3.3.6}$$

where we introduce a matrix V that relates the left-handed antineutrinos in the mass eigenstate basis to those in the flavor-eigenstate basis. Since there are no weak interactions

for the left-handed antineutrinos, their flavor-eigenstate basis is undetermined and $V_{\alpha i}$ are not physical. We can take advantage of this and choose $V_{\alpha i} = U_{\alpha i}$ so, for Dirac neutrinos, the electromagnetic dipole moment matrix in the flavor-eigenstate basis is also given by Eq. (3.3.5), with the addition of the superscript D (for Dirac).

Similar to σ_{ij}, the neutrino dipole contribution to the $\nu_\alpha + e \to \nu_\beta + e$ cross section $\sigma_{\alpha\beta}$ is proportional to $|\mu_{\beta\alpha}|^2$. Summing over the flavors of the final-state netrinos,

$$\frac{d\sigma_\alpha}{dE_R} = \frac{|\mu_\alpha^{\text{eff}}|^2}{\mu_B^2}\frac{\pi\alpha^2}{m_e^2}\left[\frac{1}{E_R} - \frac{1}{E_\nu}\right], \tag{3.3.7}$$

where

$$|\mu_\alpha^{\text{eff}}|^2 \equiv \sum_\beta |\mu_{\beta\alpha}|^2. \tag{3.3.8}$$

Note that one is not obliged to work in the flavor-eigenstate basis even when the incoming state is a flavor eigenstate. In the mass-eigenstate basis, the incoming neutrino is a linear superposition of mass eigenstates so the amplitude for $\nu_\alpha \to \nu_i$ is $\mathcal{A}_{\alpha i} \propto U_{\alpha j}\mu_{ij}$. Summing over all possible final-states (assuming again these are impossible to measure or "tag" in either flavor or mass eigenstates) $\sigma_\alpha \propto \sum_i |U_{\alpha j}\mu_{ij}|^2$. It is easy to show that $\sum_i |U_{\alpha j}\mu_{ij}|^2 = \sum_\beta |\mu_{\beta\alpha}|^2 = |\mu_\alpha^{\text{eff}}|^2$.

There remains the possibility of producing a neutrino flavor-eigenstate ν_α and detecting it via elastic scattering some distance L away from the neutrino source. In this case, the incoming neutrino state is the "oscillated ν_α," a different linear superposition of mass-eigenstates (see, for example, [**77**]). Given what is known about the neutrino mass-squared

differences, oscillation effects are irrelevant to all Earth-bound experimental constraints of interest.

3.4. Summary of Experimental Constraints

As discussed earlier, we will concentrate on bounds that come from the scattering of solar neutrinos or Earth-bound (anti)neutrinos.[†] In the case of Earth-bound neutrinos, different sources have been used in order to search for a nonzero neutrino electromagnetic moment, including neutrinos from nuclear reactors and neutrinos from pion decay. In both cases, the strongest bounds are obtained from precise analyses of neutrino–electron scattering so we will concentrate on those. In the case of neutrinos from pion decay at rest, coherent elastic neutrino–nucleus scattering (CEvNS) data has also been used to search for nonzero neutrino dipole moments. Current estimates, obtained from data made available by the COHERENT Collaboration [**92**], are not yet competitive (for recent analyses see [**84, 85**]). From the CEvNS measurement in CsI, constraints down to few $\times 10^{-9}$ μ_B can be obtained with 90% C.L, while the future detector materials of the COHERENT experiment, e.g. Ge, can generally perform better by a factor of a few [**68, 70, 69**].

There are also interesting results from the DONUT experiment, which obtains an upper bound of $|\mu_{\nu_\tau}^{\rm eff}| < 3.9 \times 10^{-7}$ μ_B with 90% C.L. [**93**]. It makes use of neutrinos from meson decays in flight, including a nonzero sample of ν_τ-initiated scattering events. We will comment on these bounds in Sec. 3.6.

One can also obtain constraints down to $|\mu_\nu| \sim$ few $\times\ 10^{-12}$ μ_B from stellar cooling [**74**]. These constraints are less robust and somewhat model dependent (for an earlier detailed discussion, see, for example, [**73**]). It has also been argued that new physics can

[†]We will, in general, use 'neutrinos' to refer to neutrinos or antineutrinos.

weaken such bounds significantly. For example, in so-called "chameleon" models [**94**], these bounds are virtually absent. The observation of neutrinos from Supernova 1987A can also be used to constrain the neutrino magnetic moment. Early estimates pointed to $|\mu_\nu| \sim$ few $\times\, 10^{-13}\ \mu_B$ [**75, 76**]. More recently, however, these bounds were called into question [**95**], and it was argued that they may not be valid at all. Henceforth, we do not consider indirect astrophysical bounds in our analyses.

Finally, unless otherwise noted, we assume henceforth there are only three light neutrino states.

3.4.1. Solar Experiments

Neutrinos from the Sun arrive at the Earth as incoherent mixtures of the mass eigenstates: ν_1 with probability P_1, ν_2 with probability P_2, ν_3 with probability P_3 (for a recent, detailed overview, see, for example, [**96**]). Given what is currently known about neutrino-oscillation parameters[‡], for all solar neutrino energies, $P_3 = |U_{e3}|^2 \sim 0.02$, while P_1 and P_2 depend on the neutrino energy. Here we ignore the impact of the nonzero neutrino magnetic moments on the flavor evolution of the neutrinos inside the Sun.

The measurement of solar neutrinos scattering on electrons, for a fixed neutrino energy, is sensitive to

$$|\mu|^2_{\rm solar} = P_1|\mu_1^{\rm eff}|^2 + P_2|\mu_2^{\rm eff}|^2 + P_3|\mu_3^{\rm eff}|^2. \tag{3.4.1}$$

The best published solar neutrino constraints are from the Borexino experiment. Using solar neutrino data taken in 1291.5 days during its second phase, Borexino set an

[‡]In our analyses, we use the results presented in [**28**], NuFIT5.1 (2021). See also `http://www.nu-fit.org`. Concretely, we use $\sin^2\theta_{12} = 0.304$, $\sin^2\theta_{13} = 0.02220$, $\sin^2\theta_{23} = 0.573$.

upper bound of $|\mu|_{\rm solar} < 2.8 \times 10^{-11}\ \mu_B$ at 90% C.L. for predominantly ^{7}Be neutrinos (monochromatic, $E_\nu = 862$ keV). For ^{7}Be neutrino energies, matter effects inside the Sun are small and $P_1 = |U_{e1}|^2 \sim 0.7$ and $P_2 = |U_{e2}|^2 \sim 0.3$ to a good approximation.

The XENON experiments, while searching for dark matter, are also sensitive to neutrinos from the Sun. When it comes to nonzero magnetic moments, the dominant contribution is from *pp* solar neutrinos (most abundant, lowest energy). For *pp*-solar neutrinos, matter effects inside the Sun are negligible and $P_1 = |U_{e1}|^2 \sim 0.7$ and $P_2 = |U_{e2}|^2 \sim 0.3$ is an excellent approximation. The excess of electron recoil events reported by the XENON1T collaboration [**2**] can be explained by a nonzero neutrino electromagnetic moment ($\mu_\nu = 5.7 \times 10^{-11}$ is the quoted best-fit value [**97**]). However, the observed excess can also be interpreted as evidence for some unaccounted-for background, e.g., tritium decays [**2**]. Given all the uncertainty, we do not include the XENON1T results in our analysis. Furthermore, very recently, first results on the low-energy electron-recoil data of the XENONnT collaboration were made public [**29**]. The XENONnT collaboration reports an upper bound of $|\mu|_{\rm solar} < 6.3 \times 10^{-12}\ \mu_B$ (90% C.L.) that is almost five times stronger than the Borexino upper bound. This bound supersedes the XENON1T hint by almost an order of magnitude and is included in our analysis.

Future dark matter direct-detection experiments will also be sensitive to the *pp* solar neutrinos. These should be sensitive to effective magnetic moments of order $10^{-12}\mu_B$ [**72**], almost an order of magnitude smaller than the recently reported XENONnT bound.

There are also constraints from the scattering of ^{8}B neutrinos on electrons [**98**]. ^{8}B neutrinos have energies between 5 MeV and 10 MeV and are strongly impacted by solar matter effects. For ^{8}B neutrinos, $P_1 \sim 0.1$ and $P_2 \sim 0.9$, with some energy dependency.

Dipole moment constraints from ^{8}B neutrinos are not competitive with those from Borexino or XENONnT and will not be included in our results.

3.4.2. Reactor Experiments

Nuclear reactors are intense sources of electron antineutrinos. The GEMMA experiment [**66**] sets the strongest bound on the neutrino electromagnetic moment among the reactor neutrino experiments. Using a total of 22,621 hours of data taking, they set the upper bound $\mu^{\rm eff}_{\bar{e}} < 2.9 \times 10^{-11}\ \mu_B$ at 90% C.L. (the bar indicates an incoming $\bar{\nu}_e$). The TEXONO collaboration also measured elastic neutrino–electron scattering for electron antineutrinos coming from the Kuo-Sheng Nuclear reactor [**99**] and constrained $\mu^{\rm eff}_{\bar{e}} < 2.2 \times 10^{-10}\ \mu_B$ at 90% C.L.. This is an order of magnitude weaker than the GEMMA bound and hence we ignore it here. More recently, the CONUS collaboration, using candidate neutrino–electron scattering events, also reported a bound on the the effective electron antineutrino magnetic moment, $\mu^{\rm eff}_{\bar{e}} < 7.5 \times 10^{-11}\ \mu_B$ at 90% C.L. [**100**]. Since it is two and half times weaker than the published GEMMA bounds, we do not include the CONUS constraints in our analyses.

3.4.3. Accelerator Experiments

The LSND experiment measured neutrino–electron scattering using neutrinos produced in π^+ and μ^+ decay at rest [**101**]. Pion decay produces mostly ν_μ while muon decay produces both ν_e and $\bar{\nu}_\mu$. LSND data are analyzed and the collaboration reports a constraint on a mixture of $|\mu^{\rm eff}_e|^2$ and $|\mu^{\rm eff}_\mu|^2$: $|\mu^{\rm eff}_e|^2 + 2.4|\mu^{\rm eff}_\mu|^2 < 1.1 \times 10^{-18}\ \mu_B^2$ at 90% C.L. [**101**]. They assume $|\mu^{\rm eff}_\mu|^2 = |\mu^{\rm eff}_{\bar{\mu}}|^2$.

In the future, the DUNE experiment is expected to be sensitive to $|\mu_\mu^{\text{eff}}| > 3.2 \times 10^{-10}\ \mu_B$ at 90% C.L. after seven years data taking in both the neutrino and antineutrino modes [**71**]. Because of the GeV energy range of DUNE and the dependence of the electromagnetic cross section on the inverse of the neutrino energy, DUNE is not the best place to get competitive constraints on μ_μ^{eff}, despite its unprecedented neutrino flux and large detector mass. The J-PARC Sterile Neutrino Search at J-PARC Spallation Neutron Source (JSNS^2) experiment [**102**], including its proposed upgrade [**103**], might ultimately have better sensitivity since it makes use of neutrinos from meson and muon decay at rest, similar to LSND. Finally, as already discussed, future measurements of CEvNS and neutrino–electron scattering using neutrinos from pion decay at rest may ultimately provide better sensitivity to $|\mu_\mu^{\text{eff}}|$.

To illustrate the impact a measurement of $|\mu_\mu^{\text{eff}}|$ could have on the experimental landscape, in Sec. 3.6 we will assume that results from a future experiment sensitive to $|\mu_\mu^{\text{eff}}| > 2 \times 10^{-11}\mu_B$ are available. This sensitivity is comparable to that of Borexino and does not compete with expectations from future solar experiments. Nonetheless, we will argue that the impact of such an experiment may be, under the right circumstances, very significant.

3.4.4. Statistical Treatment of Experimental Constraints

All experiments report upper bounds on some effective electromagnetic moment $|\mu^{\text{eff}}|_{\text{exp}}$ (in general a different effective magnetic moment for each experiment of interest). When computing upper bounds on the different $|\mu_{ij}|$, presented and discussed in Sec. 3.6, we treat these upper bounds as quadratic χ^2 functions of $|\mu_{\text{eff}}|^2$ and assume the best-fit values

associated to all experimental results are equal to zero:

$$\chi^2_{\rm exp} = \frac{(|\mu^{\rm eff}|^2)^2}{\sigma^2_{\rm exp}}, \tag{3.4.2}$$

where $\sigma_{\rm exp}$ is extracted from the reported 90% C.L. upper bounds quoted by the different collaborations, $\mu^{\rm eff}_{90\%}$:

$$\sigma_{\rm exp} = \frac{(\mu^{\rm eff}_{90\%})^2}{\Phi^{-1}_{90\%}}. \tag{3.4.3}$$

Where $\Phi^{-1}_{90\%} = 1.645$ is the quantile of the standard Gaussian corresponding to the 90% C.L.. The reason for this assumption is that the number of dipole-moment-mediated events at any experiment is linearly proportional to $|\mu^{\rm eff}|^2$ as can be seen, for example, in Eqs. (3.3.2) and (3.3.7). Note that, traditionally, one quotes upper bounds on $|\mu^{\rm eff}|$. In order to combine results from different experiments, we assume the total χ^2 to be the sum of all the relevant $\chi^2_{\rm exp}$. While this may be an oversimplification, as we are assuming the best fits to be null and neglecting correlations (e.g. in solar neutrino fluxes), we find this approach to be suitable to make our point on the interplay between magnetic moment measurements and the nature of neutrinos.

3.5. Fate of XENON1T

The XENON1T results can be interpreted as being due to a magnetic moment with magnitude $\mu_\nu \in (1.4, 2.9) \times 10^{-11}\ \mu_B$ (90% C.L.) [**2**]. Statistically, we treat this range as a Gaussian measurement and build a test statistic by modifying Eq. (3.4.2) with a non-zero central value $\mu^{\rm eff}_{\rm exp} \simeq 2.3 \times 10^{-11}\ \mu_B$ and $\sigma_{\rm exp}$ extracted from the reported 90%

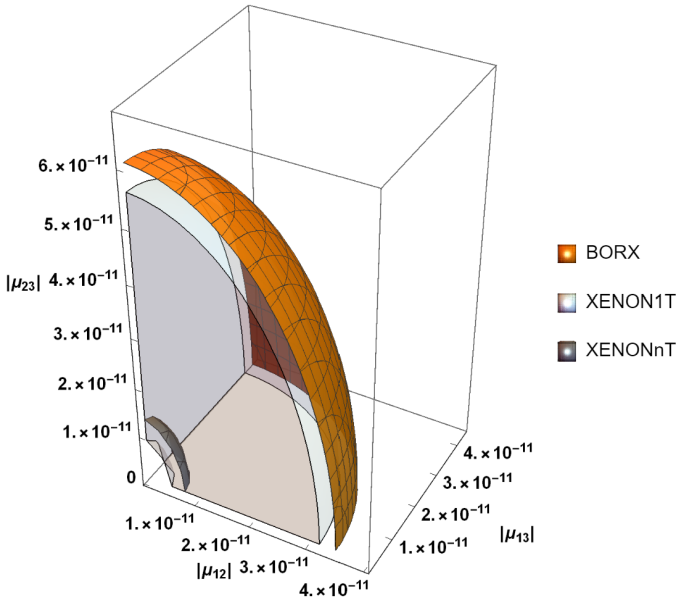

Figure 3.1. 90% allowed regions for solar experiments for Majorana neutrinos extracted from current data. We show the allowed region contours (meshed) for Borexino and XENONnT. The XENON1T measurement allowed region is shown as a filled shape.

C.L. values. The Gaussian approximation is not perfect, but it is good enough to show that the XENONnT measurement all but excludes the XENON1T hint.

First, we take a look at the case where we interpret the XENON1T excess as being due to Majorana BSM neutrino magnetic moments. Using Eq. (3.6.1), we can view the the 90% C.L. preferred regions of the Borexino (orange), XENON1T (filled light cyan), and XENONnT (gray) results in Fig. 3.1. The XENON1T measurement region is comfortably inside the parameter space allowed by the Borexino contour. We can also see that the XENONnT measurement is sensitive enough to almost exclude the entire XENON1T preferred region. This would not be as trivial to see in a two-parameter plane, for if the

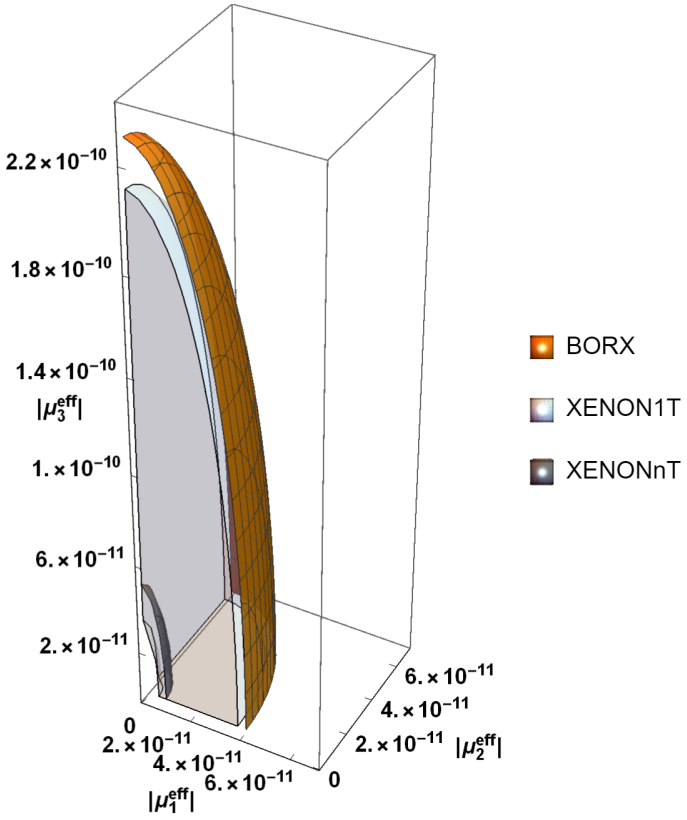

Figure 3.2. 90% allowed regions for solar experiments for Dirac neutrinos extracted from current data. We show the allowed region contours (meshed) for Borexino and XENONnT. The XENON1T measurement allowed region is shown as a filled shape. See Section 3.6.2 for more details on μ_1^{eff}, μ_2^{eff}, and μ_3^{eff}.

third magnitude of the moment is marginalized over, the entire 'shape' would collapse to show everything below the upper contour of the XENON1T preferred region as allowed.

Secondly, we interpret the results assuming Dirac neutrinos. For this we will use Eq. (3.6.3). As will be discussed in Sec. 3.6, in the solar case, we can completely describe the parameter space with three effective fundamental magnetic moments. Fig. 3.2 shows the 90% C.L. preferred regions for the Dirac case for the Borexino (organge), XENON1T (light cyan), and XENONnT (gray) results. The Dirac case depends on 9 magnitudes,

but as will be discussed later on, we can completely describe the parameter space with the three fundamental effective solar moments μ_1^{eff}, μ_2^{eff}, and μ_3^{eff}. Again, it is clear that the XENONnT results exclude the XENON1T region. Nevertheless, we can appreciate how the sensitivity to the moments associated with U_{e3} weakens drastically. Furthermore, we can appreciate that the XENON1T measurement, or more generally any solar measurement, does not individually aid our ability to distinguish between Majorana or Dirac neutrinos. Taking this into account, we will look at other neutrino sources and experiments to better understand the discovery potential when looked through the Majorana or Dirac lens.

3.6. Results: Present and Future

Here we present and discuss the current constraints on all $|\mu_{ij}|$ for both Majorana and Dirac neutrinos. We present all results in the neutrino mass-eigenstate basis; when convenient, we make use of the flavor-eigenstate basis in order to discuss specific results. Our ultimate goal is to combine all constraints from the different neutrino sources and experiments and discuss the impact of future experimental efforts. We comment on individual constraints when it is illuminating. Comparisons between Dirac neutrinos and Majorana neutrinos are presented in the 'Dirac Neutrinos' subsection.

All upper bounds and exclusion curves are quoted at 90% C.L., for the relevant number of degrees of freedom.

3.6.1. Majorana Neutrinos

If neutrinos are Majorana fermions, assuming there are no new light fermions, there are three independent complex neutrino electromagnetic dipole moments: $\mu_{12}, \mu_{13}, \mu_{23}$. We will concentrate on the existing constraints on $|\mu_{12}|, |\mu_{13}|, |\mu_{23}|$, keeping in mind the complex phases in $\mu_{12}, \mu_{13}, \mu_{23}$ are unconstrained. Unless otherwise noted, when presenting constraints on $|\mu_{12}|, |\mu_{13}|, |\mu_{23}|$, we marginalize over all unreported parameters.

As discussed in Sec. 3.3, to a good approximation, the solar neutrino experiments of interest are sensitive to

$$|\mu|^2_{\rm solar} = |U_{e1}|^2 \left(|\mu_{12}|^2 + |\mu_{13}|^2\right) + |U_{e2}|^2 \left(|\mu_{12}|^2 + |\mu_{23}|^2\right) + |U_{e3}|^2 \left(|\mu_{13}|^2 + |\mu_{23}|^2\right), \tag{3.6.1}$$

and hence insensitive to the relative phases among the different dipole moments. Constraints from Borexino and XENONnT in the different $|\mu_{ij}| \times |\mu_{jk}|$ planes $(i, j, k = 1, 2, 3)$ are depicted in Fig. 3.3 (orange and grey lines, respectively). Since all terms in Eq. (3.6.1) are positive-definite, it is possible to marginalize over all-but-one of the elements of the electromagnetic dipole matrix and constrain each $|\mu_{ij}|$ independently. The 90% C.L. upper bounds we obtain from the Borexino and XENONnT bounds are listed in Table 3.1. Throughout, we kept the neutrino oscillation parameters fixed at their best-fit values, except for the CP-odd parameter $\delta_{\rm CP}$, which we allow to float in the fits. Note that the CP-odd phase is irrelevant for the solar neutrino constraints. Had we allowed the mixing angles to also float in the fits, we would have obtained slightly weaker bounds (roughly five to ten percent), given the current uncertainties on the relevant mixing parameters.

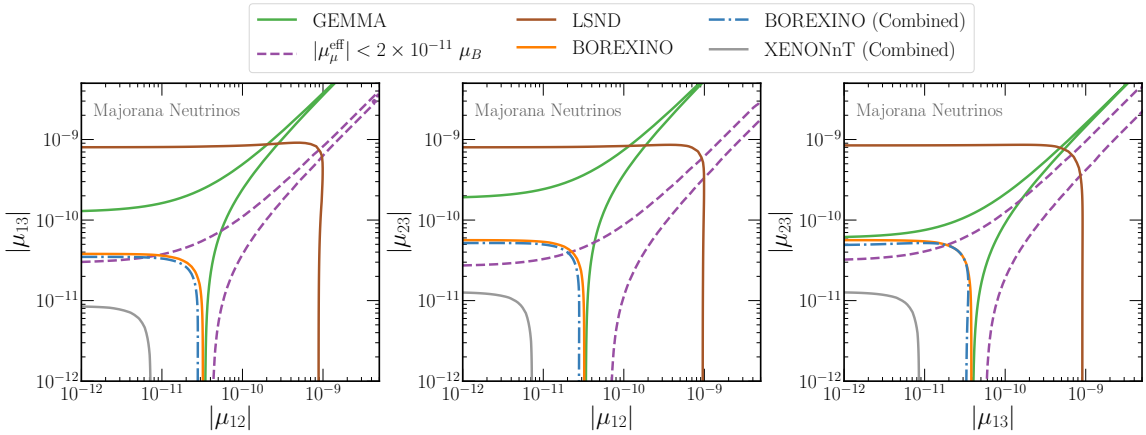

Figure 3.3. Majorana neutrinos. 90% C.L. allowed regions in the $|\mu_{12}| \times |\mu_{13}|$-plane (left), $|\mu_{12}| \times |\mu_{23}|$-plane (center), $|\mu_{13}| \times |\mu_{23}|$-plane (right), extracted from different subsets of existing and hypothetical future data. 'BOREXINO (Combined)' stands for data from Borexino, GEMMA, and LSND. 'XENONnT (Combined)' stands for data from XENONnT, Borexino, GEMMA, and LSND. '$|\mu_\mu^{\rm eff}| < 2\times10^{-11}\ \mu_B$' stands for data from a future experiment that constraints $|\mu_\mu^{\rm eff}| < 2\times10^{-11}\ \mu_B$. See Section 3.4 for details.

Table 3.1 reveals that the constraints from solar data on $|\mu_{12}|, |\mu_{13}|, |\mu_{23}|$ are relatively similar, within less than a factor of two (a factor a little over three for $|\mu_{ij}|^2$). The reason is that, for Majorana neutrinos, $\mu_{ij} = -\mu_{ji}$. Even though $|U_{e3}|^2 \ll |U_{e1}^2|, |U_{e2}|^2$, the coefficients behind the different $|\mu_{ij}|^2$ are relatively similar, ranging from $|U_{e2}|^2 + |U_{e3}|^2 \sim 0.3$ to $|U_{e1}|^2 + |U_{e2}|^2 \sim 1$.

The situation is different for experiments that constrain $|\mu_\alpha^{\rm eff}|^2$, $\alpha = e, \mu, \tau$, including reactor experiments. Constraints from GEMMA on $|\mu_{\bar{e}}^{\rm eff}|^2$ translate into the green contours in Fig. 3.3 while the sensitivity of a hypothetical future experiment that can see a nonzero $|\mu_\mu^{\rm eff}|^2$ if it is larger than $2\times10^{-11}\mu_B$ is depicted in purple (dashed line). In both these cases, there is a clear "flat direction" in the different $|\mu_{ij}| \times |\mu_{jk}|$-planes

Table 3.1. 90% C.L. upper bounds on the magnitudes of the different entries of the neutrino electromagnetic moment matrix, for Majorana neutrinos, extracted from different subsets of existing and hypothetical future data. 'Future ν_μ' stands for a future experiment capable of constraining $|\mu_\mu^{\rm eff}| < 2 \times 10^{-11}\ \mu_B$. See Section 3.4 for details.

Experiment	$\lvert\mu_{12}\rvert$ $(10^{-11}\mu_B)$	$\lvert\mu_{13}\rvert$ $(10^{-11}\mu_B)$	$\lvert\mu_{23}\rvert$ $(10^{-11}\mu_B)$
LSND	90	84	79
Borexino	2.8	3.3	5.0
Borexino & LSND & GEMMA	2.4	3.0	4.4
XENONnT	0.64	0.75	1.1
All Combined	0.64	0.75	1.1
All Combined & Future ν_μ	0.64	0.75	1.1

[**104, 69**]. This implies, for example, one cannot obtain bounds on any of the $|\mu_{ij}|$ that is independent from the other parameters that define the dipole moment matrix.

The reason for the flat direction is easy to understand. In the flavor-eigenstate basis,

$$|\mu_e^{\rm eff}|^2 = |\mu_{e\mu}|^2 + |\mu_{e\tau}|^2. \tag{3.6.2}$$

It is easy to see that $|\mu_e^{\rm eff}|^2$ depends only on the magnitudes of two out of the three $\mu_{\alpha\beta}$ $(\alpha, \beta = e, \mu, \tau)$; it does not depend on $\mu_{\mu\tau}$ at all. Since the three $\mu_{\alpha\beta}$ (and μ_{ij}) are, in general, independent, there is a combination of $|\mu_{ij}|$ – indeed, $\mu_{\mu\tau}$ – that remains unconstrained. This translates into the cuspy contours observed in Fig. 3.3. The same argument holds for $|\mu_\mu^{\rm eff}|^2$, $|\mu_\tau^{\rm eff}|^2$.

Flat directions are lifted if one combines constraints on different $|\mu_\alpha^{\rm eff}|^2$. Bounds from the LSND experiments, depicted in brown in Fig. 3.3, illustrate this, since, as discussed in Section 3.4, LSND constrains a weighted sum of $|\mu_\mu^{\rm eff}|^2$ and $|\mu_e^{\rm eff}|^2$. For this reason, we can compute the LSND bounds on the different $|\mu_{ij}|$ after one marginalizes over all other

dipole moment observables. These are listed in Table 3.1. The LSND bounds are much weaker than the solar bounds.

Combinations of solar data with reactor or accelerator data are also free from flat directions and one can obtain constraints on all μ_{ij}, marginalizing over all other dipole moment observables, from all current experiments combined. These are listed in Table 3.1 and depicted in Fig. 3.3 (dot-dashed blue contour for Borexino combined with LSND and GEMMA, grey for XENONnT combined with all other existing data). The bounds from solar experiments dominate those from Earth-bound experiments. The XENONnT constraints are strong enough that the impact of combining them with all other data is negligible. We also combine all existing constraints with a future experiment that excludes, at the 90% C.L., $|\mu_\mu^{\rm eff}| < 2 \times 10^{-11} \mu_B$. These are listed in Table 3.1. The impact of the future experiment is negligible relative to that of XENONnT.

More generally, if the neutrinos are Majorana fermions and there are no extra neutrino degrees of freedom, expectations are that next-generation experiment sensitive to $|\mu_\mu^{\rm eff}|^2 > 2 \times 10^{-11} \mu_B$ will not see the effects of nonzero neutrino electromagnetic moments. The solar bounds preclude it. This is depicted in Fig. 3.3. The sensitivity region of the future $|\mu_\mu^{\rm eff}|^2$ is well inside the region of parameters space ruled out by the XENONnT experiment.

3.6.2. Dirac Neutrinos

If neutrinos are Dirac fermions, assuming there are no new light fermions, there are nine independent complex neutrino electromagnetic dipole moments: μ_{11}^D, μ_{12}^D, μ_{13}^D, μ_{21}^D, μ_{22}^D, μ_{23}^D, μ_{31}^D, μ_{32}^D, μ_{33}^D. Like in the Majorana neutrino case, we will concentrate on the

existing constraints on the magnitudes of the different electromagnetic moments $|\mu_{ij}^D|$ $(i,j=1,2,3)$, keeping in mind the complex phases of the different μ_{ij}^D are unconstrained. Unless otherwise noted, when presenting constraints, we marginalize over all unreported parameters.

As discussed in Sec. 3.3, to a good approximation, the solar neutrino experiments of interest are sensitive to

$$
\begin{aligned}
(3.6.3)\ |\mu|^2_{\rm solar} &= |U_{e1}|^2|\mu_1^{\rm eff}|^2 + |U_{e2}|^2|\mu_2^{\rm eff}|^2 + |U_{e3}|^2|\mu_3^{\rm eff}|^2, \\
&= |U_{e1}|^2\left(|\mu_{11}^D|^2 + |\mu_{21}^D|^2 + |\mu_{31}^D|^2\right) + |U_{e2}|^2\left(|\mu_{12}^D|^2 + |\mu_{22}^D|^2 + |\mu_{32}^D|^2\right) + \\
(3.6.4) &\quad + |U_{e3}|^2\left(|\mu_{13}^D|^2 + |\mu_{33}^D|^2 + |\mu_{33}^D|^2\right),
\end{aligned}
$$

and hence insensitive to the relative phases among the different dipole moments. While all nine $|\mu_{ij}^D|$ are constrained by solar data, it is clear that the bounds are correlated. After marginalizing over all other $|\mu_{ij}^D|$, the bounds on, for example, $|\mu_{11}^D|$ and $|\mu_{21}^D|$ are identical. Hence, as far as solar data are concerned, it is sufficient to extract bounds on $|\mu_i^{\rm eff}|$, $i=1,2,3$, defined in Eq. (3.3.3); these apply to all $|\mu_{ij}^D|$ (for fixed i, $j=1,2,3$). 90% C.L. Constraints from Borexino and XENONnT in the different $|\mu_i^{\rm eff}| \times |\mu_j^{\rm eff}|$ planes $(i,j=1,2,3)$ are depicted in Fig. 3.4 in orange and grey, respectively. Since all terms in Eq. (3.6.3) are positive-definite, it is possible to marginalize over all-but-one of the effective electromagnetic dipole moments and constrain each $|\mu_i^{\rm eff}|$ independently. The 90% C.L. upper bounds we obtain from the Borexino and XENONnT bounds are listed in Table 3.2. Throughout, we kept the neutrino oscillation parameters fixed at their best-fit values, except for the CP-odd parameter $\delta_{\rm CP}$, which we allow to float in the fits.

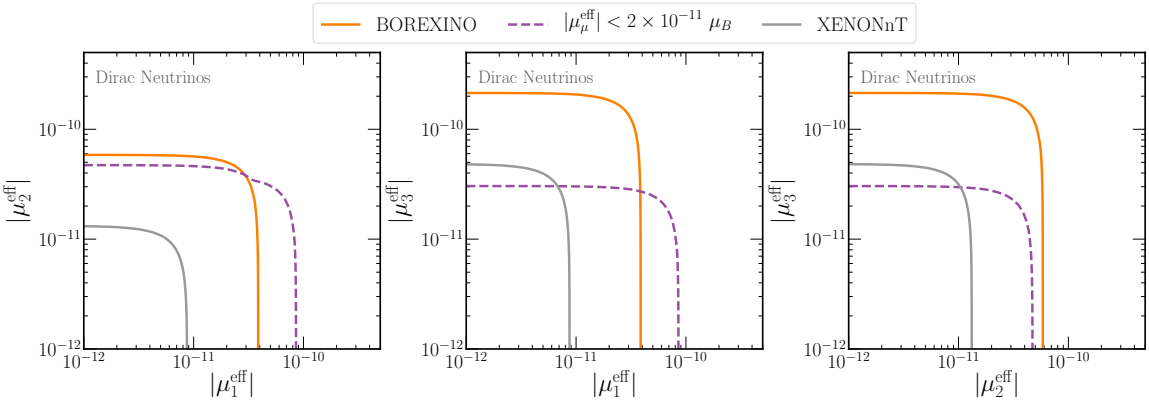

Figure 3.4. Dirac neutrinos. 90% C.L. allowed regions in the $|\mu_1^{\rm eff}| \times |\mu_2^{\rm eff}|$-plane (left), $|\mu_1^{\rm eff}| \times |\mu_3^{\rm eff}|$-plane (center), $|\mu_2^{\rm eff}| \times |\mu_3^{\rm eff}|$-plane (right), extracted from different subsets of existing and hypothetical future data. '$|\mu_\mu^{\rm eff}| < 2 \times 10^{-11}\ \mu_B$' stands for data from a future experiment that constraints $|\mu_\mu^{\rm eff}| < 2 \times 10^{-11}\ \mu_B$. See Section 3.4 for details. In the case of the future experiment sensitive to $|\mu_\mu^{\rm eff}|$ (dashed, purple curves), we assume only $\mu_{11}^D, \mu_{22}^D, \mu_{33}^D \neq 0$.

Note that the CP-odd phase is irrelevant for the solar neutrino constraints. Had we allowed the mixing angles to also float in the fits, we would have obtained slightly weaker bounds (roughly five to ten percent), given the current uncertainties on the relevant mixing parameters.

Table 3.2 reveals that $|\mu_3^{\rm eff}|$ is significantly less constrained – one order of magnitude – by solar data than $|\mu_{1,2}^{\rm eff}|$. The reason is that, for Dirac neutrinos, the different $|\mu_i^{\rm eff}|$ are independent and $|U_{e3}|^2 \ll |U_{e1}|^2, |U_{e2}|^2$. This is to be contrasted to the Majorana case, where all independent $|\mu_{ij}|$ are similarly constrained by solar data. In the Dirac case, if $|U_{e3}|^2$ were zero, the bound on $|\mu_3^{\rm eff}|$ would disappear. In the Majorana case, the solar bounds presented in Table 3.1 would be almost identical to what one would have obtained if $|U_{e3}|^2$ were zero.

Table 3.2. 90% C.L. upper bounds on the magnitudes of the different entries of the neutrino electromagnetic moment matrix, for Dirac neutrinos, extracted from different subsets of existing and hypothetical future data. 'Future ν_μ' stands for a future experiment capable of constraining $|\mu_\mu^{\text{eff}}| < 2 \times 10^{-11}\ \mu_B$. See Section 3.4 for details.

	$\lvert\mu_{ij}^D\rvert$ $(10^{-11}\mu_B)$		
Experiment	$ij = 11, 21, 31$	$ij = 12, 22, 32$	$ij = 13, 23, 33$
Borexino	3.4	5.1	19
Borexino & GEMMA & LSND	3.2	4.8	18
XENONnT	0.76	1.2	4.2
All Combined	0.76	1.2	4.2
All Combined & Future ν_μ	0.76	1.2	2.8

Experimental results that translate into an upper bound on a single $|\mu_\alpha^{\text{eff}}|$, $\alpha = e, \mu, \tau$, do not translate into bounds on individual μ_{ij}^D, similar to the Majorana case. Also here, there are flat directions, i.e., linear combinations of $|\mu_{ij}^D|^2$ that are unconstrained. In fact, in the Dirac case, there are many more flat directions relative to the Majorana case. This is simplest to see in the flavor-eigenstate basis. For example,

$$|\mu_e^{\text{eff}}|^2 = |\mu_{ee}^D|^2 + |\mu_{\mu e}^D|^2 + |\mu_{\tau e}^D|^2, \tag{3.6.5}$$

clearly independent from six of the nine $|\mu_{\alpha\beta}^D|$, $\alpha, \beta = e, \mu, \tau$.

Unlike the Majorana case, constraints from LSND are also plagued by flat directions in the Dirac case. Using the flavor-eigenstate basis, the effective dipole moment constrained by LSND is independent from $|\mu_{e\tau}|^2, |\mu_{\mu\tau}|^2, |\mu_{\tau\tau}|^2$. In the case of Dirac neutrinos, a collection of Earth-bound experiments capable of fully constraining all independent $|\mu_{ij}^D|$

should also include a ν_τ-initiated scattering sample.* For example, data from GEMMA, LSND, *and* DONUT can constrain all μ_{ij}^D, independent from exact flat directions.

Combinations of solar data with those from Earth-bound experiments are not, of course, plagued by flat directions. Furthermore, Earth-bound experiments provide information on the $|\mu_{ij}^D|$ beyond $|\mu_i^{\rm eff}|^2$. We return to these momentarily but, for now, it is enough to state that all such combinations still translate into identical bounds on the elements of the "triplets" $(|\mu_{11}^D|, |\mu_{21}^D|, |\mu_{31}^D|)$, $(|\mu_{12}^D|,\ |\mu_{22}^D|, |\mu_{32}^D|)$, or $(|\mu_{13}^D|, |\mu_{23}^D|, |\mu_{33}^D|)$. In practice, given that constraints from Borexino and, especially, XENONnT are stronger than those from nuclear reactor and accelerator neutrinos, the consequences of adding, to the solar data, the Earth-bound data, are quantitatively quite small. Combined results are listed in Table 3.2. As in the Majorana case, the XENONnT constraints are strong enough that the impact of combining them with all other data is negligible.

Future data could, in principle, lead to a less trivial picture and more information. Constraints from an experiment that rules out, at the 90% C.L., $|\mu_\mu^{\rm eff}|^2 > 2 \times 10^{-11}\mu_B$, combined with current XENONnT data, are also listed in Table 3.2. While the impact on the $|\mu_{i1}|$ and $|\mu_{i2}|$ $(i = 1, 2, 3)$ elements is negligible, the impact on the $|\mu_{i3}|$ elements is quite significant. This is due to the fact that $|U_{e3}| \ll |U_{\mu 3}|$. More important than placing more stringent bounds, if the neutrinos are Dirac fermions, a future experiment more sensitive to $|\mu_\mu^{\rm eff}|^2$ than LSND may potentially observe the effect of a nonzero neutrino electromagnetic even if there are no extra neutrino states. Fig. 3.4 depicts the sensitivity of a hypothetical future experiment that can see a nonzero $|\mu_\mu^{\rm eff}|^2$ if it is larger than

*Another option is an "oscillated" scattering sample, i.e, a well-defined flavor eigenstate detected via the electromagnetic dipole-moment interaction a long distance L away.

$2 \times 10^{-11}\mu_B$ in purple (dashed), assuming only the diagonal μ^D_{ij} are nonzero.[†] The figure reveals that the sensitivity of such an experiment reaches beyond current constraints on $|\mu^{\rm eff}_3|$. This is qualitatively different from what was observed in the Majorana case, Fig. 3.3. There, an experiment sensitive to $|\mu^{\rm eff}_\mu|^2 > 2 \times 10^{-11}\mu_B$ is unable to make a discovery unless there are light fermionic states other than the known neutrinos.

We now turn to the details of the experimental sensitivity of scattering experiments to $|\mu^D_{ij}|$. In the mass-eigenstate basis, reorganizing the terms in the summations, indicated here explicitly,

$$|\mu^{\rm eff}_\alpha|^2 = \sum_{j,k}\left(\sum_i U_{\alpha j}U^*_{\alpha k}\mu^D_{ij}\mu^{D*}_{ik}\right) \equiv \sum_{j,k} A^\alpha_{jk}S_{jk}. \tag{3.6.6}$$

Here, $A^\alpha_{jk} \equiv U_{\alpha j}U^*_{\alpha k}$ depend only on the elements of the mixing matrix,[‡] independent from the values of the electromagnetic moments. Instead, $S_{jk} \equiv \sum_i \mu^D_{ij}\mu^{D*}_{ik}$ depend only on (products of) the electromagnetic dipole moments. Eq. (3.6.6) also holds for incoming neutrinos that are incoherent superpositions of the mass eigenstates, like the solar neutrinos. In theses cases, $A_{jk} = P_j\delta_{jk}$, where P_j is the probability that an incoming ν_j "hits" the target of interest.

Any combination of measurements of $|\mu^{\rm eff}_\alpha|^2$ and $|\mu^{\rm eff}_i|^2$ is capable of measuring, or constraining, at most, the different S_{jk}, not necessarily the nine individual $|\mu^D_{ij}|$. When it comes to information on the different $|\mu^D_{ij}|$, this has interesting consequences related to the fact that $S_{jk} \equiv \sum_i \mu^D_{ij}\mu^{D*}_{ik}$, for fixed j, k, is invariant under relabeling the "i" index.

[†]The flat directions, discussed earlier, are the reason for restricting here the 18-dimensional parameter space to this much smaller subspace. Otherwise, defining the sensitivity of the future ν_μ experiment would be both cumbersome and opaque.

[‡]This discussion can be trivially generalized to the "oscillated ν_α."

In other words, all permutations of the "i" indices lead to the same S_{jk} and hence the same $\mu_\alpha^{\rm eff}$ for all α.

Some consequences of this symmetry are important for discussing upper bounds on the different μ_{ij}^D. For example, if one marginalizes any collection of upper bounds (expressed, for concreteness, as a χ^2-function) relative to all but one $|\mu_{ij}^D|$ one will obtain the same reduced χ^2 for all values of i and fixed value of j. Hence, the upper bounds one obtains for $|\mu_{1j}^D|, |\mu_{2j}^D|, |\mu_{3j}^D|$ are the same for each value of j. This is trivial to see in the solar data, as discussed earlier.

Generalizing, if the same collection of bounds is marginalized over all but a specific pair $|\mu_{ij}^D|, |\mu_{i'k}^D|$, the same reduced χ^2 is expected for all pairs i, i' related by different permutations of the i, i' indices. For $i = i'$, $j = k$, for example, we recover the result mentioned above, that the bounds on $|\mu_{1j}^D|, |\mu_{2j}^D|, |\mu_{3j}^D|$ are the same for each value of j. For $i = i'$, $j \neq k$, constraints in the $|\mu_{1j}^D| \times |\mu_{1k}^D|$, $|\mu_{2j}^D| \times |\mu_{2k}^D|$, $|\mu_{3j}^D| \times |\mu_{3k}^D|$ planes are all the same. Finally, for $i \neq i'$and fixed j, k, constraints in the $|\mu_{1j}^D| \times |\mu_{2k}^D|$, $|\mu_{2j}^D| \times |\mu_{1k}^D|$, $|\mu_{1j}^D| \times |\mu_{3k}^D|$, $|\mu_{3j}^D| \times |\mu_{1k}^D|$, $|\mu_{2j}^D| \times |\mu_{3k}^D|$, $|\mu_{3j}^D| \times |\mu_{2k}^D|$ planes are all the same. When $j = k$, only half of these are independent since, for example, the $|\mu_{12}^D| \times |\mu_{32}^D|$ and $|\mu_{32}^D| \times |\mu_{12}^D|$ planes are the same.

Therefore, when it comes to depicting constraints in the planes defined by pairs of μ_{ij}^D, instead of 36 independent such constraints, all accessible information can be depicted in 9 independent planes. Explicitely, these are (the '=' signs here mean that, in all the "equal" planes the constraints are identical.)

- $|\mu^D_{ij}| \times |\mu^D_{i'j}|$, $j = 1, 2, 3$:

$$|\mu^D_{11}| \times |\mu^D_{21}| = |\mu^D_{11}| \times |\mu^D_{31}| = |\mu^D_{21}| \times |\mu^D_{31}|,$$

$$|\mu^D_{12}| \times |\mu^D_{22}| = |\mu^D_{12}| \times |\mu^D_{32}| = |\mu^D_{22}| \times |\mu^D_{32}|,$$

$$|\mu^D_{13}| \times |\mu^D_{23}| = |\mu^D_{13}| \times |\mu^D_{33}| = |\mu^D_{23}| \times |\mu^D_{33}|.$$

- $|\mu^D_{ij}| \times |\mu^D_{ik}|$, $j \neq k$. The distinguishable $\{j, k\}$ pairs are $\{1, 2\}, \{1, 3\}, \{2, 3\}$:

$$|\mu^D_{11}| \times |\mu^D_{12}| = |\mu^D_{21}| \times |\mu^D_{22}| = |\mu^D_{31}| \times |\mu^D_{32}|,$$

$$|\mu^D_{11}| \times |\mu^D_{13}| = |\mu^D_{21}| \times |\mu^D_{23}| = |\mu^D_{31}| \times |\mu^D_{33}|,$$

$$|\mu^D_{12}| \times |\mu^D_{13}| = |\mu^D_{22}| \times |\mu^D_{23}| = |\mu^D_{32}| \times |\mu^D_{33}|.$$

- $|\mu^D_{ij}| \times |\mu^D_{i'k}|$, $i \neq i'$, $j \neq k$. The distinguishable (j, k) pairs are $\{1, 2\}, \{1, 3\}, \{2, 3\}$:

$$|\mu^D_{11}| \times |\mu^D_{22}| = |\mu^D_{11}| \times |\mu^D_{32}| = |\mu^D_{21}| \times |\mu^D_{12}| = |\mu^D_{21}| \times |\mu^D_{32}| = |\mu^D_{31}| \times |\mu^D_{12}| = |\mu^D_{31}| \times |\mu^D_{22}|,$$

$$|\mu^D_{11}| \times |\mu^D_{23}| = |\mu^D_{11}| \times |\mu^D_{33}| = |\mu^D_{21}| \times |\mu^D_{13}| = |\mu^D_{21}| \times |\mu^D_{33}| = |\mu^D_{31}| \times |\mu^D_{13}| = |\mu^D_{31}| \times |\mu^D_{23}|,$$

$$|\mu^D_{12}| \times |\mu^D_{23}| = |\mu^D_{12}| \times |\mu^D_{33}| = |\mu^D_{22}| \times |\mu^D_{13}| = |\mu^D_{22}| \times |\mu^D_{33}| = |\mu^D_{32}| \times |\mu^D_{13}| = |\mu^D_{32}| \times |\mu^D_{23}|.$$

Fig. 3.5 depicts the constraints on all distinguishable (in principle) pairs of $|\mu^D_{ij}|, |\mu^D_{i'k}|$, in the corresponding $|\mu^D_{ij}| \times |\mu^D_{i'k}|$-planes. The different curves correspond to the constraints imposed by Borexino (orange contour), Borexino data combined with LSND and GEMMA (blue, dot-dashed contour), and XENONnT combined with Borexino, LSND,

and GEMMA (grey contour). The dashed, purple line, corresponds to a hypothetical future bound, obtained by combining the existing XENONnT data with a future experiment that constrains $|\mu_\mu^{\rm eff}| < 2 \times 10^{-11}\ \mu_B$ at the 90% C.L.

When it comes to existing constraints on $|\mu_{ij}^D|, |\mu_{i'k}^D|$ pairs, as expected, the constraints from solar data also overwhelm those of all Earth-bound experiments, especially once one considers the very recent results reported by XENONnT. The situation is different once one includes future constraints from an experiment sensitive to $|\mu_\mu^{\rm eff}|^2$. The impact of these, already discussed in the context of upper bounds on individual $|\mu_{ij}^D|$ around Table 3.2, can be clearly seen in Fig. 3.5, in the planes that involve the $|\mu_{i3}^D|$ elements.

In the far future, assuming experiments are restricted to measuring $|\mu_\alpha^{\rm eff}|^2$ and $|\mu_i^{\rm eff}|^2$ (and even different versions of the "oscillated" $|\mu_\alpha^{\rm eff}|^2$), data will still only depend on the μ_{ij}^D through S_{jk}. This means that there are several μ_{ij}^D "subsets" that are indistinguishable from one another and from the most general case. To explore this further, we define the complex 3-component vector $\vec{v}_j = (\mu_{1j}^D, \mu_{2j}^D, \mu_{3j}^D)$, $j = 1, 2, 3$, so $S_{jk} = \vec{v}_j \cdot \vec{v}_k^*$. All observables are proportional to the dot-products of the three different vectors $\vec{v}$ and hence do not depend on rigid rotations in the (complex) space defined by the $\vec{v}_j$. This rotational symmetry is the one we had been exploring above. Taking advantage of this invariance, we can, for example, choose the 1-direction such that $\vec{v}_1 = (\mu_{11}^{D\star}, 0, 0)$ and the 2-direction such that $\vec{v}_2 = (\mu_{12}^{D\star}, \mu_{22}^{D\star}, 0)$.[§] There is no freedom to reduced the number of components of the third vector, $\vec{v}_3 = (\mu_{13}^{D\star}, \mu_{23}^{D\star}, \mu_{33}^{D\star})$. The entire μ_{ij}^D parameter space – 9 complex parameters – can be perfectly mimicked by a reduced parameter space – 6 complex parameters – where $\mu_{21}^D, \mu_{31}^D, \mu_{32}^D$ vanish exactly. Hence, several (as many as we

[§]The $\star$ is mean to indicate that these are not entries of a generic matrix but one where some of the elements are known to vanish.

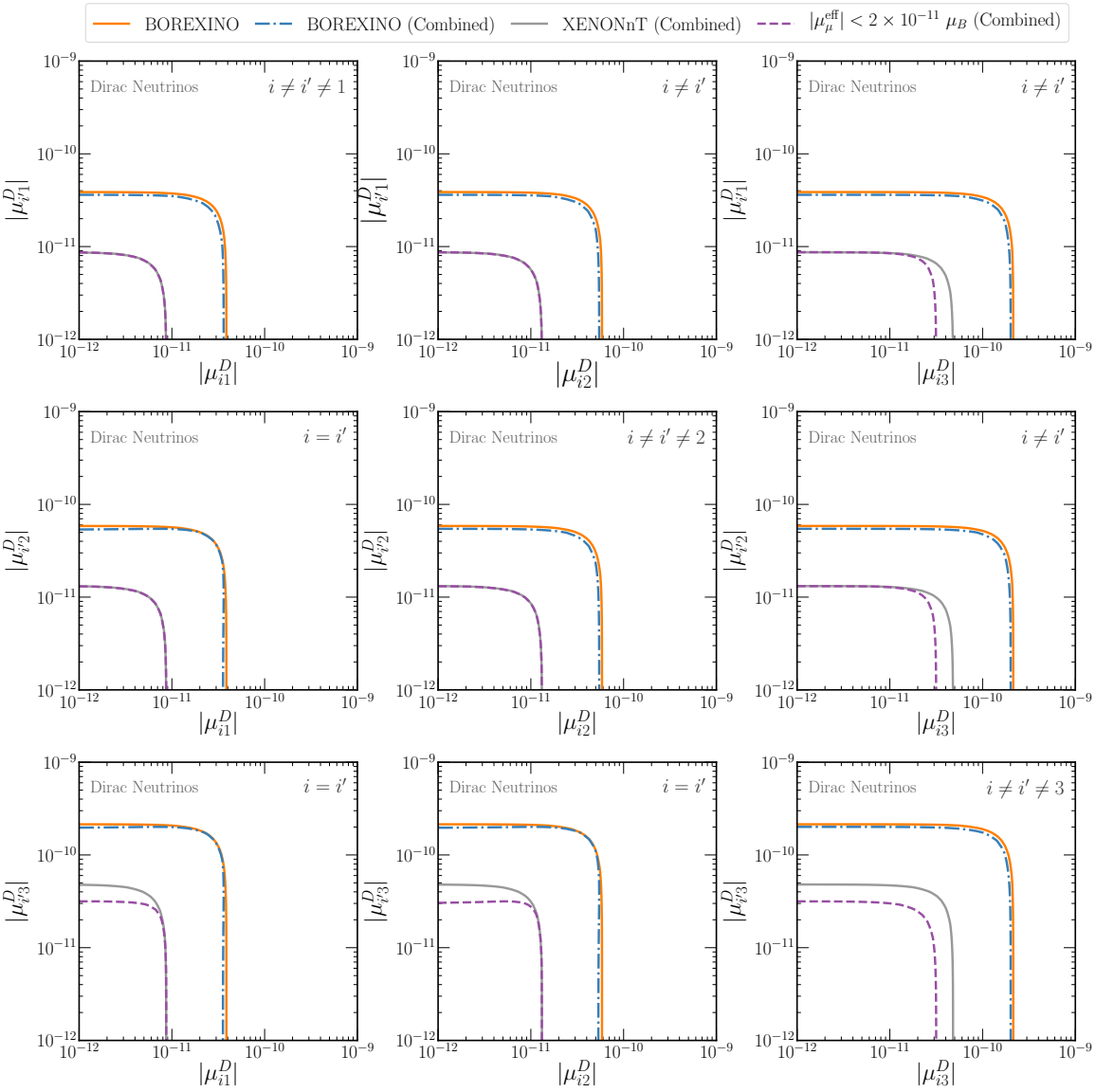

Figure 3.5. Dirac neutrinos. 90% C.L. allowed regions in all $|\mu^D_{ij}| \times |\mu^D_{i'k}|$-planes, extracted from different subsets of existing and hypothetical future data. 'BOREXINO (Combined)' stands for data from Borexino, GEMMA, and LSND. 'XENONnT (Combined)' stands for data from XENONnT, Borexino, GEMMA, and LSND. '$|\mu_\mu^{\rm eff}| < 2 \times 10^{-11}\ \mu_B$ (Combined)' stands for data from a future experiment that constraints $|\mu_\mu^{\rm eff}| < 2 \times 10^{-11}\ \mu_B$. See Section 3.4 for details. In all panels, $i, i' = 1, 2, 3$, along with the constraint in the top right-hand corner.

can imagine) idealized measurements of $|\mu_\alpha^{\rm eff}|^2$ and $|\mu_i^{\rm eff}|^2$ may well be able to establish that neutrinos have a magnetic moment, but they cannot reveal whether, for example, some of them vanish.

3.7. Conclusions

Massive neutrinos are guaranteed to have nonzero electromagnetic moments. The sizes of these dipole moments are functions of all neutrino interactions with known and unknown particles and depend on the nature of the neutrino – Majorana fermion versus Dirac fermion.

Since there are at least three neutrino families, the neutrino dipole moments define a matrix. The number of independent electromagnetic moments depends on the number of neutrino families and the nature of the neutrinos. Here, we estimated the current upper bounds on all independent neutrino electromagnetic moments, concentrating on Earth-bound experiments and measurements with solar neutrinos. We considered the hypotheses that neutrinos are Majorana fermions or Dirac fermions. Our results, obtained after marginalizing over all other dipole-moment observables (magnitudes and phases), are listed in Tables 3.1 and 3.2. We included the very recent results reported by the XENONnT experiment, sensitive to *pp*-solar neutrinos. Right now, XENONnT data provide the most stringent bounds on all elements of the neutrino electromagnetic moment matrix, independent from the nature of the neutrinos. This was already true of published solar neutrino data from the Borexino experiment, which makes use of the scattering of ^{7}Be solar neutrinos.

For the same number of neutrino families, there are more independent neutrino electromagnetic dipole moments if neutrinos are Dirac fermions. This translates into weaker bounds on the magnitudes of the elements of the dipole moment matrix relative to those obtained if neutrinos are Majorana fermions. As a concrete example, for Dirac neutrinos, if $|U_{e3}|^2$ were zero, solar data would be unable to constrain the magnitudes of three of the nine independent elements of the electromagnetic moment matrix. The situation is very different for Majorana neutrinos. In this case, the dependence on $|U_{e3}|^2$ of existing solar bounds is almost negligible.

Another consequence of the Majorana fermion versus Dirac fermion distinction is that the potential physics reach of next-generation experiments depends on the nature of the neutrino. Here, we concentrated on a next-generation experiment that is sensitive to the neutrino electromagnetic moments via ν_μ elastic scattering. An experiment sensitive to $|\mu_\mu^{\rm eff}| > 2 \times 10^{-11} \mu_B$ may discover that the neutrino electromagnetic moments are nonzero *if neutrinos are Dirac fermions*. Instead, if neutrinos are Majorana fermions, such a discovery is ruled out by existing solar neutrino data, *unless there are more than three light neutrinos*.

The Majorana fermion versus Dirac fermion distinction can be effectively erased if there are more than three light neutrinos. For example, five Majorana neutrinos (e.g., three mostly active and two mostly sterile) allow for ten complex electromagnetic dipole moments, a good match (with one dipole moment to spare) to the nine complex electromagnetic dipole moments required to describe the couplings of three Dirac neutrinos. It is not clear whether these two scenarios can be disentangled, even if one assumes a large collection of very precise future experiments, including measurements of $|\mu_{e,\mu,\tau}^{\rm eff}|^2$ from the

elastic scattering of all three flavor eigenstates along with different linear combinations of $|\mu^{\rm eff}_{1,2,3,...}|^2$ from the scattering of solar neutrinos of different energies.

We explored in great detail what information can be acquired, in principle, on the neutrino electromagnetic moments if neutrinos are Dirac fermions. Unlike the Majorana case, in the Dirac case the parameter space is very large – 9 complex parameters. Nonetheless, if all future information comes from measurements of $|\mu^{\rm eff}_{1,2,3,...}|^2$ and $|\mu^{\rm eff}_{e,\mu,\tau}|^2$, the amount of information one can extract is much more limited than naively anticipated. For example, in the absence of a discovery, for a fixed value of $j = 1, 2$, or 3, upper limits on $|\mu^D_{ij}|$ are *identical* for all $i = 1, 2, 3$. Similarly, excluded regions in several $\mu_{ij} \times \mu_{i'k}$ planes are also identical, and the argument persists for "higher-dimensional" allowed regions in $\mu_{ij} \times \ldots \times \mu_{i'k}$ spaces. In the case of the reduced two-dimensional $\mu_{ij} \times \mu_{i'k}$ spaces, we showed there are only nine independent excluded regions. All other 27 are related to those nine.

The situation would be qualitatively different if the scattered neutrinos from the detection process were also, somehow, measured. This requires experimental capabilities that are way out of current reach. For example, one may consider the dipole-moment mediated process $\nu_\alpha + e^- \to \nu_\beta + e^-$, $\alpha, \beta = e, \mu, \tau$. Assuming a left-handed-helicity ν_α and neutrino energies much larger than the neutrino masses – guaranteed of all available neutrino beams – the outgoing ν_β would have right-handed helicity. If neutrinos are Dirac fermions, the observation of the right-handed-helicity ν_β requires chirality violation and is hence very efficiently suppressed by the neutrino masses squared (in units of the neutrino energy). For all practical purposes, right-handed-helicity ν_β are sterile neutrinos. Instead, if neutrinos are Majorana fermions, the right-handed-helicity ν_β would behave

as what is casually referred to as a $\bar{\nu}_\beta$ and, if measured via charged-current weak interactions, would lead to the production of an ℓ_β^+. In the latter scenario, not only would one be able to measure $\mu_{\alpha\beta}$ (as opposed to $\mu_\alpha^{\rm eff}$), but one would also have discovered that lepton-number-symmetry is violated and that neutrinos are Majorana fermions.

The fact that experimental constraints on the neutrino electromagnetic moments are weaker (and the discovery potential, in some sense, stronger) if neutrinos are Dirac fermions is orthogonal to theoretical expectations that point to a strong correlation between potentially large neutrino electromagnetic moments and Majorana fermions [**88, 89**], highlighted in the Introduction. The discovery of neutrino electromagnetic moments of order $10^{-11}\mu_B$, coupled to knowledge that neutrinos are Dirac fermions, would indicate that the robust assumptions made in [**88, 89**] do not apply and that the physics behind nonzero neutrino masses is more puzzling and subtle than the community currently suspects.

CHAPTER 4

Conclusion

With the observation of neutrino flavor oscillations we have definitive evidence that neutrinos have mass. This deviates from the predictions of the Standard Model, so neutrino masses and flavor oscillations offer a window into Beyond the Standard Model physics and hypotheses. In this thesis, we explored how additional sterile neutrino states affect the NOvA and T2K discrepancy. We also briefly explored the XENON1T anomaly, and studied the parameter space of the fundamental magnetic moments to search for insights and how we could distinguish between Majorana or Dirac neutrinos.

We explored the nature of the NOvA and T2K discrepancy in the presence of a sterile neutrino. We developed simulations that replicate the results of the NOvA and T2K experiments under the three-neutrino picture and allow us to test the four-neutrino hypothesis. The four-neutrino hypothesis yields a better fit ($\Delta\chi^2 \sim 9$) in the Inverted Ordering mass scheme, but the fit suffers from several statistical issues: Firstly, the improvement is still comparable to the number of added degrees of freedom. Secondly, the change in chi-squared $\Delta\chi^2 = \chi^2_{3\nu} - \chi^2_{4\nu}$ should follow a chi-squared distribution. We find that our best-fit values are similar to those when random fluctuations are accounted for. Succinctly, the new oscillation from the four-neutrino model can absorb the statistical fluctuations from individual bins. Nevertheless, if we restrict the new sterile neutrino to have a very small mass-squared splitting Δm^2_{4l}, and therefore avoid the aforementioned statistical pathologies, there still remains a preference of ($\Delta\chi^2 \sim 4$). Although less strong

and smaller than the number of added degrees of freedom, the magnitude of this preference is still comparable to that of other proposed solutions, such as non-standard interactions. Looking forward, NOvA and T2K will continue to collect and analyze data. The continued persistence of this discrepancy or its dissipation will allow us to confirm the existence of a new light fermion state or exclude a wide range of Δm^2_{4l}. In the case that such a light fermion state is detected, the future experiments DUNE and Hyper-Kamiokande will be poised to further study the properties of the new particle.

We briefly explored the XENON1T anomaly and XENONnT measurement to check that the latter has excluded the former. Through this exploration, we saw that an individual solar measurement of a neutrino magnetic moment is not enough to help determine between the Majorana and Dirac hypotheses. Taking a survey of direct neutrino magnetic moment measurements and bounds, we decided that XENONnT and Borexino, LSND, and GEMMA offered the most competitive bounds in the solar, accelerator, and reactor experiments, respectively. Navigating through issues with flat-directions and degeneracies, we show how a future accelerator ν_μ experiment could have nontrivial discovery potential even with sensitivities an order of magnitude behind solar experiments. The measurement of a neutrino magnetic moment by such a future ν_μ experiment would suggest that neutrinos are either Dirac or that additional light fermionic states exist. This is complimentary to the neutrinoless double beta decay search, which aims to show that neutrinos are Majorana particles in the case that a measurment is made. Furthermore, we studied the fundamental magnetic moment observables in the Dirac case in more detail to tease out some degeneracies. We found that, for one-dimensional marginalization, there are only three distinguishable moments μ^{D}_{i1}, μ^{D}_{i2}, and μ^{D}_{i3}. Furtheremore, when showing

constraints for the planes correlating two moments μ^{D}_{ij} and $\mu^{\mathrm{D}}_{i'j}$, we find that instead of the expected 36 planes there are only 9 unique such planes. These patterns hold even if we construct experiments that could measure the outgoing neutrino from the scattering event or if the experiment was sensitive to oscillations.

We have managed to inform the picture of possible new light fermionic states by examining the NOvA and T2K discrepancy and the now superseded XENON1T anomaly. We have also explored the discovery potential for neutrino-electron scattering in future accelerator ν_μ experiments given BSM neutrino dipole moments. Possible topics to revisit in this thesis include: Extending the analysis in Chapter 2 by performing the computationally intensive Feldman-Cousins correction. This would allow us to more robustly rule-out the additional very light sterile neutrino hypothesis. If a future ν_μ experiment were to measure a large BSM neutrino magnetic moment, it would be important to revisit how Majorana neutrinos with additional fermionic states can mimic the number of parameters of the Dirac neutrino dipole matrix as discussed in Chapter 3. Specifically, studying whether matching the number of parameters in the Majorana neutrino dipole matrix by adding sterile states is truly enough to replicate the Dirac results. Furthermore, it would be an opportunity to study what kind of mass and mixing properties these additional fermionic states would have. The massive nature of neutrinos and our rich experimental program give us an unprecedented window into nature and how to improve the SM. The future of the field looks promising when we consider the subtle physics behind massive neutrinos and future experimental pursuits such as DUNE and Hyper-Kamiokande.

References

[1] **NOvA** , M. A. Acero *et al.*, "An Improved Measurement of Neutrino Oscillation Parameters by the NOvA Experiment," arXiv:2108.08219 [hep-ex].

[2] **XENON** , E. Aprile *et al.*, "Excess electronic recoil events in XENON1T," *Phys. Rev. D* **102** (2020) no. 7, 072004, arXiv:2006.09721 [hep-ex].

[3] **T2K** , K. Abe *et al.*, "Improved constraints on neutrino mixing from the T2K experiment with $\mathbf{3.13 \times 10^{21}}$ protons on target," *Phys. Rev. D* **103** (2021) no. 11, 112008, arXiv:2101.03779 [hep-ex].

[4] **MINOS+** , P. Adamson *et al.*, "Search for sterile neutrinos in MINOS and MINOS+ using a two-detector fit," *Phys. Rev. Lett.* **122** (2019) no. 9, 091803, arXiv:1710.06488 [hep-ex].

[5] B. T. Cleveland, T. Daily, R. Davis, Jr., J. R. Distel, K. Lande, C. K. Lee, P. S. Wildenhain, and J. Ullman, "Measurement of the solar electron neutrino flux with the Homestake chlorine detector," *Astrophys. J.* **496** (1998) 505–526.

[6] **SNO** , Q. R. Ahmad *et al.*, "Direct evidence for neutrino flavor transformation from neutral current interactions in the Sudbury Neutrino Observatory," *Phys. Rev. Lett.* **89** (2002) 011301, arXiv:nucl-ex/0204008.

[7] **SAGE** , J. N. Abdurashitov *et al.*, "Solar neutrino flux measurements by the Soviet-American Gallium Experiment (SAGE) for half the 22 year solar cycle," *J. Exp. Theor. Phys.* **95** (2002) 181–193, arXiv:astro-ph/0204245.

[8] **GALLEX** , W. Hampel *et al.*, "GALLEX solar neutrino observations: Results for GALLEX IV," *Phys. Lett. B* **447** (1999) 127–133.

[9] **GNO** , M. Altmann *et al.*, "Complete results for five years of GNO solar neutrino observations," *Phys. Lett. B* **616** (2005) 174–190, arXiv:hep-ex/0504037.

[10] **KamLAND** , K. Eguchi *et al.*, "First results from KamLAND: Evidence for reactor anti-neutrino disappearance," *Phys. Rev. Lett.* **90** (2003) 021802, arXiv:hep-ex/0212021.

[11] **Super-Kamiokande** , S. Fukuda *et al.*, "Determination of solar neutrino oscillation parameters using 1496 days of Super-Kamiokande I data," *Phys. Lett. B* **539** (2002) 179–187, arXiv:hep-ex/0205075.

[12] **Super-Kamiokande** , Y. Fukuda *et al.*, "Evidence for oscillation of atmospheric neutrinos," *Phys. Rev. Lett.* **81** (1998) 1562–1567, arXiv:hep-ex/9807003.

[13] **Borexino** , C. Arpesella *et al.*, "Direct Measurement of the Be-7 Solar Neutrino Flux with 192 Days of Borexino Data," *Phys. Rev. Lett.* **101** (2008) 091302, arXiv:0805.3843 [astro-ph].

[14] **Daya Bay** , F. P. An *et al.*, "Observation of electron-antineutrino disappearance at Daya Bay," *Phys. Rev. Lett.* **108** (2012) 171803, arXiv:1203.1669 [hep-ex].

[15] **RENO** , J. K. Ahn *et al.*, "Observation of Reactor Electron Antineutrino Disappearance in the RENO Experiment," *Phys. Rev. Lett.* **108** (2012) 191802, arXiv:1204.0626 [hep-ex].

[16] **Double Chooz** , Y. Abe *et al.*, "Indication of Reactor $\bar{\nu}_e$ Disappearance in the Double Chooz Experiment," *Phys. Rev. Lett.* **108** (2012) 131801, arXiv:1112.6353 [hep-ex].

[17] **T2K** , K. Abe *et al.*, "Indication of Electron Neutrino Appearance from an Accelerator-produced Off-axis Muon Neutrino Beam," *Phys. Rev. Lett.* **107** (2011) 041801, arXiv:1106.2822 [hep-ex].

[18] **NOvA** , P. Adamson *et al.*, "First measurement of electron neutrino appearance in NOvA," *Phys. Rev. Lett.* **116** (2016) no. 15, 151806, arXiv:1601.05022 [hep-ex].

[19] **DUNE** , B. Abi *et al.*, "Deep Underground Neutrino Experiment (DUNE), Far Detector Technical Design Report, Volume II: DUNE Physics," arXiv:2002.03005 [hep-ex].

[20] **Hyper-Kamiokande** , K. Abe *et al.*, "Hyper-Kamiokande Design Report," arXiv:1805.04163 [physics.ins-det].

[21] **JUNO** , A. Abusleme *et al.*, "JUNO physics and detector," *Prog. Part. Nucl. Phys.* **123** (2022) 103927, arXiv:2104.02565 [hep-ex].

[22] C. Giunti and A. Studenikin, "Neutrino electromagnetic interactions: a window to new physics," *Rev. Mod. Phys.* **87** (2015) 531, arXiv:1403.6344 [hep-ph].

[23] **LSND** , A. Aguilar *et al.*, "Evidence for neutrino oscillations from the observation of $\bar{\nu}_e$ appearance in a $\bar{\nu}_\mu$ beam," *Phys. Rev. D* **64** (2001) 112007, arXiv:hep-ex/0104049.

[24] **MiniBooNE** , A. A. Aguilar-Arevalo *et al.*, "Significant Excess of ElectronLike Events in the MiniBooNE Short-Baseline Neutrino Experiment," *Phys. Rev. Lett.* **121** (2018) no. 22, 221801, arXiv:1805.12028 [hep-ex].

[25] V. V. Barinov *et al.*, "Results from the Baksan Experiment on Sterile Transitions (BEST)," *Phys. Rev. Lett.* **128** (2022) no. 23, 232501, arXiv:2109.11482 [nucl-ex].

[26] G. Mention, M. Fechner, T. Lasserre, T. A. Mueller, D. Lhuillier, M. Cribier, and A. Letourneau, "The Reactor Antineutrino Anomaly," *Phys. Rev. D* **83** (2011) 073006, arXiv:1101.2755 [hep-ex].

[27] J. M. Berryman and P. Huber, "Reevaluating Reactor Antineutrino Anomalies with Updated Flux Predictions," *Phys. Rev. D* **101** (2020) no. 1, 015008, arXiv:1909.09267 [hep-ph].

[28] I. Esteban, M. C. Gonzalez-Garcia, M. Maltoni, T. Schwetz, and A. Zhou, "The fate of hints: updated global analysis of three-flavor neutrino oscillations," *JHEP* **09** (2020) 178, arXiv:2007.14792 [hep-ph].

[29] **XENON** , E. Aprile *et al.*, "Search for New Physics in Electronic Recoil Data from XENONnT," arXiv:2207.11330 [hep-ex].

[30] P. Dunne, "Latest Neutrino Oscillation Results from T2K, doi:10.5281/zenodo.3959558," July, 2020. https://doi.org/10.5281/zenodo.3959558.

[31] A. Himmel, "New Oscillation Results from the NOvA Experiment, doi:10.5281/zenodo.3959581," July, 2020. https://doi.org/10.5281/zenodo.3959581.

[32] K. J. Kelly, P. A. N. Machado, S. J. Parke, Y. F. Perez-Gonzalez, and R. Z. Funchal, "Neutrino mass ordering in light of recent data," *Phys. Rev. D* **103** (2021) no. 1, 013004, arXiv:2007.08526 [hep-ph].

[33] P. F. de Salas, D. V. Forero, S. Gariazzo, P. Martínez-Miravé, O. Mena, C. A. Ternes, M. Tórtola, and J. W. F. Valle, "2020 global reassessment of the neutrino oscillation picture," *JHEP* **02** (2021) 071, arXiv:2006.11237 [hep-ph].

[34] F. Capozzi, E. Di Valentino, E. Lisi, A. Marrone, A. Melchiorri, and A. Palazzo, "Unfinished fabric of the three neutrino paradigm," *Phys. Rev. D* **104** (2021) no. 8, 083031, arXiv:2107.00532 [hep-ph].

[35] **Daya Bay** , D. Adey *et al.*, "Measurement of the Electron Antineutrino Oscillation with 1958 Days of Operation at Daya Bay," *Phys. Rev. Lett.* **121** (2018) no. 24, 241805, arXiv:1809.02261 [hep-ex].

[36] **RENO** , G. Bak *et al.*, "Measurement of Reactor Antineutrino Oscillation Amplitude and Frequency at RENO," *Phys. Rev. Lett.* **121** (2018) no. 20, 201801, arXiv:1806.00248 [hep-ex].

[37] **Double Chooz** , H. de Kerret *et al.*, "Double Chooz θ_{13} measurement via total neutron capture detection," *Nature Phys.* **16** (2020) no. 5, 558–564, arXiv:1901.09445 [hep-ex].

[38] R. Jimenez, C. Pena-Garay, K. Short, F. Simpson, and L. Verde, "Neutrino Masses and Mass Hierarchy: Evidence for the Normal Hierarchy," arXiv:2203.14247 [hep-ph].

[39] S. Gariazzo *et al.*, "Neutrino mass and mass ordering: No conclusive evidence for normal ordering," arXiv:2205.02195 [hep-ph].

[40] P. B. Denton, J. Gehrlein, and R. Pestes, "CP -Violating Neutrino Nonstandard Interactions in Long-Baseline-Accelerator Data," *Phys. Rev. Lett.* **126** (2021) no. 5, 051801, arXiv:2008.01110 [hep-ph].

[41] L. S. Miranda, P. Pasquini, U. Rahaman, and S. Razzaque, "Searching for non-unitary neutrino oscillations in the present T2K and NOνA data," *Eur. Phys. J. C* **81** (2021) no. 5, 444, arXiv:1911.09398 [hep-ph].

[42] S. S. Chatterjee and A. Palazzo, "Interpretation of NOνA and T2K data in the presence of a light sterile neutrino," arXiv:2005.10338 [hep-ph].

[43] S. S. Chatterjee and A. Palazzo, "Nonstandard Neutrino Interactions as a Solution to the $NO\nu A$ and T2K Discrepancy," *Phys. Rev. Lett.* **126** (2021) no. 5, 051802, arXiv:2008.04161 [hep-ph].

[44] D. V. Forero, C. Giunti, C. A. Ternes, and M. Tortola, "Nonunitary neutrino mixing in short and long-baseline experiments," *Phys. Rev. D* **104** (2021) no. 7, 075030, arXiv:2103.01998 [hep-ph].

[45] U. Rahaman, "Looking for Lorentz invariance violation (LIV) in the latest long baseline accelerator neutrino oscillation data," *Eur. Phys. J. C* **81** (2021) no. 9, 792, arXiv:2103.04576 [hep-ph].

[46] U. Rahaman, S. Razzaque, and S. U. Sankar, "A review of the tension between the T2K and NOνA appearance data and hints to new physics," arXiv:2201.03250 [hep-ph].

[47] S. A. R. Ellis, K. J. Kelly, and S. W. Li, "Leptonic Unitarity Triangles," *Phys. Rev. D* **102** (2020) no. 11, 115027, arXiv:2004.13719 [hep-ph].

[48] S. A. R. Ellis, K. J. Kelly, and S. W. Li, "Current and Future Neutrino Oscillation Constraints on Leptonic Unitarity," *JHEP* **12** (2020) 068, arXiv:2008.01088 [hep-ph].

[49] **Super-Kamiokande** , K. Abe *et al.*, "Solar Neutrino Measurements in Super-Kamiokande-IV," *Phys. Rev. D* **94** (2016) no. 5, 052010, arXiv:1606.07538 [hep-ex].

[50] Y. Nakajima, "Recent results and future prospects from Super-Kamiokande," June, 2020. https://doi.org/10.5281/zenodo.3959640.

[51] **KamLAND** , A. Gando *et al.*, "Reactor On-Off Antineutrino Measurement with KamLAND," *Phys. Rev. D* **88** (2013) no. 3, 033001, arXiv:1303.4667 [hep-ex].

[52] **T2K** , K. Abe *et al.*, "Search for light sterile neutrinos with the T2K far detector Super-Kamiokande at a baseline of 295 km," *Phys. Rev. D* **99** (2019) no. 7, 071103, arXiv:1902.06529 [hep-ex].

[53] S. S. Wilks, "The Large-Sample Distribution of the Likelihood Ratio for Testing Composite Hypotheses," *Annals Math. Statist.* **9** (1938) no. 1, 60–62.

[54] **Daya Bay** , F. P. An *et al.*, "Improved Search for a Light Sterile Neutrino with the Full Configuration of the Daya Bay Experiment," *Phys. Rev. Lett.* **117** (2016) no. 15, 151802, arXiv:1607.01174 [hep-ex].

[55] Y. Declais *et al.*, "Search for neutrino oscillations at 15-meters, 40-meters, and 95-meters from a nuclear power reactor at Bugey," *Nucl. Phys. B* **434** (1995) 503–534.

[56] **MINOS+, Daya Bay** , P. Adamson *et al.*, "Improved Constraints on Sterile Neutrino Mixing from Disappearance Searches in the MINOS, MINOS+, Daya Bay, and Bugey-3 Experiments," *Phys. Rev. Lett.* **125** (2020) no. 7, 071801, arXiv:2002.00301 [hep-ex].

[57] M. Dentler, A. Hernández-Cabezudo, J. Kopp, P. A. N. Machado, M. Maltoni, I. Martinez-Soler, and T. Schwetz, "Updated Global Analysis of Neutrino Oscillations in the Presence of eV-Scale Sterile Neutrinos," *JHEP* **08** (2018) 010, arXiv:1803.10661 [hep-ph].

[58] **Super-Kamiokande** , K. Abe *et al.*, "Limits on sterile neutrino mixing using atmospheric neutrinos in Super-Kamiokande," *Phys. Rev. D* **91** (2015) 052019, arXiv:1410.2008 [hep-ex].

[59] **IceCube** , M. G. Aartsen *et al.*, "Search for sterile neutrino mixing using three years of IceCube DeepCore data," *Phys. Rev. D* **95** (2017) no. 11, 112002, arXiv:1702.05160 [hep-ex].

[60] S. Gariazzo, P. F. de Salas, and S. Pastor, "Thermalisation of sterile neutrinos in the early Universe in the 3+1 scheme with full mixing matrix," *JCAP* **07** (2019) 014, arXiv:1905.11290 [astro-ph.CO].

[61] J. M. Berryman, A. de Gouvêa, K. J. Kelly, and A. Kobach, "Sterile neutrino at the Deep Underground Neutrino Experiment," *Phys. Rev. D* **92** (2015) no. 7, 073012, arXiv:1507.03986 [hep-ph].

[62] K. J. Kelly, "Searches for new physics at the Hyper-Kamiokande experiment," *Phys. Rev. D* **95** (2017) no. 11, 115009, arXiv:1703.00448 [hep-ph].

[63] W. J. Marciano and A. I. Sanda, "Exotic Decays of the Muon and Heavy Leptons in Gauge Theories," *Phys. Lett. B* **67** (1977) 303–305.

[64] B. W. Lee and R. E. Shrock, "Natural Suppression of Symmetry Violation in Gauge Theories: Muon - Lepton and Electron Lepton Number Nonconservation," *Phys. Rev. D* **16** (1977) 1444.

[65] K. Fujikawa and R. Shrock, "The Magnetic Moment of a Massive Neutrino and Neutrino Spin Rotation," *Phys. Rev. Lett.* **45** (1980) 963.

[66] A. G. Beda, V. B. Brudanin, V. G. Egorov, D. V. Medvedev, V. S. Pogosov, M. V. Shirchenko, and A. S. Starostin, "The results of search for the neutrino magnetic moment in GEMMA experiment," *Adv. High Energy Phys.* **2012** (2012) 350150.

[67] **Borexino** , M. Agostini *et al.*, "Limiting neutrino magnetic moments with Borexino Phase-II solar neutrino data," *Phys. Rev. D* **96** (2017) no. 9, 091103, arXiv:1707.09355 [hep-ex].

[68] J. Billard, J. Johnston, and B. J. Kavanagh, "Prospects for exploring New Physics in Coherent Elastic Neutrino-Nucleus Scattering," *JCAP* **11** (2018) 016, arXiv:1805.01798 [hep-ph].

[69] O. G. Miranda, D. K. Papoulias, M. Tórtola, and J. W. F. Valle, "Probing neutrino transition magnetic moments with coherent elastic neutrino-nucleus scattering," *JHEP* **07** (2019) 103, arXiv:1905.03750 [hep-ph].

[70] D. Baxter *et al.*, "Coherent Elastic Neutrino-Nucleus Scattering at the European Spallation Source," *JHEP* **02** (2020) 123, arXiv:1911.00762 [physics.ins-det].

[71] V. Mathur, I. M. Shoemaker, and Z. Tabrizi, "Using DUNE to Shed Light on the Electromagnetic Properties of Neutrinos," arXiv:2111.14884 [hep-ph].

[72] J. Aalbers *et al.*, "A Next-Generation Liquid Xenon Observatory for Dark Matter and Neutrino Physics," arXiv:2203.02309 [physics.ins-det].

[73] A. Heger, A. Friedland, M. Giannotti, and V. Cirigliano, "The Impact of Neutrino Magnetic Moments on the Evolution of Massive Stars," *Astrophys. J.* **696** (2009) 608–619, arXiv:0809.4703 [astro-ph].

[74] S. A. Díaz, K.-P. Schröder, K. Zuber, D. Jack, and E. E. B. Barrios, "Constraint on the axion-electron coupling constant and the neutrino magnetic dipole moment by using the tip-RGB luminosity of fifty globular clusters," arXiv:1910.10568 [astro-ph.SR].

[75] J. M. Lattimer and J. Cooperstein, "Limits on the Neutrino Magnetic Moment from SN 1987a," *Phys. Rev. Lett.* **61** (1988) 23–26. [Erratum: Phys.Rev.Lett. 61, 2633 (1988)].

[76] G. G. Raffelt, "Limits on neutrino electromagnetic properties: An update," *Phys. Rept.* **320** (1999) 319–327.

[77] J. F. Beacom and P. Vogel, "Neutrino magnetic moments, flavor mixing, and the Super-Kamiokande solar data," *Phys. Rev. Lett.* **83** (1999) 5222–5225, arXiv:hep-ph/9907383.

[78] W. Grimus and T. Schwetz, "Elastic neutrino electron scattering of solar neutrinos and potential effects of magnetic and electric dipole moments," *Nucl. Phys. B* **587** (2000) 45–66, arXiv:hep-ph/0006028.

[79] A. S. Joshipura and S. Mohanty, "Bounds on neutrino magnetic moment tensor from solar neutrinos," *Phys. Rev. D* **66** (2002) 012003, arXiv:hep-ph/0204305.

[80] W. Grimus, M. Maltoni, T. Schwetz, M. A. Tortola, and J. W. F. Valle, "Constraining Majorana neutrino electromagnetic properties from the LMA-MSW solution of the solar neutrino problem," *Nucl. Phys. B* **648** (2003) 376–396, arXiv:hep-ph/0208132.

[81] B. C. Canas, O. G. Miranda, A. Parada, M. Tortola, and J. W. F. Valle, "Updating neutrino magnetic moment constraints," *Phys. Lett. B* **753** (2016) 191–198, arXiv:1510.01684 [hep-ph]. [Addendum: Phys.Lett.B 757, 568–568 (2016)].

[82] O. G. Miranda, D. K. Papoulias, O. Sanders, M. Tórtola, and J. W. F. Valle, "Low-energy probes of sterile neutrino transition magnetic moments," *JHEP* **12** (2021) 191, arXiv:2109.09545 [hep-ph].

[83] D. Aristizabal Sierra, O. G. Miranda, D. K. Papoulias, and G. S. Garcia, "Neutrino magnetic and electric dipole moments: From measurements to parameter space," *Phys. Rev. D* **105** (2022) no. 3, 035027, arXiv:2112.12817 [hep-ph].

[84] M. Cadeddu, F. Dordei, C. Giunti, Y. F. Li, E. Picciau, and Y. Y. Zhang, "Physics results from the first COHERENT observation of coherent elastic neutrino-nucleus scattering in argon and their combination with cesium-iodide data," *Phys. Rev. D* **102** (2020) no. 1, 015030, arXiv:2005.01645 [hep-ph].

[85] M. Atzori Corona, M. Cadeddu, N. Cargioli, F. Dordei, C. Giunti, Y. F. Li, C. A. Ternes, and Y. Y. Zhang, "Impact of the Dresden-II and COHERENT neutrino scattering data on neutrino electromagnetic properties and electroweak physics," arXiv:2205.09484 [hep-ph].

[86] A. N. Khan, "New limits on neutrino electromagnetic interactions and light new physics with XENONnT," arXiv:2208.02144 [hep-ph].

[87] S. K. A., A. Majumdar, D. K. Papoulias, H. Prajapati, and R. Srivastava, "First results of LZ and XENONnT: A comparative study of neutrino properties and light mediators," arXiv:2208.06415 [hep-ph].

[88] N. F. Bell, V. Cirigliano, M. J. Ramsey-Musolf, P. Vogel, and M. B. Wise, "How magnetic is the Dirac neutrino?," *Phys. Rev. Lett.* **95** (2005) 151802, arXiv:hep-ph/0504134.

[89] N. F. Bell, M. Gorchtein, M. J. Ramsey-Musolf, P. Vogel, and P. Wang, "Model independent bounds on magnetic moments of Majorana neutrinos," *Phys. Lett. B* **642** (2006) 377–383, arXiv:hep-ph/0606248.

[90] M. Lindner, B. Radovčić, and J. Welter, "Revisiting Large Neutrino Magnetic Moments," *JHEP* **07** (2017) 139, arXiv:1706.02555 [hep-ph].

[91] P. Vogel and J. Engel, "Neutrino Electromagnetic Form-Factors," *Phys. Rev. D* **39** (1989) 3378.

[92] **COHERENT** , D. Akimov *et al.*, "COHERENT Collaboration data release from the first observation of coherent elastic neutrino-nucleus scattering," arXiv:1804.09459 [nucl-ex].

[93] **DONUT** , R. Schwienhorst *et al.*, "A New upper limit for the tau - neutrino magnetic moment," *Phys. Lett. B* **513** (2001) 23–29, arXiv:hep-ex/0102026.

[94] J. Khoury and A. Weltman, "Chameleon cosmology," *Phys. Rev. D* **69** (2004) 044026, arXiv:astro-ph/0309411.

[95] N. Bar, K. Blum, and G. D'Amico, "Is there a supernova bound on axions?," *Phys. Rev. D* **101** (2020) no. 12, 123025, arXiv:1907.05020 [hep-ph].

[96] M. Maltoni and A. Y. Smirnov, "Solar neutrinos and neutrino physics," *Eur. Phys. J. A* **52** (2016) no. 4, 87, arXiv:1507.05287 [hep-ph].

[97] V. Brdar, A. Greljo, J. Kopp, and T. Opferkuch, "The Neutrino Magnetic Moment Portal: Cosmology, Astrophysics, and Direct Detection," *JCAP* **01** (2021) 039, arXiv:2007.15563 [hep-ph].

[98] J. A. Grifols, E. Masso, and S. Mohanty, "Neutrino magnetic moments and photodisintegration of deuterium," *Phys. Lett. B* **587** (2004) 184–188, arXiv:hep-ph/0401144.

[99] **TEXONO** , M. Deniz *et al.*, "Measurement of Nu(e)-bar -Electron Scattering Cross-Section with a CsI(Tl) Scintillating Crystal Array at the Kuo-Sheng Nuclear Power Reactor," *Phys. Rev. D* **81** (2010) 072001, arXiv:0911.1597 [hep-ex].

[100] **CONUS** , H. Bonet *et al.*, "First limits on neutrino electromagnetic properties from the CONUS experiment," arXiv:2201.12257 [hep-ex].

[101] **LSND** , L. B. Auerbach *et al.*, "Measurement of electron - neutrino - electron elastic scattering," *Phys. Rev. D* **63** (2001) 112001, arXiv:hep-ex/0101039.

[102] S. Ajimura *et al.*, "Technical Design Report (TDR): Searching for a Sterile Neutrino at J-PARC MLF (E56, JSNS2)," arXiv:1705.08629 [physics.ins-det].

[103] S. Ajimura *et al.*, "Proposal: JSNS^2-II," arXiv:2012.10807 [hep-ex].

[104] B. C. Canas, O. G. Miranda, A. Parada, M. Tortola, and J. W. F. Valle, "New limits on neutrino magnetic moments from low energy neutrino data," *J. Phys. Conf. Ser.* **761** (2016) no. 1, 012043, arXiv:1609.08563 [hep-ph].

APPENDIX A

Appendix to chapter 2

A.1. Detailed Fit Results

In Section 2.4, we provided best-fit points of our analyses of T2K, NOvA, and their combination under the three- and four-neutrino hypotheses. When discussing the best-fit points under the four-neutrino hypothesis (Table 2.3), we showed the results of the analysis (i.e. which signs of Δm^2_{31} and Δm^2_{4l}) that provided the best overall fit to each experimental data set. In this appendix, we provide the results to all four fits for each experiment/combination. Table A.1 does so for our analyses of T2K and NOvA data separately, and Table A.2 does so for their combination.

Table A.1. Best-fit 4ν parameters of our four T2K (top) and NOvA (bottom) analyses. See Section 2.4.2 for more detail.

4ν	T2K			
	NO		IO	
	$\Delta m^2_{4l} > 0$	< 0	> 0	< 0
$\sin^2\theta_{13}$	0.024	0.024	0.024	0.024
$\sin^2\theta_{23}$	0.44	0.44	0.44	0.43
$\Delta m^2_{31}/10^{-3}$ eV^2	2.49	2.48	-2.38	-2.39
$\delta_{\rm CP}$	4.94	4.89	4.45	4.42
$\sin^2\theta_{14}$	7.1×10^{-2}	7.8×10^{-2}	8.0×10^{-2}	7.8×10^{-2}
$\sin^2\theta_{24}$	4.2×10^{-2}	4.0×10^{-2}	4.1×10^{-2}	4.1×10^{-2}
$\sin^2\theta_{34}$	5.2×10^{-2}	5.2×10^{-2}	5.6×10^{-1}	7.8×10^{-1}
$\Delta m^2_{4l}/$eV^2	1.1×10^{-2}	-9.0×10^{-3}	1.1×10^{-2}	-8.5×10^{-3}
δ_{14}	3.51	3.14	2.08	1.83
δ_{24}	6.10	5.89	2.72	2.64
$\chi^2_{4\nu}$	62.07	62.63	62.80	61.95
Best-fit	$m_4 < m_3 < m_1 < m_2$			
$\chi^2_{3\nu} - \chi^2_{4\nu}$	4.87			

	NOvA			
	NO		IO	
	$\Delta m^2_{4l} > 0$	< 0	> 0	< 0
$\sin^2\theta_{13}$	0.022	0.022	0.022	0.022
$\sin^2\theta_{23}$	0.44	0.62	0.59	0.41
$\Delta m^2_{31}/10^{-3}$ eV^2	2.43	2.44	-2.32	-2.35
$\delta_{\rm CP}$	0.00	5.22	3.19	4.58
$\sin^2\theta_{14}$	6.9×10^{-3}	1.6×10^{-2}	8.9×10^{-3}	1.4×10^{-2}
$\sin^2\theta_{24}$	1.2×10^{-1}	1.2×10^{-1}	1.3×10^{-1}	1.1×10^{-1}
$\sin^2\theta_{34}$	0.29	0.79	0.34	0.69
$\sin^2\theta_{34}$	1.0×10^{-2}	-8.0×10^{-3}	1.0×10^{-2}	-8.1×10^{-3}
$\Delta m^2_{4l}/$eV^2	3.51	4.07	4.81	4.69
δ_{14}	3.15	3.21	0.12	0.15
δ_{24}	38.10	38.14	38.13	38.16
Best-fit	$m_1 < m_2 < m_3 < m_4$			
$\chi^2_{3\nu} - \chi^2_{4\nu}$	5.30			

Table A.2. Best-fit 4ν parameters of our four combined T2K+NOvA analyses. See Section 2.4.2 for more detail.

4ν	Combined T2K and NOvA			
	NO		IO	
	$\Delta m^2_{4l} > 0$	< 0	> 0	< 0
$\sin^2\theta_{13}$	0.023	0.025	0.023	0.023
$\sin^2\theta_{23}$	0.45	0.45	0.44	0.43
$\Delta m^2_{31}/10^{-3}$ eV^2	2.49	2.51	-2.36	-2.39
δ_{CP}	4.09	3.88	1.72	4.47
$\sin^2\theta_{14}$	2.1×10^{-2}	1.1×10^{-1}	3.4×10^{-2}	4.3×10^{-2}
$\sin^2\theta_{24}$	5.3×10^{-2}	3.3×10^{-2}	5.3×10^{-2}	6.0×10^{-2}
$\sin^2\theta_{34}$	0.56	0.21	1.1×10^{-2}	0.37
$\Delta m^2_{4l}/\mathrm{eV}^2$	1.1×10^{-2}	-1.1×10^{-2}	1.2×10^{-2}	-8.5×10^{-3}
δ_{14}	0.01	0.03	6.09	4.88
δ_{24}	1.82	1.18	0.53	5.89
$\chi^2_{4\nu}$	107.41	107.62	104.27	102.83
Best-fit	$m_4 < m_3 < m_1 < m_2$			
$\chi^2_{3\nu} - \chi^2_{4\nu}$	8.99			